Synthesis and Analysis of Palladium Modified Bi_2WO_6/BiOCl Composites for Enhanced Water Decontamination

Shivam Parekh

A thesis submitted to the Faculty of Engineering in partial fulfillment of the requirements for the Master of Applied Science degree in Chemical Engineering

uOttawa

Department of Chemical and Biological Engineering
Faculty of Engineering
University of Ottawa

Abstract

Over the past several decades, rapid industrial and population growth has put a strain on the environment and clean water supplies by exposing them to harmful toxins such as heavy metals and organic and inorganic pollutants. As such, water decontamination remains a vital issue that needs to be addressed in the 21st century. Over the years, various water treatment strategies have been deployed, including ion exchange, membrane filtration, adsorption, and precipitation. However, many of these techniques are hindered by incomplete treatment and high operation and energy costs. In more recent times, advanced oxidation processes (AOPs), including UV disinfection, ozone disinfection, and heterogeneous photocatalysis, have sought to provide effective and environmentally friendly solutions to water treatment. Among these, semiconductor photocatalysis has attracted growing interest due to its ability to degrade a plethora of organic and inorganic pollutants into innocuous compounds such as H_2O and CO_2.

Photocatalysis uses light energy to activate a photoactive material, usually in the form of a semiconductor, to allow for the degradation of harmful pollutants in water. When photocatalysts are exposed to light with energy equal to or greater than their band gap, their electrons (e^-) are excited from the valence band (VB) to the conduction band (CB), leaving positively charged holes (h^+) in their place. These charge carriers can subsequently participate in reduction and oxidation reactions to break down undesirable pollutants. Historically, TiO_2 has been regarded as an ideal photocatalyst for its high stability, commercial availability, non-toxicity, and low cost. However, due to its wide band gap (>3.2 eV), it is only active under UV light. This hinders the application of TiO_2 in water decontamination processes that rely on visible-light-driven photocatalysis. Hence, modern work in this field focuses on the development of photocatalysts that access a larger portion of the solar spectrum.

This work concerns the synthesis and analysis of a novel Pd-Bi_2WO_6/BiOCl heterojunction photocatalyst. Bi_2WO_6/BiOCl was prepared using a hydrothermal technique, whose conditions, including composite ratio, calcination temperature, and calcination time, were optimized based on their performance in the degradation of Rhodamine B (RhB) under visible light. Pd-Bi_2WO_6/BiOCl samples with varying amounts of palladium were fabricated by the photoreduction method. The novel catalyst was analyzed with x-ray diffraction (XRD), x-ray photoelectron spectroscopy (XPS), scanning electron microscopy (SEM), ultraviolet-visible diffuse reflectance spectroscopy (UV-vis DRS), and N_2-sorption testing. It was demonstrated that the palladium-modified composites exhibited improved RhB photodegradation, with 0.5 wt% Pd-Bi_2WO_6/BiOCl showing maximal photoactivity, representing approximately 25% improvement over Bi_2WO_6/BiOCl. The improved results were attributed to the formation of a Schottky junction and the surface plasmon resonance (SPR) effect, which suppressed the recombination of e^- and h^+ and boosted the visible light responsiveness.

Quenching experiments revealed that holes and hydroxyl radicals were the main oxidizing species responsible for the breakdown of RhB molecules. The stability and reusability of the catalyst were demonstrated with a four stage recycle test. Experiments were also done to study the effects of key operational parameters, including the initial RhB concentration, catalyst dosage, reaction temperature, and water pH. From the experimental findings and characterization analyses, it was proposed that Pd-Bi_2WO_6/BiOCl forms a type I heterojunction that uses h^+ and $\bullet OH$ to degrade RhB via the N-de-eethylation process. Overall, this study endorsed the use of plasmonic heterojunction photocatalysts for the effective treatment of organic pollutants in water.

Résumé

Au cours des dernières décennies, la croissance rapide de l'industrie et de la population a mis à rude épreuve l'environnement et les réserves d'eau propre en les exposant à des toxines nocives telles que les métaux lourds et les polluants organiques et inorganiques. La décontamination de l'eau reste donc une question vitale qu'il convient d'aborder au XXIe siècle. Au fil des ans, diverses stratégies de traitement de l'eau ont été déployées, notamment l'échange d'ions, la filtration sur membrane, l'adsorption et la précipitation. Toutefois, bon nombre de ces techniques sont entravées par un traitement incomplet et des coûts d'exploitation et d'énergie élevés. Plus récemment, les procédés d'oxydation avancés (POA), notamment la désinfection par UV, la désinfection à l'ozone et la photocatalyse hétérogène, ont cherché à fournir des solutions efficaces et respectueuses de l'environnement pour le traitement de l'eau. Parmi ces procédés, la photocatalyse à semi-conducteurs a suscité un intérêt croissant en raison de sa capacité à dégrader une pléthore de polluants organiques et inorganiques en composés inoffensifs tels que l'H_2O et le CO_2.

La photocatalyse utilise l'énergie lumineuse pour activer un matériau photoactif, généralement sous la forme d'un semi-conducteur, afin de permettre la dégradation des polluants nocifs présents dans l'eau. Lorsque les photocatalyseurs sont exposés à la lumière avec une énergie égale ou supérieure à leur bande interdite, leurs électrons (e^-) sont excités de la bande de valence (VB) à la bande de conduction (CB), laissant à leur place des trous chargés positivement (h^+). Ces porteurs de charge peuvent ensuite participer à des réactions de réduction et d'oxydation pour décomposer les polluants indésirables. Historiquement, le TiO_2 a été considéré comme un photocatalyseur idéal en raison de sa grande stabilité, de sa disponibilité commerciale, de sa non-toxicité et de son faible coût. Cependant, en raison de sa large bande interdite (>3,2 eV), il n'est actif que sous la lumière UV. Cela entrave l'application du TiO_2 dans les processus de décontamination de l'eau qui reposent sur la photocatalyse à la lumière visible. C'est pourquoi les travaux actuels dans ce domaine se concentrent sur le développement de photocatalyseurs qui accèdent à une plus grande partie du spectre solaire.

Ce travail concerne la synthèse et l'analyse d'un nouveau photocatalyseur à hétérojonction Pd-Bi_2WO_6/BiOCl. Bi_2WO_6/BiOCl a été préparé à l'aide d'une technique hydrothermale, dont les conditions, y compris le rapport composite, la température de calcination et le temps de calcination, ont été optimisées sur la base de leur performance dans la dégradation de la Rhodamine B (RhB) sous la lumière visible. Des échantillons de Pd-Bi_2WO_6/BiOCl avec des quantités variables de palladium ont été fabriqués par la méthode de photoréduction. Le nouveau catalyseur a été analysé par diffraction des rayons X (XRD), spectroscopie photoélectronique à rayons X (XPS), microscopie électronique à balayage (SEM), spectroscopie de réflectance diffuse ultraviolette-visible (UV-vis DRS) et test d'absorption de N2. Il a été démontré que les composites modifiés au palladium présentaient une meilleure photodégradation du RhB, avec 0,5 % en poids de Pd-Bi_2WO_6/BiOCl montrant une photoactivité maximale, ce qui représente une amélioration d'environ 25 % par rapport à Bi_2WO_6/BiOCl. Les résultats améliorés ont été attribués à la formation d'une jonction Schottky et à l'effet de résonance plasmonique de surface (SPR), qui a supprimé la recombinaison des e^- et h^+ et a stimulé la réactivité à la lumière visible.

Les expériences de trempe ont révélé que les trous et les radicaux hydroxyles étaient les principales espèces oxydantes responsables de la décomposition des molécules de RhB. La stabilité et la réutilisation du catalyseur ont été démontrées par un test de recyclage en quatre étapes. Des expériences ont également été réalisées pour étudier les effets des principaux paramètres opérationnels, notamment la concentration initiale de RhB, le dosage du catalyseur, la température de réaction et le pH de l'eau. Sur la base des résultats expérimentaux et des analyses de

caractérisation, il a été proposé que Pd-Bi_2WO_6/BiOCl forme une hétérojonction de type I qui utilise h^+ et •OH pour dégrader le RhB via le processus de N-déethylation. Dans l'ensemble, cette étude a approuvé l'utilisation de photocatalyseurs à hétérojonction plasmonique pour le traitement efficace des polluants organiques dans l'eau.

Acknowledgments

I would like to start by expressing my heartfelt gratitude to Dr. Jason Zhang for all of his support and encouragement over the course of this project. None of this work would have been possible without his guidance. I truly appreciate the time and care he has dedicated to supervising my work.

I would like to acknowledge the support of the Natural Sciences and Engineering Research Council of Canada (NSERC), whose discovery grant helped support this project and our lab.

I would like to express my gratitude to Dr. Yun Liu at the University of Ottawa's Centre for Catalysis and Innovation (CCRI) for her help with SEM imaging; Dr. Jeffey Owens and Sarah Osterholm at the X-ray core facility for their help with XRD analysis; Dr. Gabriele Schatte at Queen's University for her help attaining XPS data; and Dr. Ashlee Howarth at Concordia University for her help with N_2 sorption testing and BET surface analysis.

I would also like to recognize the support and friendship of my labmates, Yuanchen Zhu and Shiqian Li. I will always cherish our time together in the lab and greatly appreciate our friendship.

I would like to thank my friends and family, who are always there for me. I would not have been able to complete this work without their support.

I would like to take a moment to express my gratitude to my parents. They have always allowed me to follow my dreams, and their unconditional love and support have inspired me to be a better student and person. I will forever be grateful for everything they have done for me.

Finally, I would like to thank my amazing catalysts, who never cease to surprise me… our time together was quite illuminating (under visible light, of course).

Table of Contents

List of Figures

List of Tables

Chapter 1: Introduction

1.1 Background

As the global population continues to rise and spur rapid industrial growth, there has been a growing concern over the increasing lack of access to essential resources and environmental degradation. Over the past several decades, industrialization has posed a risk to the environment by exposing it to harmful materials such as heavy metals and organic and inorganic pollutants that have seen greater detection levels in clean water sources [1]. This has resulted in an increased risk to safe access to clean drinking water. According to the United Nations, over two billion people worldwide are unable to access clean drinking water [2]. As such, water decontamination has become a vital issue that needs to be addressed in the 21st century.

Traditionally, various water treatment strategies have been used to address water contamination. These include ion exchange, membrane filtration, adsorption, and precipitation [3]. These processes have been limited by incomplete treatment of organic pollutants and high energy and financial cost of operation [4]. Additionally, many of these processes produce harmful secondary by-products which can be carcinogenic [5]. In more recent times, advanced oxidation processes (AOPs) including UV and ozone disinfection have sought to provide more comprehensive and environmentally friendly approaches to water treatment [1], [6]. However, these methods are often hindered by high energy and operational costs [7]. Recently, heterogeneous photocatalysis has emerged as a viable candidate for water treatment applications. This is because photocatalysis can achieve complete water treatment while operating at ambient conditions without producing harmful side products [1], [6]. Thus, providing an environmentally and cost-friendly approach to water decontamination.

Photocatalysis, an advanced oxidation process, uses light energy to activate a photoactive material, usually a semiconductor, to facilitate the degradation of harmful pollutants in water [4], [6]. Unlike metals, which exhibit a continuous electronic state, semiconductors have a band gap (E_g) between their valence (VB) and conduction bands (CB) [3]. The band gap of semiconductors, typically narrower than those of insulators, represents the minimum amount of energy required to excite electrons (e^-) in the valence band to the conduction band. When semiconductors are exposed to light with energy equal to or greater than their E_g, their electrons are excited to the conduction band. This creates positive charges left behind in the valence band known as holes (h^+) [8]. The photogenerated charge carrier species: electrons and holes can subsequently participate in reduction and oxidation reactions which convert undesirable pollutants to innocuous materials such as CO_2 and H_2O [6], [9].

One of the most commonly used photocatalysts is titanium dioxide (TiO_2). This is due to its inert properties, high chemical stability, low toxicity, simple synthesis, and low post-processing demand [6], [10]. TiO_2 is also capable of degrading a plethora of organic pollutants. However, despite these many advantages, it is limited in its absorption of solar light due to its large band gap of 3.2 eV [10]. This constraints TiO_2 to only access UV light which accounts for a mere 4% of the solar spectrum [11]. As a result, its viability for water treatment applications is impaired, as it cannot be photoactivated by natural visible light (380-780 nm) [11]. Hence, modern research focused on photocatalytic water decontamination aims to enhance TiO_2's ability to absorb visible light and design novel photoactive materials that can access a larger portion of the visible solar spectra.

One class of compounds that has gained increasing interest in the field of photocatalytic water treatment is the Aurivillius family. These catalysts share several beneficial traits, including high photocatalytic stability, low toxicity, good conductivity, and considerable photoactivity [12]. One particular candidate from this group is bismuth tungstate (Bi_2WO_6). This catalyst is an n-type semiconductor with a band gap of 2.6-2.9 eV owing to its hierarchical structure consisting of perovskite-type tungstate (WO_4^{2-}) layers intertwined between bismuth oxide ($Bi_2O_2^{2+}$) units [13]. In addition to its low band gap, Bi_2WO_6 contains internal electric fields that facilitate good e^-/h^+ separation [13]. Nonetheless, bismuth tungstate is hindered by a high e^-/h^+ recombination rate [14]. As a result, for Bi_2WO_6 to be considered a viable candidate for water treatment, its charge carrier separation must be bolstered to ensure higher photoactivity.

Another category of compounds that has attracted attention is the bismuth oxyhalides, BiOX (X=Cl, Br, or I). These compounds can be described as having a crystalline structure consisting of bismuth oxide layers located within blocks of halogen atoms (Cl, Br, or I) [15]. One photocatalyst from this group which has been subject to recent research is bismuth oxychloride (BiOCl). Owing to its high photocatalytic stability and low toxicity in conjunction with its crystalline morphology, BiOCl has shown significant promise in recent water decontamination studies. However, its band gap of 3.2 eV limits its use in visible light applications [13], [14], [16].

Recently, a variety of techniques, including metal doping, control of nanostructure, and heterojunction synthesis, have been used to improve BiOCl's photocatalytic performance [16]. Among these methods, the formation of conjugate heterojunctions has led to a significant improvement in photoactivity. Typically, BiOCl is composited with other catalysts, including $BiVO_4$, Bi_2O_3, TiO_2, and Bi_2WO_6 [16], [17], [18], [19]. Typically, it is the case that effective heterojunctions are comprised of small band gap structures being paired with larger band gap structures [8], [16]. As such, Bi_2WO_6 shows particular promise to be composited with BiOCl. Additionally, bismuth tungstate displays good photostability and nontoxicity, which allows it to be effectively paired with bismuth oxychloride [16]. Several studies have shown that Bi_2WO_6/BiOCl heterojunctions display enhanced visible light response and high photoactivity [16], [20], [21], [22], [23], [24].

To further enhance the stability and activity of heterojunctions, noble metal deposition is often used [25], [26], [27]. Noble metals like Au, Ag, Pt, and Pd are commonly deposited on heterojunction catalysts to induce the surface plasmon resonance (SPR) effect to boost photocatalytic activity under visible light [25], [26], [27]. The deposition of noble metals on the surface of the photocatalyst has two major benefits, namely, increased responsiveness to visible light and suppressed charge carrier recombination [25], [26], [27]. This is due to the metal nanoparticles behaving as charge acceptors, preventing e^-/h^+ recombination. As such, noble metal deposition has emerged as a promising tool to boost the visible-light-driven activity of heterojunction photocatalysts [25], [26], [27]. Recently, Pd nanoparticles have been the most promising of the noble metals, and have been deposited on a variety of photocatalysts, leading to high photoactivity [26].

In this work, studies were conducted to determine optimal parameters in the synthesis of Bi_2WO_6/BiOCl heterojunctions through the analysis of photoactivity. A novel Pd nanoparticle-deposited Bi_2WO_6/BiOCl ternary heterojunction was also synthesized and optimized based on the visible light-driven degradation of an aqueous Rhodamine B (RhB) solution.

1.2 Project Objectives

To improve the visible light-driven performance of Bi_2WO_6/BiOCl, the following research objectives were pursued and are outlined as follows:

1. To optimize several synthesis parameters, including the ratio between Bi_2WO_6 and BiOCl, calcination temperature, and calcination time of the hydrothermal synthesis of Bi_2WO_6/BiOCl composite heterojunction.

2. To determine the optimal loading amount of palladium nanoparticles on the surface of Bi_2WO_6/BiOCl for the synthesis of a novel Pd-Bi_2WO_6/BiOCl ternary heterojunction.
3. To study the effect of operation parameters on the performance of the novel Pd-Bi_2WO_6/BiOCl photocatalyst through the optimization of catalyst dosage, degradation temperature, initial pH, initial concentration of RhB, and catalyst recyclability.
4. To study the size, composition, morphology, optical, and adsorption properties of Bi_2WO_6/BiOCl and Pd-Bi_2WO_6/BiOCl using X-ray diffraction (XRD), X-ray photoelectron spectroscopy (XPS), scanning electron microscopy (SEM), ultraviolet-visible diffused reflectance spectroscopy (UV-vis DRS), and N_2 sorption testing.

1.3 Thesis Outline

This thesis consists of five sections which are dedicated to introduction, literature review, experimental findings, and conclusions; all of which are divided into separate chapters as detailed below:

- **Chapter 1: Introduction**

  In this chapter, a brief introduction to the principles of semiconductor photocatalysis, the importance of effective water treatment, and the overall objectives of the thesis are presented.

- **Chapter 2: Literature Review**

  This chapter will offer an in-depth literature review into the principles of photocatalytic water treatment, various preparation techniques for Bi_2WO_6/BiOCl, and noble metal loading for surface plasmon resonance-enhanced photocatalytic performance.

- **Chapter 3: Optimization of Synthesis Conditions of Hydrothermal-Prepared Bi_2WO_6/BiOCl Composite Heterojunctions**

  During the first phase of the research, synthesis parameters including the Bi_2WO_6:BiOCl composition ratio, calcination temperature, and calcination time were studied to optimize the hydrothermal synthesis of Bi_2WO_6/BiOCl.

- **Chapter 4: Palladium Modified Bi_2WO_6/BiOCl Composite Heterojunctions for Enhanced Water Treatment**

  Palladium nanoparticles were deposited on the previously optimized Bi_2WO_6/BiOCl via a photodeposition technique to synthesize a novel Pd-Bi_2WO_6/BiOCl ternary heterojunction. The effects of several operational parameters were examined to strengthen the visible light-driven photocatalysis of RhB. A possible degradation pathway and mechanism were also proposed.

- **Chapter 5: Conclusions and Recommendations**

  The major findings and conclusions of the work are presented, and recommendations for future work are offered.

1.4 Nomenclature

Eg	Band gap energy
$Bi_2O_2^{2+}$	Bismuth oxide
BiOCl	Bismuth oxychloride
BiOX	Bismuth oxyhalide
Bi_2WO_6	Bismuth tungstate
CO_2	Carbon dioxide
e^-	Electron
h^+	Hole
N_2	Nitrogen
Pd	Palladium
TiO_2	Titanium dioxide
WO_4^{2-}	Tungstate anion
H_2O	Water

1.5 Abbreviations

AOP	Advanced Oxidation Process
BET	Brunauer-Emmett-Teller
CB	Conduction Band
DRS	Diffuse Reflectance Spectroscopy
eV	Electron Volts
RhB	Rhodamine B
SEM	Scanning Electron Microscopy
SPR	Surface Plasmon Resonance

UV	Ultraviolet
UV-vis	Ultraviolet Visible
VB	Valence Band
XPS	X-ray Photoelectron Spectroscopy
XRD	X-ray Diffraction

References

[1] M. A. Al-Nuaim, A. A. Alwasiti, and Z. Y. Shnain, “The photocatalytic process in the treatment of polluted water,” *Chemical Papers 2022 77:2*, vol. 77, no. 2, pp. 677–701, Oct. 2022, doi: 10.1007/S11696-022-02468-7.

[2] E. Koncagül and R. Connor, “The United Nations World Water Development Report 2023: partnerships and cooperation for water; facts, figures and action examples,” Paris, 2023.

[3] S. Mishra and B. Sundaram, “A review of the photocatalysis process used for wastewater treatment,” *Mater Today Proc*, Jul. 2023, doi: 10.1016/J.MATPR.2023.07.147.

[4] G. Crini and E. Lichtfouse, “Advantages and disadvantages of techniques used for wastewater treatment,” *Environ Chem Lett*, vol. 17, no. 1, pp. 145–155, Mar. 2019, doi: 10.1007/s10311-018-0785-9.

[5] A. O. Oluwole, E. O. Omotola, and O. S. Olatunji, “Pharmaceuticals and personal care products in water and wastewater: a review of treatment processes and use of photocatalyst immobilized on functionalized carbon in AOP degradation,” *BMC Chem*, vol. 14, no. 1, p. 62, Dec. 2020, doi: 10.1186/s13065-020-00714-1.

[6] G. Ren *et al.*, “Recent Advances of Photocatalytic Application in Water Treatment: A Review,” *Nanomaterials 2021, Vol. 11, Page 1804*, vol. 11, no. 7, p. 1804, Jul. 2021, doi: 10.3390/NANO11071804.

[7] S. K. Loeb *et al.*, “The Technology Horizon for Photocatalytic Water Treatment: Sunrise or Sunset?,” *Environ Sci Technol*, vol. 53, no. 6, pp. 2937–2947, Mar. 2019, doi: 10.1021/ACS.EST.8B05041.

[8] M. M. Ayyub and C. N. R. Rao, “Design of efficient photocatalysts through band gap engineering,” in *Nanostructured Photocatalysts*, Elsevier, 2020, pp. 1–18. doi: 10.1016/B978-0-12-817836-2.00001-6.

[9] S. Mishra and B. Sundaram, “A review of the photocatalysis process used for wastewater treatment,” *Mater Today Proc*, Jul. 2023, doi: 10.1016/j.matpr.2023.07.147.

[10] S. Y. Lee and S. J. Park, “TiO2 photocatalyst for water treatment applications,” *Journal of Industrial and Engineering Chemistry*, vol. 19, no. 6, pp. 1761–1769, Nov. 2013, doi: 10.1016/J.JIEC.2013.07.012.

[11] L. Wang and J. Yu, “Principles of photocatalysis,” 2023, pp. 1–52. doi: 10.1016/B978-0-443-18786-5.00002-0.

[12] D. O. Charkin, D. N. Lebedev, and S. M. Kazakov, “Multiple cation and anion substitutions into the structures of Bi2WO6 and PbBi3WO8Cl,” *J Alloys Compd*, vol. 536, pp. 155–160, Sep. 2012, doi: 10.1016/J.JALLCOM.2012.04.113.

[13] Z. Zhu *et al.*, “Recent progress in Bi_2WO_6-Based photocatalysts for clean energy and environmental remediation: Competitiveness, challenges, and future perspectives,” *Nano Select*, vol. 2, no. 2, pp. 187–215, Feb. 2021, doi: 10.1002/nano.202000127.

[14] Z. Li, L. Zhu, W. Wu, S. Wang, and L. Qiang, “Highly efficient photocatalysis toward tetracycline under simulated solar-light by Ag+-CDs-Bi2WO6: Synergistic effects of silver ions and carbon dots,” *Appl Catal B*, vol. 192, pp. 277–285, Sep. 2016, doi: 10.1016/j.apcatb.2016.03.045.

[15] X. Yu, J. Yang, K. Ye, X. Fu, Y. Zhu, and Y. Zhang, “Facile one-step synthesis of BiOCl/BiOI heterojunctions with exposed {001} facet for highly enhanced visible light photocatalytic performances,” *Inorg Chem Commun*, vol. 71, pp. 45–49, Sep. 2016, doi: 10.1016/J.INOCHE.2016.06.034.

[16] Z. Liang, C. Zhou, J. Yang, Q. Mo, Y. Zhang, and Y. Tang, “Visible light responsive Bi 2 WO 6 /BiOCl heterojunction with enhanced photocatalytic activity for degradation of tetracycline and rohdamine B,” *Inorg Chem Commun*, vol. 93, pp. 136–139, Jul. 2018, doi: 10.1016/j.inoche.2018.05.022.

[17] G. Zhang, Y. Tan, Z. Sun, and S. Zheng, “Synthesis of BiOCl/TiO 2 heterostructure composites and their enhanced photocatalytic activity,” *J Environ Chem Eng*, vol. 5, no. 1, pp. 1196–1204, Feb. 2017, doi: 10.1016/j.jece.2017.01.040.

[18] Q. Su *et al.*, “Construction of a Bioinspired Hierarchical $BiVO_4$/BiOCl Heterojunction and Its Enhanced Photocatalytic Activity for Phenol Degradation,” *ACS Appl Mater Interfaces*, vol. 13, no. 28, pp. 32906–32915, Jul. 2021, doi: 10.1021/acsami.1c05117.

[19] X. Zhang, G. Xu, J. Hu, J. Lv, J. Wang, and Y. Wu, “Fabrication and photocatalytic performances of BiOCl nanosheets modified with ultrafine Bi_2O_3 nanocrystals,” *RSC Adv*, vol. 6, no. 68, pp. 63241–63249, 2016, doi: 10.1039/C6RA09919J.

[20] N. Tahmasebi, Z. Maleki, and P. Farahnak, “Enhanced photocatalytic activities of Bi2WO6/BiOCl composite synthesized by one-step hydrothermal method with the assistance of HCl,” *Mater Sci Semicond Process*, vol. 89, pp. 32–40, Jan. 2019, doi: 10.1016/j.mssp.2018.08.026.

[21] Y. Huang *et al.*, “Peroxymonosulfate Activation by Bi2WO6/BiOCl Heterojunction Nanocomposites under Visible Light for Bisphenol A Degradation,” *Nanomaterials*, vol. 11, no. 11, p. 3130, Nov. 2021, doi: 10.3390/nano11113130.

[22] M. Guo *et al.*, “Bi2WO6–BiOCl heterostructure with enhanced photocatalytic activity for efficient degradation of oxytetracycline,” *Sci Rep*, vol. 10, no. 1, p. 18401, Oct. 2020, doi: 10.1038/s41598-020-75003-x.

[23] L. Derikvand and N. Tahmasebi, “Synthesis and photocatalytic performance of Bi2WO6/BiOX (X=Cl, Br, I) composites for RhB degradation under visible light,” *Korean Journal of Chemical Engineering*, vol. 38, no. 1, pp. 163–169, Jan. 2021, doi: 10.1007/s11814-020-0687-y.

[24] J. Chen *et al.*, “Preparation of BiOCl/Bi2WO6 Photocatalyst for Efficient Fixation on Cotton Fabric: Applications in UV Shielding and Self-Cleaning Performances,” *Materials*, vol. 14, no. 22, p. 7002, Nov. 2021, doi: 10.3390/ma14227002.

[25] A. Nazir, P. Huo, H. Wang, Z. Weiqiang, and Y. Wan, “A review on plasmonic-based heterojunction photocatalysts for degradation of organic pollutants in wastewater,” *J Mater Sci*, vol. 58, no. 15, pp. 6474–6515, Apr. 2023, doi: 10.1007/s10853-023-08391-w.

[26] Z. Li and X. Meng, “Recent development on palladium enhanced photocatalytic activity: A review,” *J Alloys Compd*, vol. 830, p. 154669, Jul. 2020, doi: 10.1016/j.jallcom.2020.154669.

[27] M. Arumugam, R. Koutavarapu, K.-K. Seralathan, S. Praserthdam, and P. Praserthdam, “Noble metals (Pd, Ag, Pt, and Au) doped bismuth oxybromide photocatalysts for improved visible light-driven catalytic activity for the degradation of phenol,” *Chemosphere*, vol. 324, p. 138368, May 2023, doi: 10.1016/j.chemosphere.2023.138368.

Chapter 2: Literature Review

2.1 Introduction

Over the past several decades, rapid industrial and population growth has led to a greater demand for clean water sources. According to the United Nations, roughly 750 million people worldwide lack access to proper drinking water [2]. Additionally, the industrial demand for water is expected to grow four-fold by 2050 [2]. As such, the development of water treatment technologies that are able to meet these challenges is of vital importance in the 21st century.

Traditionally, processes such as membrane separation, flocculation, coagulation, sedimentation, and filtration have been used for water treatment [9]. However, many of these existing technologies fall short of providing complete treatment of organic pollutants [1]. Recently, advanced oxidation processes (AOPs), including ozone, UV, and photocatalytic treatment, have sought to provide complete degradation of organic and inorganic water pollutants. These processes utilize hydroxyl radicals (•OH), degrading pollutants into innocuous materials like H_2O and CO_2 [9], [11], [28]. Among the AOPs, semiconductor photocatalysis has emerged as a promising candidate for water treatment.

Photocatalysis, considered a green technology, utilizes solar energy to generate oxidative active species that can degrade pollutants in water via a sequence of redox reactions. Recently, heterogeneous photocatalysis has gained growing attention due to its high efficiency in degrading many organic pollutants. This is attributed to its non-selective nature, allowing it to target a wide range of contaminants [28]. Since the extent of the degradation depends on the internal electrical properties of the semiconductor, the selection of the photocatalyst is crucial. Historically, TiO_2 has been regarded as an ideal photocatalyst due to its high stability, simple synthesis, nontoxicity, and low cost [29]. However, due to its wide band gap (>3.2 eV), it can only be photoactivated by ultraviolet radiation [30]. This makes it impractical to use for many water treatment processes that rely on visible-light-driven photocatalysis. As such, it is important to develop novel photocatalysts with narrow band gaps that allow them to access the visible light spectrum. Among these, Bi_2WO_6/BiOCl has shown potential in providing effective, visible-light-driven treatment of organic pollutants in water. The following chapter provides a detailed review of Bi_2WO_6/BiOCl as a candidate for photocatalytic water treatment.

2.2 History of Photocatalysis

Photocatalysis refers to the initiation or acceleration of a chemical reaction in the presence of a compound (a catalyst) that activates upon absorbing light of the appropriate wavelength. The term *photocatalysis* was first coined in 1911, when German chemist Alexander Eibner described his work on illuminating zinc oxide (ZnO) for bleaching Prussian blue dye [31]. Over the next several decades, researchers began developing the basic concepts of light-activated catalysts. In 1938, Kitchener and Goodeve demonstrated that titanium dioxide, when photoactivated by UV light, could serve as a photosensitizer for dye bleaching [32]. This discovery was significant as it revealed that UV radiation could generate active oxygen species on the surface of the catalyst, leading to the breakdown of organic compounds. To this day, TiO_2 remains a widely used photocatalyst for various applications, including water treatment, self-cleaning surfaces, and hydrogen evolution. For much of the next several years, photocatalysis was seldom studied due to a lack of applications of the young technology. However, it was Filimonov's work on isopropanol photooxidation with ZnO and TiO_2 that reignited interest in the field [33]. This led to a major breakthrough in 1972, when Japanese chemists Kenichi Honda and Akira Fujishima reported hydrogen evolution from water using a TiO_2 anode connected to a platinum cathode [34]. It was observed that when TiO_2 absorbed UV light, it induced the flow of electrons, resulting in the production of H_2 gas [34]. This showed that photocatalysis could offer an effective, clean, and cost-effective approach to environmental applications. Presently, photocatalysis is used for a plethora of applications, including water splitting, self cleaning surfaces, hydrogen generation, air filtration, and water treatment. Among them, water treatment remains one of the most widely used applications. The following section will delve into the fundamental concepts of photocatalytic water treatment.

2.3 Fundamentals of Photocatalytic Water Treatment

The following passage will discuss the fundamental theories and concepts related to photocatalytic water treatment. Belonging to the broader class of advanced oxidation processes, photocatalytic water decontamination involves the generation of hydroxyl radicals to decompose organic pollutants into innocuous materials like CO_2 and H_2O [11], [35]. Several AOPs have been considered for water treatment, including the Fenton and photolytic processes. These processes are largely dependent on UV activation to produce hydroxyl and oxidative radicals, respectively. These technologies have shown the potential to efficiently degrade a wide array of organic and inorganic pollutants. However, due to their dependence on UV light, they are often expensive and energy-intensive processes [9], [36].

To address the challenges incurred by the other AOPs, heterogeneous photocatalysis has emerged as a promising candidate for water treatment. Heterogeneous photocatalysis, which typically consists of solid and liquid phases, can be found in a plethora of fields, including heavy metal removal, photoreduction, cancer treatment, and water splitting. Most heterogeneous photocatalysts are classified as semiconductors. Therefore, to understand the physicochemical properties of photocatalysts, it is necessary to discuss their band structure.

The electron band structure of a material, specifically a semiconductor, refers to the possible energy levels at which an electron is permitted and prohibited from occupying energy bands and band gaps, respectively. In contrast to metals, which exhibit a continuous electronic state, semiconductors possess a band gap between their valence band (VB) and conduction band (CB) [8], [11], [37], [38]. The valence band is filled with electrons located in the outermost regions of the atomic structures [8], [35]. Consequently, the VB is the most energetic level and influences the oxidative capacity of the semiconductor. In contrast, the conduction band represents the reductive capacity of a semiconductor as it is the lowest unoccupied molecular orbital [8]. The band gap, the energy difference between the top of the valence band and the bottom of the conduction band, also represents the minimum amount of energy required to excite electrons from the VB to the CB. As such, photons containing energy equal to or greater than the E_g of a semiconductor photocatalyst can excite electrons from the VB to the CB, initiating photocatalysis [20], [37].

The band gap of a semiconductor (E_g) and its absorbance-edge wavelength ($\lambda_{\text{absorbance-edge}}$) can be expressed using the Planck relations as described in Equations 2-1 and 2-2 [39]:

$$E_g(\text{eV}) = \frac{1240}{\lambda_{\text{absorbance-edge}}} \tag{2-1}$$

$$\lambda_{\text{absorbance-edge}}(\text{nm}) = \frac{1240}{E_g} \tag{2-2}$$

As seen in the equation above, the lower the bandgap of a semiconductor, the larger the wavelength of light that can activate it. This, however, does not necessarily mean that ideal photocatalysts should have very small band gaps. This is because as the band gap begins to get smaller, the reductive and oxidative capabilities of the semiconductor decrease, and a greater e^-/h^+ recombination rate would occur [37], [40]. As such, when designing a suitable photocatalyst, it is important to narrow the band gap to a value that would still allow for good redox capabilities as well as limited charge carrier recombination.

Using the electronegativity theory proposed by Mulliken, the band positions of the conduction band (CB) and valence band (VB) can be calculated as presented in Equations 2-3 and 2-4, respectively [35].

$$E_{CB}= \chi_p\text{-}E^e\text{-}0.5E_g \tag{2-3}$$

$$E_{VB} = E_{CB}+E_g \tag{2-4}$$

Where, E_{CB}, E_{VB}, and E_g represent the position of the conduction band edge, valence band edge and the band gap. χ_p represents the semiconductor electronegativity and E^e represents the free electron energy using the hydrogen scale (~4.5 vs. NHE).

Due to the photoactivity of catalysts being heavily influenced by environmental and operating conditions, such as the source of light, temperature, and pH, it is important to determine a common parameter that can be used to compare the performance of different photocatalytic systems. Such a parameter exists in the actual quantum yield (F). Expressed as a percentage, the quantum yield represents the number of reacted electrons (N_R) over the overall amount of photon absorbance from the light source (N_A). This relation is summarized in Equation 2-5 below [11].

$$F = \frac{N_R}{N_A}\times 100\% \tag{2-5}$$

It is important to note that in heterogeneous systems, as a result of light scattering on the photocatalyst surface, the actual quantum yield (F) can be difficult to measure. As such, an assumption is usually made that all of the incident photons are absorbed, giving the apparent quantum yield as [11]:

$$F' = \frac{N_R}{N_I}\times 100\% \tag{2-6}$$

The apparent quantum yield is typically lower than the actual quantum yield as the amount of incident photons from the light source is greater than the number of photons that are absorbed. The quantum yield is affected by other parameters, including the rates of charge transfer (k_{CT}) and electron hole recombination (k_R). This relationship is reflected in Equation 2-7 below [35]:

$$F \propto \frac{k_{CT}}{k_{CT} + k_R} \tag{2-7}$$

In the absence of any charge carrier recombination, the quantum yield would assume a value of unity (100%). However, in a real heterogeneous system, the recombination rate is considerable, rendering the quantum yield value less than 100%. Ensuring a low recombination rate remains one of the key challenges faced in modern photocatalytic systems [11], [35].

In order to assess the performance of a photocatalyst in a laboratory setting, the degradation efficiency (E) is often used [35], [38], [41]:

$$E(\%) = \frac{c_0 - c_t}{c_0} \times 100\% \tag{2-8}$$

Where c_0 and c_t represent the initial substrate concentration and the substrate concentration at a given time (t), respectively.

The concentration of the substrate being degraded is often converted to the absorbance value corresponding to its characteristic peak. This relationship is given by the Beer-Lambert law expressed in Equation 2-9 below [41]:

$$A = alc \tag{2-9}$$

Where, A, a, l, and c are the absorbance, molar absorptivity, path length of irradiation, and concentration of substrate, respectively.

2.4 Photocatalytic Decontamination of Organic Pollutants in Water

A typical photocatalytic water degradation process involves several key steps. Firstly, because all of the redox reactions occur on the photocatalytic surface, the target pollutant must be adsorbed by the catalyst [42], [43]. Next, the photogeneration of the electron-hole pair occurs when the semiconductor photocatalyst absorbs light photons of energy greater than or equal to its band gap. This initiates *photoexcitation,* whereby the electrons in the valence band jump to the conduction band, creating positively charged holes in their place [40]. The generation of these charge carrier species (holes and electrons) is crucial for the photocatalytic process as they are strong oxidizing and reducing agents, respectively. As will be mentioned later in the chapter, the selection of the light source must match the band gap of the photocatalyst to ensure proper photogeneration of the e^-/h^+ pair [44]. Furthermore, the e^- and h^+ generated via photoexcitation are generally non-selective in terms of their degradation of organic and inorganic pollutants due to their strong reduction and oxidizing potentials. This characteristic makes photocatalysis an attractive tool for the degradation of a variety of pollutants in water. However, it is also important to note that the lifespan of the separated e^-/h^+ pair spans only several nanoseconds, leading to two competing mechanisms that define the next step and influence the effectiveness of the overall process: charge recombination and charge separation [45].

During charge recombination, electrons and holes recombine either in the bulk of the photocatalyst or on its surface, producing heat as a by-product. This phenomenon is a direct result of the coulombic forces that exist between the charges and is a thermodynamically favourable process [46]. The second possibility involves charge separation, where the photogenerated e^-/h^+ pair separates and migrates to the surface of the catalyst, where they can subsequently participate in redox reactions. Once the charge carrier species have reached the photocatalytic surface, they may participate in decomposing the pollutant substrates [40], [42].

During a typical photoreaction, holes and electrons are involved in photooxidation and photoreduction, respectively. Photooxidation occurs when the h^+ remaining in the VB interacts with adsorbed H_2O and OH^- molecules acting as donor molecules, forming hydroxyl (•OH) radicals [43], [47]. Since •OH is a highly reactive oxidizing agent with a standard oxidizing potential of 2.8 V, it is nonselective and capable of decomposing many pollutants [43]. Additionally, a certain amount of the h^+ present in the VB can directly oxidize pollutants to produce intermediates, which are subsequently converted into simple products. Simultaneously, e^- present in the CB react with O_2, forming highly oxidative superoxide ions ($O_2^{\bullet -}$), which are also capable of decomposing organic pollutants via a sequence of reactions [40], [43], [47].

This overall process results in the mineralization and decomposition of the initial organic substrate into simple-non-toxic products such as H_2O and CO_2. The complete mechanism and diagram describing the photocatalytic decomposition of organic pollutants in water are provided as follows [40], [45], [46], [48].

Step 1: Photoexcitation and generation of e^-/h^+ pair

$$\text{Photocatalyst} + (h\nu \geq E_g) \rightarrow e^- + h^+ \tag{2-10}$$

$$h^+ + \text{organic pollutant}_{\text{adsorbed}} \rightarrow \text{organic pollutant}^{\bullet +}_{\text{adsorbed}} \tag{2-11}$$

Step 2: Photooxidation and Photoreduction

$$H_2O + h^+ \rightarrow H^+ + \bullet OH \tag{2-12}$$

$$h^+ + OH^- \rightarrow \bullet OH \tag{2-13}$$

$$O_2 + e^- \rightarrow O_2^{\bullet -} \quad (2\text{-}14)$$

$$O_2^{\bullet -} + \bullet OH \rightarrow \bullet OOH \quad (2\text{-}15)$$

Step 3: Oxidation and Reduction of Other Radical Species

$$H_2O_2 + H^+ \rightarrow \bullet OOH + H_2O \quad (2\text{-}16)$$

$$h^+ + \text{organic pollutant}_{\text{adsorbed}} \rightarrow \text{organic pollutant}^{\bullet +}_{\text{adsorbed}} \quad (2\text{-}17)$$

Step 4: Attacking of Pollutants

$$\text{organic pollutant}_{\text{adsorbed}} + \bullet OH,\ h^+, \bullet OOH \text{ or } O_2^{\bullet -} \rightarrow \text{intermediates and products} \quad (2\text{-}18)$$

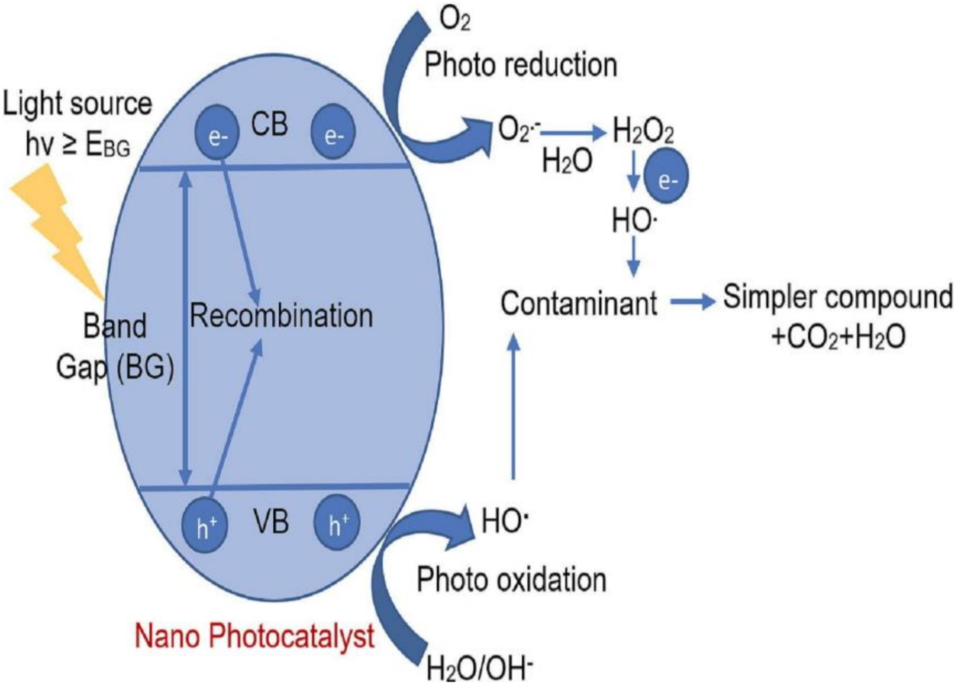

Figure 2-1: Diagram of photocatalytic degradation mechanism [9].

2.5 Photocatalytic Degradation Kinetics

In addition to the photocatalytic mechanism mentioned in the previous section, it is also important to understand the reaction kinetics. Since most photocatalytic degradation (PCD) reactions involve a solid-liquid phase, they can be categorized as being part of a heterogeneous catalytic system [49].

Consequently, the kinetics for the photodegradation of organic pollutants follow the Langmuir-Hinshelwood (L-H) model and assume pseudo-first-order kinetics [46], [49]. The use of the L-H model in characterizing the degradation kinetics of photocatalytic systems has been extensively studied in the literature. The following passage describes the L-H model and the corresponding equations [11], [35], [46], [49].

First, the effect of the initial substrate (i.e. organic pollutant) concentration and the rate of degradation (r) is given as:

$$r = -\frac{dc}{dt} = \frac{k_r Kc}{1+Kc} \tag{2-19}$$

Where, c (mg/L) is the concentration of the substrate at a given time t (min), k_r is the actual rate constant (mg L^{-1} min^{-1}) and K is the adsorption equilibrium constant (L mg^{-1}).

In most cases the initial concentration of the organic pollutant being degraded is on the scale of mg/L (ppm), as such the Kc term is deemed negligible such that pseudo-first order kinetics are applied,

$$1 + Kc \approx 1 \tag{2-20}$$

Applying the assumption to Equation 2-20 gives,

$$r = -\frac{dc}{dt} = k_r Kc \tag{2-21}$$

letting $k_{app} = k_r K$ gives,

$$r = -\frac{dc}{dt} = k_{app} c \tag{2-22}$$

where k_{app} (min^{-1}) is the product of the adsorption equilibrium constant and the actual rate constant and is defined as the apparent rate constant. Generally, k_{app} is referred to as the reaction rate constant due to PCD usually operating at dilute pollutant concentrations ($c_0 < 10^{-3}$ mol/L)

Next, applying an integration on Equation 2-22 using the following boundary conditions as: $c = c_0$ at $t=0$ and $c=c$ when $t=t$, with c being the substrate concentration at time t.

$$\ln\left(\frac{c_0}{c}\right) = k_{app}t \qquad (2\text{-}23)$$

Where, c_0 and c are defined as the initial substrate concentration and substrate concentration at a given time, respectively.

2.6 Effect of Operational Parameters on Photocatalytic Degradation Kinetics

The following section will discuss the importance of several key operational parameters which influence the overall rate of degradation and the kinetics discussed in the previous section.

2.6.1: Catalyst Dosage

Catalyst dosage is the amount of photocatalyst that is used for a photodegradation reaction. This parameter is important, as the performance of the photodegradation process is directly linked to the amount of catalyst injected into the system [11], [50]. Moreover, when considering the economic feasibility of the process, it is desirable to minimize the amount of catalyst used to reduce the cost of operations. Initially, an increase in the catalyst dosage enhances the rate of degradation due to a higher number of photogenerated e^- and h^+ available to participate in redox reactions that degrade target pollutants [50]. Furthermore, a greater number of photocatalysts in the system increases the total active site surface area, leading to an increased rate of degradation. However, once the dosage surpasses an optimum value, the rate will eventually decrease with any additional catalyst added. This is because excess catalyst can cause clustering [51], blocking light penetration. This results in the scattering of photons, causing less light to be absorbed by the catalyst, resulting in a decrease of photocatalytic activity [11], [23], [50].

2.6.2: Initial Organic Pollutant Concentration

The initial amount of target organic pollutant required to be degraded in the aqueous solution will influence the overall photodegradation rate. It has been reported that at low levels, increasing the concentration of the pollutant can cause an increase in the rate of degradation [11], [23], [47]. However, if the pollutant concentration is too high, a decline will be observed in the photocatalytic activity. This phenomenon can be attributed to an increased demand for oxidizing species (•OH and $O_2^{\bullet-}$) due to the elevated pollutant levels. Therefore, with an increased number of pollutant molecules adsorbed on the catalyst surface, fewer active sites are available to adsorb the hydroxyl ions needed to produce the hydroxyl radicals involved in the degradation of the pollutant. As a result, the rate of degradation will decline [11], [49].

2.6.3: Initial pH

The pH of photocatalytic systems plays an important role in the rate of reaction. This is because the pH can impact the surface charge of the photocatalyst [11]. Moreover, the pH can dictate the band position of the semiconductor catalyst. Typically, organic pollutants exhibit neutral behaviour when the pH of the solution is lower than their acid dissociation constant (pKa) [52], [53]. As the pH increases to values greater than the pollutant's pKa, the compound will begin to deionize and will acquire a negative charge. As a result, the pH will influence how the pollutant aggregates and its ability to be absorbed by the catalyst [46], [52], [53]. The pH can also influence the photocatalyst itself. This is because, in acidic conditions, the predominant oxidizing species present in the solution are typically holes. Whereas, in neutral to alkaline conditions, the photocatalyst is able to generate a greater number of hydroxyl radicals, which will have a greater impact on the degradation of the target molecule [46]. As •OH displays a significant oxidation potential, it may be desirable to operate the system in alkaline conditions. However, it is important to note that at higher pH, •OH radicals may be scavenged due to a greater amount of OH^- anions, suppressing the rate of degradation. As a result, it is important to determine the optimal initial pH to ensure good photocatalytic activity [11], [46], [52], [53].

2.6.4: Temperature

One of the several benefits of aqueous photocatalytic systems is that they can be operated in ambient conditions due to photonic activation. This is beneficial as it limits excessive energy expenditure related to external heating. It has been established that most aqueous photocatalytic systems involved in the decontamination of organic pollutants exhibit an optimal temperature range of 20-80°C [11], [54]. This wide temperature range indicates that photocatalysts are less sensitive to temperature changes compared to changes in concentration and pH. It is important to note that increases in temperature within the optimum range can lead to increased activity. However, it has been reported that as the temperature increases, there is an increased suppression of e^-/h^+ separation [54]. Moreover, temperatures greater than 80°C can negatively impact the adsorption capability of the photocatalyst, resulting in a decrease in the adsorption of the target pollutant [55]. Additionally, elevated temperatures can lead to the desorption of adsorbed substrate, lowering the rate of degradation. As such, photocatalytic water treatment systems are typically conducted at ambient temperature [46], [54], [55].

2.7 BiOCl

As photocatalysis continues to be explored for water treatment applications, one group of materials that has gained growing attention is the bismuth oxyhalides, BiOX (X=Cl, Br, or I). These compounds are recognized for their impressive photocatalytic properties, including high photoactivity and low charge carrier recombination [56], [57]. Bismuth oxyhalides are described as having a layered-crystalline structure consisting of [X-Bi-O-Bi-X] units located in between blocks of halogen atoms (X=Cl, Br, or I) [56]. Due to this layered framework, bismuth oxyhalide exhibits excellent optical and electronic properties, making it attractive for photocatalytic applications. A compound from this class that has garnered recent attention is bismuth oxychloride (BiOCl).

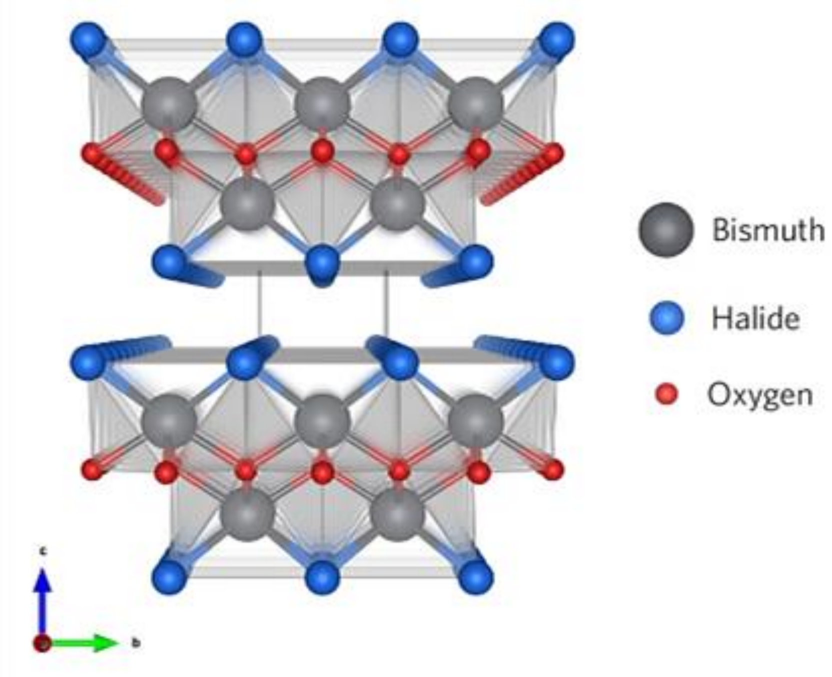

Figure 2-2: Schematic representation of the structure of bismuth oxyhalide [56].

As shown in Figure 2-2, BiOCl can be characterised as a ternary bismuth-based semiconductor consisting of group V-VI-VII elements with an open layered presentation composed of repeating units of [Cl-Bi-O-Bi-Cl] [56], [57]. These units are held in place by van der Walls (VDW) interactions with Cl atoms. Each unit of [Cl-Bi-O-Bi-Cl] contains a Bi atom surrounded by four Cl atoms and four O atoms, creating a conical decahedral morphology [57]. This arrangement allows for an increased area for atoms and orbitals to polarize upon excitation, creating internal electric fields in the [100] plane, leading to efficient separation of electrons and holes. Since the conical decahedral morphology of BiOCl enables efficient e^-/h^+ separation upon exposure to light of the appropriate wavelength [56]. The induced internal electric fields trigger the movement of e^- between the layered structure, promoting the efficient separation of h^+ and e^-. The presence of internal electrostatic fields limits the charge recombination ratio, making BiOCl a promising candidate for photocatalytic applications [17], [56], [57].

However, BiOCl has also been known to be limited in its pure form. Due to its wide band gap of 3.2 eV, bismuth oxychloride is not an effective semiconductor under visible light, limiting its suitability for visible light-driven photocatalysis and restricting its application [17]. Therefore, it is important to consider techniques to enhance the visible light responsiveness of this catalyst. Presently, several methods are being explored in the literature to boost the photoactivity of BiOCl under visible light. These include elemental doping, the creation of oxygen vacancies, strain modulation, the use of co-catalysts, and the formation of composite heterojunctions [22], [37]. Among these, the construction of heterojunctions has shown great promise in boosting the visible-light photoactivity of BiOCl. As shown in Figure 2-3, such a technique involves the compositing of two photocatalysts with different band structures at their interfaces to promote greater charge carrier generation and separation [37], [57]. Several studies have shown that the formation of heterojunctions involving BiOCl has several advantageous properties, including increased photochemical stability, greater charge carrier separation, decreased e^-/h^+ recombination, and increased visible light responsiveness. These properties have allowed BiOCl-based heterojunctions to display enhanced photocatalytic activity [18], [21], [58].

When selecting photocatalysts for composites, it is important to note that it is the difference in band gaps and band positions between the two photocatalysts that allows for the formation of a heterojunction and thus improves e^-/h^+ separation and photoactivity [37]. As such, suitable pairs typically involve large band gap structures composited with smaller band gap structures. Recently, BiOCl has been composited with several other semiconductors, including $BiVO_4$, Bi_2O_3, TiO_2, and Bi_2WO_6 [17], [19], [24], [56], [57]. Among these, the pairing of BiOCl with Bi_2WO_6 has shown great potential. The following section will describe the structure and properties of Bi_2WO_6, highlighting its suitability for heterojunction formation with BiOCl.

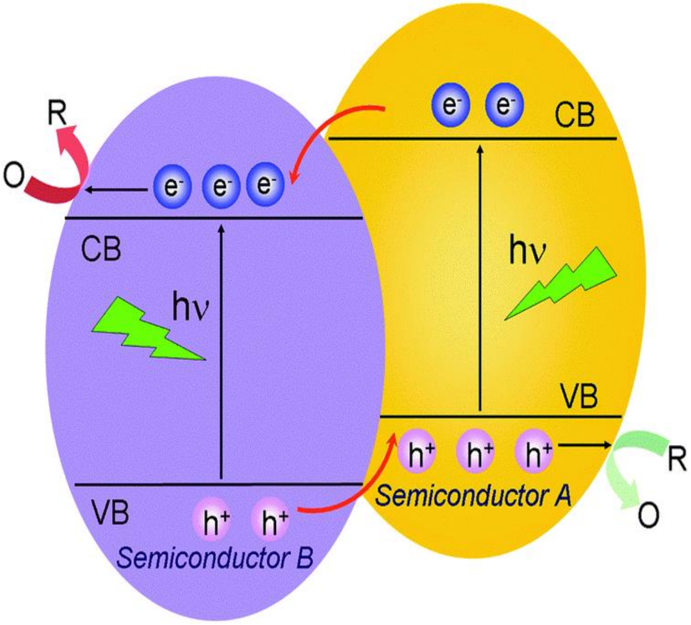

Figure 2-3: Schematic diagram of a typical heterojunction formation between two catalysts of different band gaps [37].

2.8 Bi_2WO_6

Belonging to the Aurivillius family, bismuth tungstate (Bi_2WO_6) is represented by the chemical formula $Bi_2A_{n-1}B_nO_{3n+1}$ [44]. As shown in Figure 2-4 below, Bi_2WO_6 exhibits an n-type perovskite structure consisting of alternating ionic layers of $[Bi_2O_2]^{2+}$ intertwined with octahedral layers of $[WO_4]^{2-}$ [44]. The valence band of Bi_2WO_6 comprises a combination of bismuth-6s and oxygen-2p atomic orbitals. The conduction band is composed of the 5d orbital of tungsten atoms. This results in a band structure consisting of a band gap ranging from 2.6 to 2.9 eV [12]. As a result, Bi_2WO_6 possesses excellent visible light responsiveness due to its ability to absorb larger wavelengths of light. Additionally, bismuth tungstate benefits from internal electric fields, which facilitate considerable charge carrier separation. Despite its excellent electronic properties, this catalyst suffers from a high e^-/h^+ recombination ratio, limiting its photocatalytic performance [12], [44].

As mentioned in the previous section, Bi_2WO_6 has recently been considered as a candidate to be composited with BiOCl. There are several reasons why bismuth tungstate pairs well with bismuth oxychloride. The typical absorption band edges for Bi_2WO_6 can pair with those of BiOCl to form a heterojunction. Additionally, both catalysts have a layered morphology consisting of ionic layers of $[Bi_2O_2]^{2+}$ wedged in between blocks of either Cl or $[WO_4]^{2-}$ ions, allowing for a good match [22], [23]. In terms of their properties, Bi_2WO_6 increases the visible light responsiveness, which is lacking for BiOCl. Conversely, the excellent electron-hole separation of BiOCl addresses the high recombination ratio hindering Bi_2WO_6. Furthermore, it has been reported that among the candidates that have been composited with BiOCl, Bi_2WO_6 displays excellent chemical stability. As a result, the physical and structural compatibility of BiOCl and Bi_2WO_6 allows them to form effective composite heterojunctions for the degradation of organic pollutants [22], [23], [51]. The following section will discuss the synthesis methods that have been used to form this heterojunction.

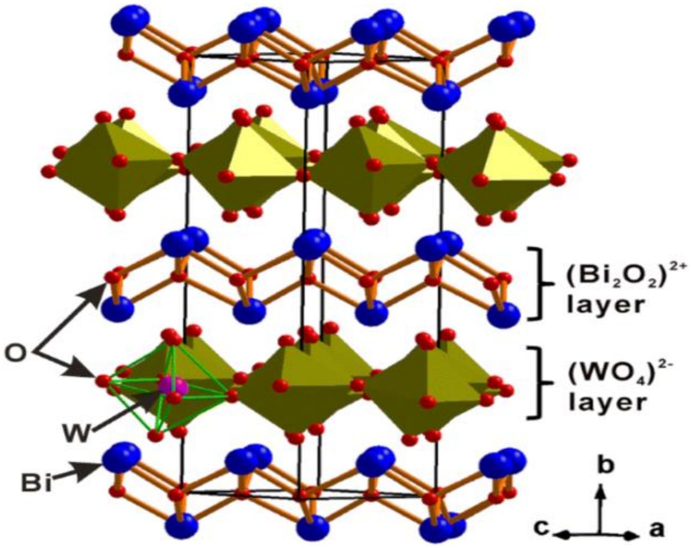

Figure 2-4: Schematic representation of the structure of Bi_2WO_6 [44].

2.9 Synthesis Techniques for Bi_2WO_6/BiOCl

When synthesizing a photocatalyst, it is important to consider the methods that have been previously used. This is because the synthesis route can greatly influence the size and morphology of the catalyst, impacting its overall performance. Several fabrication methods have been deployed to synthesize Bi_2WO_6/BiOCl. Each of these methods, as well as their synthesis conditions (Bi_2WO_6:BiOCl ratio, calcination temperature, and calcination time), influence the structure and therefore the properties of the catalyst. As such, it is important to fine-tune the conditions of the selected route to optimize catalyst performance. It is generally the case that Bi_2WO_6/BiOCl composite heterojunctions are synthesized via hydrothermal calcination. Nonetheless, it is important to pay due diligence to all of the reported fabrication methods to gain a better understanding of the behaviour and applications of the photocatalyst. The following passage will explore the major synthesis routes used to synthesize Bi_2WO_6/BiOCl heterojunctions.

2.9.1: Solvothermal Synthesis

Solvothermal synthesis is a common technique used for the fabrication of many photocatalysts due to the control of particle size and morphology. Several studies have reported the use of this method for the synthesis of Bi_2WO_6/BiOCl. A typical process adapted from Xu et al. involved a two-stage solvothermal synthesis of the heterojunction [59]. Firstly, a designated amount of bismuth (III) nitrate pentahydrate ($Bi(NO_3)_3{\cdot}5H_2O$) is dispersed into ethylene glycol (EG). Next, sodium chloride (NaCl), serving as the chlorine source, is added to deionized water under constant magnetic stirring. This is followed by the dropwise addition of the deionized aqueous solution to the EG solution under stirring. After sufficient mixing is achieved, the combined solution is transferred into a Teflon-lined autoclave and subsequently heated at 120°C for a period of 12 hours. Once the BiOCl sample is cooled and collected, it is stored for later use. Next, the Bi_2WO_6/BiOCl composites were fabricated. This part of the process involves the addition of $Bi(NO_3)_3{\cdot}5H_2O$ and

$Na_2WO_4{\cdot}2H_2O$ into EG under constant magnetic stirring. Once a uniform suspension is attained, a selected amount of the previously synthesized BiOCl is mixed into the EG solution. The combined mixture is then placed in a Teflon-lined autoclave for a period of 12 hours at 180°C to form Bi_2WO_6/BiOCl composites. Using this method, Xu et al. reported a 97.4% reduction of 10 ppm RhB within 60 minutes of visible light irradiation, representing a 1.4 and 4-fold improvement in photocatalytic activity compared to Bi_2WO_6 and BiOCl synthesized under similar conditions [59]. Several other studies have also reported the effective treatment of organic pollutants by Bi_2WO_6/BiOCl structures synthesized with similar solvothermal methods [60], [61], [62], [63].

2.9.2: Ionic-liquid Assisted Ultrasonication

Recently, ultrasonic synthesis has received attention for its ability to use mild reaction conditions to produce catalysts of high purity. This process relies on acoustic cavitation, which involves the growth and subsequent collapse of bubbles in ionic liquids, providing localized heating that facilitates catalyst-producing reactions [64]. As such, the use of ionic liquids has shown good compatibility for the fabrication of a wide array of inorganic semiconductors, including several photocatalysts. This method has recently been explored for the fabrication of Bi_2WO_6/BiOCl heterojunctions. One such case was presented by Zhu et al., who developed an ionic-liquid assistance ultrasonic technique to produce the composite at room temperature [65]. Typically, an ionic liquid consisting of 1-butyl-3-methylimidazolium chloride ([BMIM]Cl) acts as the chlorine source. The heterojunction is formed by first adding ([BMIM]Cl) to a deionized water solution containing ($Bi(NO_3)_3{\cdot}5H_2O$) and $Na_2WO_4{\cdot}2H_2O$. After sufficient magnetic stirring is achieved, the mixture is placed in an ultrasonic bath for 2 hours. The resulting products are collected, cleaned, and dried for further analysis. This method has been reported to yield pure samples of composites consisting of orthorhombic Bi_2WO_6 and tetragonal structured BiOCl, imparting impressive photocatalytic properties. It was reported that the heterojunction facilitated the near-complete degradation of 5 ppm RhB within 100 min under visible light conditions, showcasing the potential for this fabrication route [65].

2.9.3: Hydrothermal Synthesis

Recently, hydrothermal synthesis methods have become very popular in many material sciences, including photocatalysis. This is because they allow for greater control of particle size and morphology while requiring relatively low temperatures of calcination. This is also the case for Bi_2WO_6/BiOCl composites, as the most common means of fabrication of this catalyst in the literature has been reported to be via the hydrothermal route [55], [59], [66]. In a typical process, a certain amount of $Bi(NO_3)_3·5H_2O$ and $Na_2WO_4·2H_2O$ is transferred into distilled water to obtain a well-mixed dispersion. Simultaneously, a quantity of NaCl, serving as the Cl source for BiOCl, is dissolved into DDW to obtain a solution. The NaCl solution is subsequently transferred into the first dispersion in a dropwise manner. The combined solution is transferred into an autoclave and heated in a mechanical heater. It has been reported that the temperature and time of calcination in the autoclave play important roles in the activity of the resultant catalyst. Liang et al. reported that calcination for 12 hours at 160°C can lead to near-complete degradation of RhB within a period of 160 minutes of illumination [67]. Additionally, it has been reported that synthesising this catalyst at 160°C for 8 hours can also lead to considerable photocatalytic performance [68].

2.10 Plasmonic Metal Enhanced Photocatalysis

As demonstrated in the previous section, the synthesis techniques that are used to fabricate Bi_2WO_6/BiOCl heterojunctions are generally well established. However, limited work has been reported on the use of noble metal deposition to improve the visible-light activity of this catalyst. The following section will discuss noble metal-induced surface plasmon resonance and how it has emerged as a promising tool used to improve the performance of many catalysts.

As mentioned, one of the main challenges that limits photocatalysis is low visible light responsiveness and high e^-/h^+ recombination [25]. In addition to heterojunction formation, noble metal deposition has recently been studied to improve the visible-light-driven photoactivity of many catalysts. The addition of metal nanoparticles to catalyst structures has two main merits, namely, suppression of charge carrier recombination and increased visible light responsiveness via the surface plasmon resonance (SPR) effect [69].

2.10.1: Surface Plasmon Resonance Effect

As detailed in the previous passage, one of the main benefits of depositing metal nanoparticles on catalysts is the SPR effect. This phenomenon occurs as a result of the combined oscillation of the electrons in the CB at the metal-dielectric layer [70]. It is a generally accepted concept that there are two major modes through which surface plasmon resonance occurs. These include propagating and localized surface plasmon resonance, PSPR, and LSPR, respectively [70], [71]. When metal nanoparticles are added to photocatalysts, they can cause the formation of localized surface plasmons, which leads to the LSPR effect. Typically, when plasmonic metal nanoparticles are introduced to semiconductor catalysts, the SPR effect occurs due to their interactions with incident photons. This is because when incident photons excite electrons located on the nanoparticles, there is an oscillation of the electron density that propagates in the nanoparticles, creating surface plasmons, as shown in Figure 2-5 [72]. Since many noble metals, including Ag, Au, Pt, and Pd, are typically smaller dimensionally relative to the wavelength of the incident photons, the incoming light will cause the nanoparticle electron cloud to resonant with the frequency of the absorbed light. This is significant as it creates localized electromagnetic fields on the surface of the nanoparticles [70], [71], [72]. The resultant electromagnetic field may further intensify if it comes into contact with the fields of neighbouring NPs. This phenomenon is known as the near-field dipolar coupling effect, which increases the visible light absorption by the metal particles.

This effect broadens the absorption spectra of the nanoparticles and, as a result, causes increased visible light responsiveness. This property allows surface plasmon resonance to be an attractive tool to enhance the visible light activity of photocatalysts.

In addition to the SPR effect, plasmonic metals possess excellent conductive properties. For instance, these metals typically have an electric conductance of 10^7-10^8 S/m in their bulk form [73]. However, these values are mostly retained even on the nanoparticle scale. This allows for them to be great materials in the transport of e^- and h^+ and allows them to act as charge traps, which greatly diminishes the charge carrier recombination rate [72]. This is useful in addressing the high recombination rate often incurred by photocatalysts. Plasmonic NPs have recently been used in a variety of applications, including cancer therapy, sensing devices, photodetectors, and photocatalysis [70], [74]. The following section will discuss how these plasmonic materials are being used to bolster visible-light-driven photocatalysis.

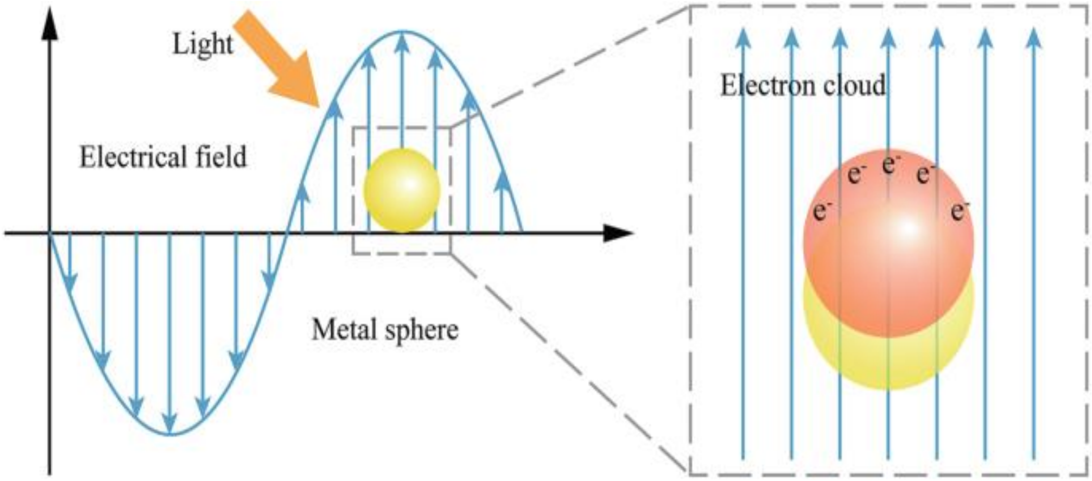

Figure 2-5: Schematic description of how incident light on metal NPs leads to oscillation of CB electrons, causing the LSPR effect [72].

2.10.2: Properties of Plasmonic Photocatalysts

When plasmonic heavy metals are added to catalysts, they do not significantly alter the photocatalytic mechanism described in Section 2.4 [70]. It is important to mention, however, that the plasmonic metals add several beneficial properties to the catalyst, which enhance their overall performance. The first difference arises from the formation of Schottky junctions, which are formed when there is a direct contact between a semiconductor and a metal [75]. It can be described as the charge layer region resulting from the overall energy difference between the CB of the semiconductor and the Fermi level of the plasmonic metal [75]. The energy of the free electrons located in the space-charge region increases as they approach the interface of the metal and semiconductor. This creates internal electric fields directed from the metal to n-type semiconductors and in the opposite direction for p-type semiconductors [75].

One of the main challenges faced in semiconductor photocatalysis is the high rate of recombination between excited e^- and h^+. The formation of a Schottky barrier can prove to be quite beneficial in addressing this issue. This is because when electrons from the photocatalyst are excited near or in the space-charge layer, the resultant electric fields impart a force on the electrons, essentially pushing them in the same direction of the field [75]. Simultaneously, the holes are pushed in the opposite direction of the electric field. This greatly limits the recombination of e^- and h^+ due to the force exerted by the internal electric fields.

Another major advantage of plasmonic photocatalysts is their increased absorption capacity. This arises from the electromagnetic fields located on the surface plasmons. When plasmonic metals are excited by visible light photons, they tend to generate surface plasmons that significantly narrow the band gap of the catalyst [70]. This enhances the visible light responsiveness of the entire catalyst, increasing the rate of photoactivity. Furthermore, the presence of metal NPs on the catalyst can introduce the photothermal effect. This phenomenon relates to an increase in thermal energy upon photoexcitation of the material, leading to increased kinetic energy and consequently an increase in the rate of reaction [70], [72].

In addition to reduced charge carrier recombination, surface plasmons can generate the dielectric polarization effect [70]. Such an event occurs when surface plasmons polarize the reactants located on the boundary between the metal and fluid. This increases the rate of adsorption of the organic pollutants onto the surface of the catalyst. However, it is important to note that if there are too many NPs deposited on the surface of the photocatalyst, they can limit the number of active sites, thereby limiting the adsorption of pollutant molecules [70]. Additionally, since the metal NPs display excellent conductive properties, they are able to efficiently transport e^- and h^+ from the semiconductor region to the metal-fluid interlayer, acting as charge traps. This allows for redox reactions to occur on the surface of the plasmonic metals [71]. This complements the redox reactions taking place on the surface of the catalyst, resulting in increased contact between the charge carrier species and pollutant molecules [75].

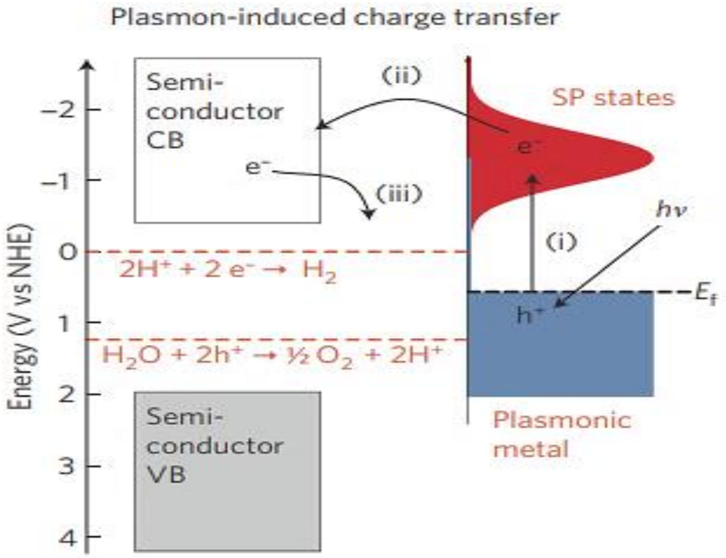

Figure 2-6: Schematic depiction of surface plasmon resonance induced charge transfer relative to NHE scale [76].

2.10.3: Heavy Metals for Plasmonic Photocatalysis

It has been reported that several metals, particularly heavy metals, have been used for plasmon-enhanced photocatalysis. Owing to their excellent conductive properties, Au and Ag have been the most commonly used heavy metals [70]. Both of these metals are categorized as group 11 metals on the periodic table and, as a result, contain a single S-orbital e^- located in their outer shells [76]. As such, these metals tend to favour losing their e^-, gaining a positive charge in the form of Ag^- and Au^+ [76]. Contrastingly, Pt and Pd both belong to group 10 and tend to lose $2e^-$ to form Pt^{2+} and Pd^{2+}, respectively [77]. An important parameter to consider when selecting a suitable metal is the work function, which represents how well it is able to retain its electrons. Comparing the work functions of the four metals follows: $\phi_{Au} > \phi_{Pt} > \phi_{Pd} > \phi_{Ag}$ [70]. As such, silver and palladium have the lowest work functions and tend to lose their electrons more easily. This is significant as semiconductors tend to form Schottky barriers more suitably with metals with lower work functions [75].

Another factor to consider when selecting a suitable metal is its conductivity. Among the four heavy metals discussed, Ag and Au have the highest thermal conductivities of 314 and 428 W/mK, respectively [78]. Since Ag has a suitable work function and a high conductivity value, it is a popular choice to enhance the performance of photocatalysts. In fact, a paper published by Wang et al. recently explored Ag-Bi_2WO_6/BiOCl in the degradation of the organic pollutant mercaptobenzothiazole [79]. However, palladium should also be considered for Bi_2WO_6/BiOCl due to its high stability, high intrinsic photocatalytic activity, and its tendency to induce the surface plasmon resonance effect to enhance visible light activity [80]. In this work, Pd was deposited on the surface of Bi_2WO_6/BiOCl to study its viability for the degradation of organic pollutants.

2.11 Parameters of Synthesis

As mentioned in the previous section, Pd-Bi_2WO_6/BiOCl will be studied for its application in the degradation of organic pollutants. However, in order to test the strength of a catalyst, its synthesis parameters must first be optimised, to yield the most effective results. The following passage will outline several key synthesis parameters that should be considered in the design of the novel Pd-Bi_2WO_6/BiOCl heterojunction.

2.11.1 Ratio between Bi_2WO_6/BiOCl

When designing an effective heterojunction catalyst, it is often the case that the ratio between the two parent compounds is optimized. The ratio of Bi_2WO_6:BiOCl plays a critical role in how the catalyst behaves. This is because Bi_2WO_6 displays good visible light responsiveness, whereas BiOCl generally imparts effective e^-/h^+ separation. As such, it is important to find a ratio that maximizes the benefits of both catalysts. During the hydrothermal synthesis of Bi_2WO_6/BiOCl, the ratio is often controlled by varying the amount of the chlorine source (NaCl) while maintaining the same amount of $Bi(NO_3)_3 \cdot 5H_2O$ and $Na_2WO_4 \cdot 2H_2O$ [81], [82]. This allows for a simple yet effective fine-tuning of the amount of BiOCl in the composite. Typically, most of the heterojunction comprises Bi_2WO_6 while maintaining a small amount of BiOCl to boost charge carrier separation. It has been reported that if there is an excess amount of BiOCl, the activity tends to decrease. This is because at elevated levels, BiOCl can increase the E_g of the composite, rendering it less effective under visible-light illumination. Several papers have studied the effect of the composition ratio on the overall performance of the catalyst, including Yang et al., who achieved near-complete degradation of gaseous toluene with Bi_2WO_6/BiOCl at a $Cl^-:WO_4^{2-}$ ratio of 1:3 [81]. Another study conducted by Guo et al. investigated the performance of Bi_2WO_6/BiOCl with a composition of 1% Bi_2WO_6 on the degradation of phenol and oxytetracycline [82]. This is important as it shows the ratio between the parent compounds can be expressed in a variety of ways and that the optimal ratio varies based on the specific application of the catalyst.

2.11.2 Temperature of Calcination

In addition to the composition of the heterojunction, the thermal conditions of the hydrothermal synthesis will also significantly impact the properties of the catalyst. Moreover, it is important to optimise these conditions in order to minimise the time and temperature of calcination to lessen the capital cost of the project. The temperature and time of calcination often play interchangeable roles; however, it is common practice to optimise the temperature first to minimise the amount of heat expenditure required for the synthesis [83]. The temperature at which the catalyst is sintered can determine its morphology and size. This effects how the catalyst particles interact with the organic pollutants and hence their adsorption properties. Typically, at higher temperatures Bi_2WO_6/BiOCl displays a more flake-like presentation. Yao et. al found that when the temperature increases from 120 to 180°C, the average particle size of Bi_2WO_6 increases [83]. It was reported that at lower particle sizes, the total surface area of the catalyst will be greater allowing for better absorption of reactants. As such, the study found that at a calcination temperature of 120°C for several hours, the catalyst displayed the most effective degradation of RhB. Generally, it is the case that Bi_2WO_6/BiOCl composites are calcined between the temperatures of 120 to 180°C [79], [81], [82]. It is important to note that at lower temperatures the time of calcination required increases as to allow for sufficient pore formation on the catalytic surface.

2.11.3 Time of Calcination

The period of thermal treatment also affects the photoactivity, as it can often play a determinative role in the structure of the catalyst. As is the case with elevated temperatures, longer durations of thermal treatment can result in increased particle size, influencing how the catalyst interacts with reactant pollutants. Moreover, it can also affect the number of pores present on the catalytic surface, affecting the reactant uptake onto the active sites. Typically, longer calcination times are required for lower temperatures, and shorter times are required for higher temperatures. Several studies have aimed to establish the relationship between the calcination of Bi_2WO_6/BiOCl and its degradation activity against organic pollutants. Typically, calcination times for temperatures ranging from 120 to 180°C last from 6 to 15 hours, depending on the specific application of Bi_2WO_6/BiOCl [79], [81], [82], [83].

2.11.4 Amount of Palladium Loading

As discussed, the addition of noble metals to heterojunction photocatalysts helps to improve activity by increasing visible-light responsiveness and reducing electron-hole recombination. As such, it is important to determine the relationship between different amounts of palladium added to the catalyst and its performance. Moreover, when considering the economic feasibility of the design, it is preferable to limit the amount of Pd used to achieve optimal results. This is because Pd can be expensive, with a bulk price of $43.93 per gram [78]. As such, it is important to achieve high photoactivity while also limiting the amount of noble metal used. When adding plasmonic materials to catalyst structures, it is often the case that it results in a significant increase in visible light activity [78], [80], [84]. However, as greater amounts are added, the activity tends to plateau and eventually decline. This is because excess amounts of nanoparticles on the surface of the catalyst can occupy active sites, which are needed to adsorb reactants [84]. Elevated Pd levels can also cause a shielding effect, which causes photonic scattering, leading to less light absorption by the catalyst. Therefore, it is important to determine the optimum loading amount of Pd to maximize photocatalytic activity. So far, there has been limited work reported on the use of noble metals on Bi_2WO_6/BiOCl structures. However, a paper published by Wang et al. did explore the use of Ag-Bi_2WO_6/BiOCl composites for the degradation of MBT, showing significantly greater visible-light activity than Bi_2WO_6/BiOCl structures [79].

2.12 Applications for Bi_2WO_6/BiOCl and Pd-Bi_2WO_6/BiOCl

Bi_2WO_6/BiOCl has been reported to be used in a variety of environmental applications, ranging from bacterial disinfection to UV shielding applications. However, the vast majority of work conducted on this catalyst has focused on its effectiveness in the degradation of organic pollutants in aqueous systems. This section will discuss the use of Bi_2WO_6/BiOCl and Pd-Bi_2WO_6/BiOCl for industrial organic dyes in water treatment applications.

2.12.1 Mercaptobenzothiazole

Consisting of the chemical formula $C_6H_4(NH)SC=S$, 2-mercaptobenzothiozole is an organosulfur compound commonly used for processing rubbers [85]. Namely, it is used for the sulfur vulcanization process, in which rubbers are converted into harder materials through the creation of sulfur cross linkages between polymer chains. MBT is most frequently synthesized at high temperature reactions between carbon disulfide and aniline in the presence of sulfur. It is also produced via a reaction between 2-aminothiophenol and carbon disulfide [85]. MBT has long been used as a target pollutant in aqueous photocatalytic systems when assessing the performance of catalysts. Wang et. al a studied the effect of Bi_2WO_6/BiOCl and a novel Ag-Bi_2WO_6/BiOCl in the degradation of this compound [79]. It was reported that when using Bi_2WO_6/BiOCl and Ag-Bi_2WO_6/BiOCl under visible light illumination, that MBT was degrade to an extent of 80% and 93% respectively [79].

2.12.2 Phenol

Phenol is an organic aromatic compound consisting of the chemical formula C_6H_5OH. It is described as being a white crystalline powder that is volatile and gives off a sweet odour [86]. The main use for phenol relates to its application in synthesizing plastics, herbicides, and several pharmaceutical drugs [86]. Phenol is most commonly produced by the cumene process, which involves the partial oxidation of isopropylbenzene (cumene). Phenol is also used as a model target organic pollutant in aqueous photocatalytic testing. This is because phenol, along with its various intermediates, is often discharged into effluent wastewater sources, posing a threat to the environment. Moreover, many chemical, biological, and photolytic degradation processes are often ineffective in breaking down this compound [86], [87]. As such, photocatalysis provides a means to degrade this harmful pollutant. However, due to its many intermediates and complicated degradation routes, phenol can often take long periods of time to degrade and is not considered an ideal compound to use for degradation testing for Bi_2WO_6/BiOCl-based compounds. This is because a high number of intermediates can often interfere with spectrophotometric measurements, rendering it impractical to judge the strength of the catalyst. However, there has been work performed on this pollutant using Bi_2WO_6/BiOCl. Guo et al. achieved 93% degradation of 20 ppm phenol within 5 hours of visible light illumination using a 1% mixture of Bi_2WO_6/BiOCl [82].

2.12.3 Methylene Blue

Characterized by its distinct blue colour, methylthioninium chloride ($C_{16}H_{18}ClN_3S$), more commonly known as methylene blue, is an organic compound frequently used as a dye and for medicinal purposes [88]. This compound is prepared through the oxidation of 4-aminodimethylaniline in the presence of sodium thiosulfate. Methylene blue is often used for the treatment of methemoglobinemia which causes elevated levels of methemoglobin, a metalloprotein form of hemoglobin [88]. Traditionally, methylene blue was used as a synthetic dye in the clothing and textile industries. For many years, methylene blue has been detected at elevated levels to be present in groundwater and surface water sources, posing a treat to the environment. Among classic techniques of treatment, including many non-photochemical methods, photocatalysis has been explored for the degradation of this compound. Several studies have examined the use of Bi_2WO_6/BiOCl for the degradation of this dye. Once such case can be found with Jiang et al. who constructed hydrangea shaped Bi_2WO_6/BiOCl composites which were able to remove 88% of 10 ppm MB within a period of 75 minutes of visible light illumination [89]. Another study conducted by Chen et al. studied the effect of the composition ratio and was able achieve 90% degradation of 10 ppm MB within a period of 60 minutes [90]. These studies show that Bi_2WO_6/BiOCl exhibits effective degradation efficiencies and times for the removal of methylene blue dye.

2.12.4 Rhodamine B

One of the most frequently used dyes used for testing the activity of catalysts is rhodamine B. Belonging to the xanthene class of dyes, RhB has the chemical formula $C_{28}H_{31}ClN_2O_3$ and can be seen in Figure 2-7 [91], [92]. Applications for this compound range from being used in paints and paper to the textile industry. Despite its many uses, RhB is also one of the most toxic dyes and poses considerable risk to the ecosystem [93]. They have been found to have neurotoxic and carcinogenic properties, posing adverse effects on the development of living organisms [91]. Moreover, due to its widespread industrial use, this dye has also been found in many wastewater sources, posing a risk to the environment. Due to their stable properties, RhB molecules tend to withstand natural degradation, making them difficult to remove from water sources. As such, it has long been studied as a target pollutant for many visible-light catalysts, including Bi_2WO_6/BiOCl. Its relatively simple degradation route makes it a popular choice when testing the strength of catalysts. As a result, it has become one of the most commonly used target pollutants for assessing the photocatalytic properties of Bi_2WO_6/BiOCl.

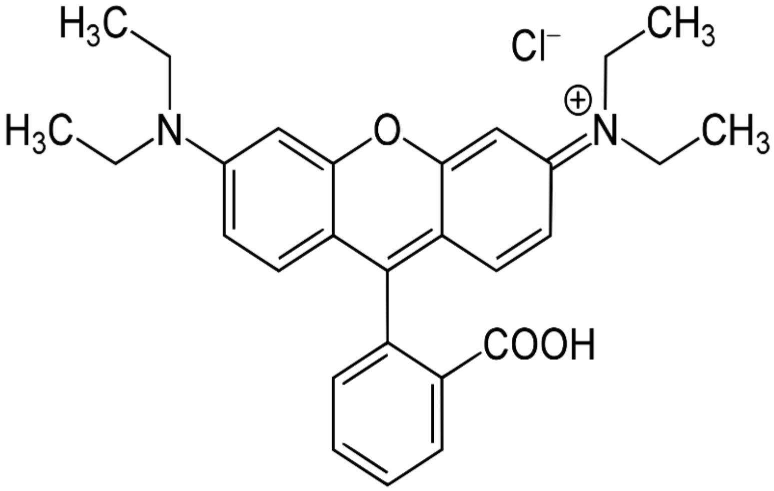

Figure 2-7: Schematic diagram of the structure of Rhodamine B [92].

2.13 Conclusion

This review provides an in-depth survey of aqueous photocatalytic systems for the degradation of organic pollutants. Traditional decontamination techniques have often involved ion exchange, membrane filtration, adsorption, and precipitation to achieve certain levels of degradation. However, these processes are often limited by incomplete treatment, harmful by-products, and high costs of operation. In recent times, heterogeneous photocatalysis has been regarded as an effective option for water treatment. Owing to the generation of highly oxidative species (h^+, •OH, and $O_2^{\bullet}$), photocatalysts are able to effectively target and degrade organic pollutants under illumination. Traditionally, TiO_2 has been viewed as a close-to-ideal catalyst due to its high chemical stability, non-toxicity, low manufacturing cost, and high photoactivity. However, as a result of its wide band gap, TiO_2 can only be activated under UV radiation, limiting its application. In order to address these challenges, modern work in this field aims to develop photoactive materials with high activity and low band gaps to gain better access to the visible-light spectrum.

Recently, Bi_2WO_6/BiOCl has been considered a potential candidate to provide effective treatment of a variety of organic pollutants. Formed as a heterojunction, Bi_2WO_6/BiOCl is able to incorporate the visible light responsiveness of Bi_2WO_6 and the low e^-/h^+ recombination rate of BiOCl. As such, this catalyst has proven to be effective in the decontamination of a variety of organic pollutants in water. Nonetheless, work still remains to be done on determining ideal synthesis conditions, including composition ratio, calcination temperature, and calcination time. Further research should also explore the potential for noble-metal deposition on this catalyst to study the effects of surface plasmon resonance in boosting its visible-light activity. Overall, Bi_2WO_6/BiOCl presents excellent photocatalytic properties and deserves further exploration for organic pollutant degradation.

2.14 Nomenclature

A	Absorbance
pKa	Acid dissociation constant at logarithmic scale
F	Actual quantum yield
k_r	Actual rate constant
K	Adsorption equilibrium constant
F'	Apparent quantum yield
k_{app}	Apparent degradation rate constant
E_g	Band gap energy
$Bi(NO_3)_3 \cdot 5H_2O$	Bismuth (III) nitrate pentahydrate
BiOCl	Bismuth oxychloride
BiOX	Bismuth oxyhalide
Bi_2WO_6	Bismuth tungstate
CO_2	Carbon dioxide
c_t	Concentration at specific time
c	Concentration of substrate
E_{CB}	Conduction band edge
E	Degradation efficiency
e^-	Electron
E^e	Free electron energy
h^+	Hole
H_2O_2	Hydrogen peroxide
H^+	Hydronium ion

OH^-	Hydroxide anion
$\bullet OH$	Hydroxyl radical
c_0	Initial concentration
a	Molar absorptivity
N_R	Number of reacted electrons
O_2	Oxygen
l	Path length of irradiation
N_A	Photon absorbance from the light source
h	Planck’s constant
k_{CT}	Rate of charge transfer
k_R	Rate of electron-hole recombination
NaCl	Sodium chloride
$Na_2WO_4 \cdot 2H_2O$	Sodium tungstate dihydrate
$O_2^{\bullet -}$	Superoxide radical
t	Time
TiO_2	Titanium dioxide
E_{VB}	Valence band edge
H_2O	Water
ZnO	Zinc Oxide

2.15 Greek Letters

λ	Absorbance-edge wavelength
v	Frequency of light
χ_p	Semiconductor electronegativity

2.16 Abbreviations

AOP	Advanced Oxidation Process
CB	Conduction Band
EG	Ethylene Glycol
L-H	Langmuir-Hinshelwood
LSPR	Localized Surface Plasmon Resonance
MBT	Mercaptobenzothiazole
MB	Methylene Blue
NP	Nanoparticle
NHE	Normal Hydrogen Electrode
PSPR	Propagating Surface Plasmon Resonance
RhB	Rhodamine B
SPR	Surface Plasmon Resonance
UV	Ultraviolet
VB	Valence Band

References

[1] M. A. Al-Nuaim, A. A. Alwasiti, and Z. Y. Shnain, “The photocatalytic process in the treatment of polluted water,” *Chemical Papers 2022 77:2*, vol. 77, no. 2, pp. 677–701, Oct. 2022, doi: 10.1007/S11696-022-02468-7.

[2] E. Koncagül and R. Connor, “The United Nations World Water Development Report 2023: partnerships and cooperation for water; facts, figures and action examples,” Paris, 2023.

[3] S. Mishra and B. Sundaram, “A review of the photocatalysis process used for wastewater treatment,” *Mater Today Proc*, Jul. 2023, doi: 10.1016/J.MATPR.2023.07.147.

[4] G. Crini and E. Lichtfouse, “Advantages and disadvantages of techniques used for wastewater treatment,” *Environ Chem Lett*, vol. 17, no. 1, pp. 145–155, Mar. 2019, doi: 10.1007/s10311-018-0785-9.

[5] A. O. Oluwole, E. O. Omotola, and O. S. Olatunji, “Pharmaceuticals and personal care products in water and wastewater: a review of treatment processes and use of photocatalyst immobilized on functionalized carbon in AOP degradation,” *BMC Chem*, vol. 14, no. 1, p. 62, Dec. 2020, doi: 10.1186/s13065-020-00714-1.

[6] G. Ren *et al.*, “Recent Advances of Photocatalytic Application in Water Treatment: A Review,” *Nanomaterials 2021, Vol. 11, Page 1804*, vol. 11, no. 7, p. 1804, Jul. 2021, doi: 10.3390/NANO11071804.

[7] S. K. Loeb *et al.*, “The Technology Horizon for Photocatalytic Water Treatment: Sunrise or Sunset?,” *Environ Sci Technol*, vol. 53, no. 6, pp. 2937–2947, Mar. 2019, doi: 10.1021/ACS.EST.8B05041.

[8] M. M. Ayyub and C. N. R. Rao, “Design of efficient photocatalysts through band gap engineering,” in *Nanostructured Photocatalysts*, Elsevier, 2020, pp. 1–18. doi: 10.1016/B978-0-12-817836-2.00001-6.

[9] S. Mishra and B. Sundaram, “A review of the photocatalysis process used for wastewater treatment,” *Mater Today Proc*, Jul. 2023, doi: 10.1016/j.matpr.2023.07.147.

[10] S. Y. Lee and S. J. Park, “TiO2 photocatalyst for water treatment applications,” *Journal of Industrial and Engineering Chemistry*, vol. 19, no. 6, pp. 1761–1769, Nov. 2013, doi: 10.1016/J.JIEC.2013.07.012.

[11] L. Wang and J. Yu, “Principles of photocatalysis,” 2023, pp. 1–52. doi: 10.1016/B978-0-443-18786-5.00002-0.

[12] D. O. Charkin, D. N. Lebedev, and S. M. Kazakov, “Multiple cation and anion substitutions into the structures of Bi2WO6 and PbBi3WO8Cl,” *J Alloys Compd*, vol. 536, pp. 155–160, Sep. 2012, doi: 10.1016/J.JALLCOM.2012.04.113.

[13] Z. Zhu *et al.*, “Recent progress in Bi_2WO_6 -Based photocatalysts for clean energy and environmental remediation: Competitiveness, challenges, and future perspectives,” *Nano Select*, vol. 2, no. 2, pp. 187–215, Feb. 2021, doi: 10.1002/nano.202000127.

[14] Z. Li, L. Zhu, W. Wu, S. Wang, and L. Qiang, “Highly efficient photocatalysis toward tetracycline under simulated solar-light by Ag+-CDs-Bi2WO6: Synergistic effects of silver ions and carbon dots,” *Appl Catal B*, vol. 192, pp. 277–285, Sep. 2016, doi: 10.1016/j.apcatb.2016.03.045.

[15] X. Yu, J. Yang, K. Ye, X. Fu, Y. Zhu, and Y. Zhang, “Facile one-step synthesis of BiOCl/BiOI heterojunctions with exposed {001} facet for highly enhanced visible light photocatalytic performances,” *Inorg Chem Commun*, vol. 71, pp. 45–49, Sep. 2016, doi: 10.1016/J.INOCHE.2016.06.034.

[16] Z. Liang, C. Zhou, J. Yang, Q. Mo, Y. Zhang, and Y. Tang, “Visible light responsive Bi 2 WO 6 /BiOCl heterojunction with enhanced photocatalytic activity for degradation of tetracycline and rohdamine B,” *Inorg Chem Commun*, vol. 93, pp. 136–139, Jul. 2018, doi: 10.1016/j.inoche.2018.05.022.

[17] G. Zhang, Y. Tan, Z. Sun, and S. Zheng, “Synthesis of BiOCl/TiO 2 heterostructure composites and their enhanced photocatalytic activity,” *J Environ Chem Eng*, vol. 5, no. 1, pp. 1196–1204, Feb. 2017, doi: 10.1016/j.jece.2017.01.040.

[18] Q. Su *et al.*, “Construction of a Bioinspired Hierarchical $BiVO_4$ /BiOCl Heterojunction and Its Enhanced Photocatalytic Activity for Phenol Degradation,” *ACS Appl Mater Interfaces*, vol. 13, no. 28, pp. 32906–32915, Jul. 2021, doi: 10.1021/acsami.1c05117.

[19] X. Zhang, G. Xu, J. Hu, J. Lv, J. Wang, and Y. Wu, “Fabrication and photocatalytic performances of BiOCl nanosheets modified with ultrafine Bi_2O_3 nanocrystals,” *RSC Adv*, vol. 6, no. 68, pp. 63241–63249, 2016, doi: 10.1039/C6RA09919J.

[20] N. Tahmasebi, Z. Maleki, and P. Farahnak, “Enhanced photocatalytic activities of Bi2WO6/BiOCl composite synthesized by one-step hydrothermal method with the assistance of HCl,” *Mater Sci Semicond Process*, vol. 89, pp. 32–40, Jan. 2019, doi: 10.1016/j.mssp.2018.08.026.

[21] Y. Huang *et al.*, “Peroxymonosulfate Activation by Bi2WO6/BiOCl Heterojunction Nanocomposites under Visible Light for Bisphenol A Degradation,” *Nanomaterials*, vol. 11, no. 11, p. 3130, Nov. 2021, doi: 10.3390/nano11113130.

[22] M. Guo *et al.*, “Bi2WO6–BiOCl heterostructure with enhanced photocatalytic activity for efficient degradation of oxytetracycline,” *Sci Rep*, vol. 10, no. 1, p. 18401, Oct. 2020, doi: 10.1038/s41598-020-75003-x.

[23] L. Derikvand and N. Tahmasebi, “Synthesis and photocatalytic performance of Bi2WO6/BiOX (X=Cl, Br, I) composites for RhB degradation under visible light,” *Korean Journal of Chemical Engineering*, vol. 38, no. 1, pp. 163–169, Jan. 2021, doi: 10.1007/s11814-020-0687-y.

[24] J. Chen *et al.*, “Preparation of BiOCl/Bi2WO6 Photocatalyst for Efficient Fixation on Cotton Fabric: Applications in UV Shielding and Self-Cleaning Performances,” *Materials*, vol. 14, no. 22, p. 7002, Nov. 2021, doi: 10.3390/ma14227002.

[25] A. Nazir, P. Huo, H. Wang, Z. Weiqiang, and Y. Wan, “A review on plasmonic-based heterojunction photocatalysts for degradation of organic pollutants in wastewater,” *J Mater Sci*, vol. 58, no. 15, pp. 6474–6515, Apr. 2023, doi: 10.1007/s10853-023-08391-w.

[26] Z. Li and X. Meng, “Recent development on palladium enhanced photocatalytic activity: A review,” *J Alloys Compd*, vol. 830, p. 154669, Jul. 2020, doi: 10.1016/j.jallcom.2020.154669.

[27] M. Arumugam, R. Koutavarapu, K.-K. Seralathan, S. Praserthdam, and P. Praserthdam, “Noble metals (Pd, Ag, Pt, and Au) doped bismuth oxybromide photocatalysts for improved visible light-driven catalytic activity for the degradation of phenol,” *Chemosphere*, vol. 324, p. 138368, May 2023, doi: 10.1016/j.chemosphere.2023.138368.

[28] Z. Li and X. Meng, “Recent development on palladium enhanced photocatalytic activity: A review,” *J Alloys Compd*, vol. 830, p. 154669, Jul. 2020, doi: 10.1016/j.jallcom.2020.154669.

[29] R. Wang, B. Li, Y. Xiao, X. Tao, X. Su, and X. Dong, “Optimizing Pd and Au-Pd decorated Bi2WO6 ultrathin nanosheets for photocatalytic selective oxidation of aromatic alcohols,” *J Catal*, vol. 364, pp. 154–165, 2018, doi: 10.1016/j.jcat.2018.05.015.

[30] S. Y. Lee and S. J. Park, “TiO2 photocatalyst for water treatment applications,” *Journal of Industrial and Engineering Chemistry*, vol. 19, no. 6, pp. 1761–1769, Nov. 2013, doi: 10.1016/J.JIEC.2013.07.012.

[31] Alexander Eibner, “Action of Light on Pigments I,” *Chem-ZTG*, pp. 753–755, 1911.

[32] C. F. Goodeve and J. A. Kitchener, “The mechanism of photosensitisation by solids,” *Transactions of the Faraday Society*, vol. 34, p. 902, 1938, doi: 10.1039/tf9383400902.

[33] V.N. Filimonov, “Photocatalytic Oxidation of Gaseous Isopropanol on ZnO + TiO 2,” *Dokl Akad Nauk SSSR*, vol. 154, no. 4, pp. 922–925, 1964.

[34] A. FUJISHIMA and K. HONDA, “Electrochemical Photolysis of Water at a Semiconductor Electrode,” *Nature*, vol. 238, no. 5358, pp. 37–38, Jul. 1972, doi: 10.1038/238037a0.

[35] S. Zhu and D. Wang, “Photocatalysis: Basic Principles, Diverse Forms of Implementations and Emerging Scientific Opportunities,” *Adv Energy Mater*, vol. 7, no. 23, Dec. 2017, doi: 10.1002/aenm.201700841.

[36] S. Mishra and B. Sundaram, “Efficacy of nanoparticles as photocatalyst in leachate treatment,” *Nanotechnology for Environmental Engineering*, vol. 7, no. 1, pp. 173–192, Mar. 2022, doi: 10.1007/s41204-021-00209-x.

[37] H. Wang *et al.*, “Semiconductor heterojunction photocatalysts: design, construction, and photocatalytic performances,” *Chem Soc Rev*, vol. 43, no. 15, p. 5234, Jul. 2014, doi: 10.1039/C4CS00126E.

[38] P. Doran, *Engineering Principles Second Edition*. 2013. Accessed: Nov. 19, 2022. [Online]. Available: http://www.sciencedirect.com:5070/book/9780122208515/bioprocess-engineering-principles

[39] S. A. Heredia Deba, B. A. Wols, D. R. Yntema, and R. G. H. Lammertink, “Photocatalytic ceramic membrane: Effect of the illumination intensity and distribution,” *J Photochem Photobiol A Chem*, vol. 437, p. 114469, Mar. 2023, doi: 10.1016/j.jphotochem.2022.114469.

[40] Suresh C. Ameta and Rakshit Ameta, *Advanced Oxidation Processes for Wastewater Treatment Emerging Green Chemical Technology*, 1st ed. Elsevier, 2018.

[41] T. G. Mayerhöfer, S. Pahlow, and J. Popp, “The Bouguer-Beer-Lambert Law: Shining Light on the Obscure.,” *Chemphyschem*, vol. 21, no. 18, pp. 2029–2046, Sep. 2020, doi: 10.1002/cphc.202000464.

[42] C. Belver, J. Bedia, M. Peñas-Garzón, V. Muelas-Ramos, A. Gómez-Avilés, and J. J. Rodriguez, “Structured photocatalysts for the removal of emerging contaminants under visible or solar light,” in *Visible Light Active Structured Photocatalysts for the Removal of Emerging Contaminants*, Elsevier, 2020, pp. 41–98. doi: 10.1016/B978-0-12-818334-2.00003-1.

[43] M. Bodzek and M. Rajca, “Photocatalysis in the treatment and disinfection of water. Part I. Theoretical backgrounds / Fotokataliza w oczyszczaniu i dezynfekcji wody część i. podstawy teoretyczne,” *Ecological Chemistry and Engineering S*, vol. 19, no. 4, pp. 489–512, Nov. 2012, doi: 10.2478/v10216-011-0036-5.

[44] Y. Liang and J. Shi, “Effect of Halide Ions on the Microstructure of Bi2WO6 with Enhanced Removal of Rhodamine B,” *J Inorg Organomet Polym Mater*, vol. 30, no. 8, pp. 2872–2880, Aug. 2020, doi: 10.1007/s10904-019-01437-0.

[45] P. O. Oladoye, T. O. Ajiboye, E. O. Omotola, and O. J. Oyewola, “Methylene blue dye: Toxicity and potential elimination technology from wastewater,” *Results in Engineering*, vol. 16, p. 100678, Dec. 2022, doi: 10.1016/j.rineng.2022.100678.

[46] B. Liu, X. Zhao, C. Terashima, A. Fujishima, and K. Nakata, “Thermodynamic and kinetic analysis of heterogeneous photocatalysis for semiconductor systems,” *Physical Chemistry Chemical Physics*, vol. 16, no. 19, p. 8751, 2014, doi: 10.1039/c3cp55317e.

[47] A. H. Navidpour, S. Abbasi, D. Li, A. Mojiri, and J. L. Zhou, “Investigation of Advanced Oxidation Process in the Presence of TiO2 Semiconductor as Photocatalyst: Property, Principle, Kinetic Analysis, and Photocatalytic Activity,” *Catalysts*, vol. 13, no. 2, p. 232, Jan. 2023, doi: 10.3390/catal13020232.

[48] A. Mohamed *et al.*, “Rapid photocatalytic degradation of phenol from water using composite nanofibers under UV,” *Environ Sci Eur*, vol. 32, no. 1, p. 160, Dec. 2020, doi: 10.1186/s12302-020-00436-0.

[49] J. Z. Bloh, “A Holistic Approach to Model the Kinetics of Photocatalytic Reactions,” *Front Chem*, vol. 7, Mar. 2019, doi: 10.3389/fchem.2019.00128.

[50] J. M. Doña *et al.*, “The effect of dosage on the photocatalytic degradation of organic pollutants,” *Research on Chemical Intermediates*, vol. 33, no. 3–5, pp. 351–358, Mar. 2007, doi: 10.1163/156856707779238676.

[51] L. Derikvand and N. Tahmasebi, “Synthesis and photocatalytic performance of Bi2WO6/BiOX (X=Cl, Br, I) composites for RhB degradation under visible light,” *Korean J Chem Eng*, vol. 38, no. 1, pp. 163–169, 2021, doi: 10.1007/s11814-020-0687-y.

[52] M. F. Hanafi and N. Sapawe, “Effect of pH on the photocatalytic degradation of remazol brilliant blue dye using zirconia catalyst,” *Mater Today Proc*, vol. 31, pp. 260–262, 2020, doi: 10.1016/j.matpr.2020.05.746.

[53] Y. Guo, C. Zhou, L. Fang, Z. Liu, W. Li, and M. Yang, “Effect of pH on the Catalytic Degradation of Rhodamine B by Synthesized CDs/g-C $_3$ N $_4$ /Cu $_x$ O Composites,” *ACS Omega*, vol. 6, no. 12, pp. 8119–8130, Mar. 2021, doi: 10.1021/acsomega.0c05915.

[54] Y.-W. Chen and Y.-H. Hsu, “Effects of Reaction Temperature on the Photocatalytic Activity of TiO2 with Pd and Cu Cocatalysts,” *Catalysts*, vol. 11, no. 8, p. 966, Aug. 2021, doi: 10.3390/catal11080966.

[55] N. A. M. Barakat, M. A. Kanjwal, I. S. Chronakis, and H. Y. Kim, “Influence of temperature on the photodegradation process using Ag-doped TiO2 nanostructures: Negative impact with the nanofibers,” *J Mol Catal A Chem*, vol. 366, pp. 333–340, Jan. 2013, doi: 10.1016/j.molcata.2012.10.012.

[56] Y. Zheng, S. Wang, M. Shu, Y. Wang, and D. Cao, “Effective BiOCl Electrons Collector for Enhancing Photocarrier Separation of Bi2WO6/BiOCl Composite,” *Chemistry an international journal*, vol. 4, no. 3, pp. 765–775, 2022, doi: 10.3390/chemistry4030054.

[57] A. M. Ganose, M. Cuff, K. T. Butler, A. Walsh, and D. O. Scanlon, “Interplay of Orbital and Relativistic Effects in Bismuth Oxyhalides: BiOF, BiOCl, BiOBr, and BiOI,” *Chemistry of Materials*, vol. 28, no. 7, pp. 1980–1984, Apr. 2016, doi: 10.1021/acs.chemmater.6b00349.

[58] Z. Liang, C. Zhou, J. Yang, Q. Mo, Y. Zhang, and Y. Tang, “Visible light responsive Bi2WO6/BiOCl heterojunction with enhanced photocatalytic activity for degradation of tetracycline and rohdamine B,” *Inorg Chem Commun*, vol. 93, pp. 136–139, 2018, doi: 10.1016/j.inoche.2018.05.022.

[59] M. Xu *et al.*, “Efficient degradation of pollutants by Bi2WO6/BiOCl heterojunction activated peroxymonosulfate: Performance and mechanism,” *J Environ Chem Eng*, vol. 12, no. 2, p. 112156, Apr. 2024, doi: 10.1016/j.jece.2024.112156.

[60] J. Wang *et al.*, “Constructing of ultrathin Bi2WO6/BiOCl nanosheets with oxygen vacancies for photocatalytic oxidation of cyclohexane with air in solvent-free,” *Appl Surf Sci*, vol. 584, p. 152606, May 2022, doi: 10.1016/j.apsusc.2022.152606.

[61] M. Guo *et al.*, “Bi2WO6–BiOCl heterostructure with enhanced photocatalytic activity for efficient degradation of oxytetracycline,” *Sci Rep*, vol. 10, no. 1, p. 18401, Oct. 2020, doi: 10.1038/s41598-020-75003-x.

[62] W. Yang, B. Ma, W. Wang, Y. Wen, D. Zeng, and B. Shan, “Enhanced photosensitized activity of a BiOCl–Bi2WO6 heterojunction by effective interfacial charge transfer,” *Physical Chemistry Chemical Physics*, vol. 15, no. 44, p. 19387, 2013, doi: 10.1039/c3cp53628a.

[63] Z. K. Cui, J. Q. Zhou, D. W. Zeng, J. L. Zhang, W. J. Fa, and Z. Zheng, “From BiOCl to Bi $_2$ WO $_6$ in Bi–W–Cl–O solvothermal system: phase-morphology evolution and photocatalytic performance,” *Materials Technology*, vol. 30, no. 1, pp. 23–27, Jan. 2015, doi: 10.1179/1753555714Y.0000000196.

[64] N. A. Dhas, A. Ekhtiarzadeh, and K. S. Suslick, “Sonochemical Preparation of Supported Hydrodesulfurization Catalysts,” *J Am Chem Soc*, vol. 123, no. 34, pp. 8310–8316, Aug. 2001, doi: 10.1021/ja010516y.

[65] S. Zhu, C. Yang, F. Li, T. Li, M. Zhang, and W. Cao, “Improved photocatalytic Bi2WO6/BiOCl heterojunctions: One-step synthesis via an ionic-liquid assisted ultrasonic method and first-principles calculations,” *Molecular Catalysis*, vol. 435, pp. 33–48, Jul. 2017, doi: 10.1016/j.mcat.2017.03.016.

[66] J. Chen *et al.*, “Preparation of BiOCl/Bi2WO6 Photocatalyst for Efficient Fixation on Cotton Fabric: Applications in UV Shielding and Self-Cleaning Performances,” *Materials*, vol. 14, no. 22, p. 7002, Nov. 2021, doi: 10.3390/ma14227002.

[67] Z. Liang, C. Zhou, J. Yang, Q. Mo, Y. Zhang, and Y. Tang, “Visible light responsive Bi 2 WO 6 /BiOCl heterojunction with enhanced photocatalytic activity for degradation of tetracycline and rohdamine B,” *Inorg Chem Commun*, vol. 93, pp. 136–139, Jul. 2018, doi: 10.1016/j.inoche.2018.05.022.

[68] Y. Zhang, Y. Ma, L. Wang, Q. Sun, F. Zhang, and J. Shi, “Facile one-step hydrothermal synthesis of noble-metal-free hetero-structural ternary composites and their application in photocatalytic water purification,” *RSC Adv*, vol. 7, no. 80, pp. 50701–50712, 2017, doi: 10.1039/C7RA10732C.

[69] J. Nie, J. Schneider, F. Sieland, L. Zhou, S. Xia, and D. W. Bahnemann, “New insights into the surface plasmon resonance (SPR) driven photocatalytic H $_2$ production of Au–TiO $_2$,” *RSC Adv*, vol. 8, no. 46, pp. 25881–25887, 2018, doi: 10.1039/C8RA05450A.

[70] W. Hou and S. B. Cronin, “A Review of Surface Plasmon Resonance-Enhanced Photocatalysis,” *Adv Funct Mater*, vol. 23, no. 13, pp. 1612–1619, Apr. 2013, doi: 10.1002/adfm.201202148.

[71] M. Lemos de Souza, D. Pereira dos Santos, and P. Corio, “Localized surface plasmon resonance enhanced photocatalysis: an experimental and theoretical mechanistic investigation,” *RSC Adv*, vol. 8, no. 50, pp. 28753–28762, 2018, doi: 10.1039/C8RA03919D.

[72] Z. Chen, Y. Lu, Q. Zhang, D. Zhang, S. Li, and Q. Liu, “Electrochemistry Coupling Localized Surface Plasmon Resonance for Biochemical Detection,” 2022, pp. 15–35. doi: 10.1007/978-1-0716-1803-5_2.

[73] W. M. Haynes, D. R. Lide, and T. J. Bruno, Eds., *CRC Handbook of Chemistry and Physics*. CRC Press, 2016. doi: 10.1201/9781315380476.

[74] S. Das, R. Devireddy, and M. R. Gartia, “Surface Plasmon Resonance (SPR) Sensor for Cancer Biomarker Detection,” *Biosensors (Basel)*, vol. 13, no. 3, p. 396, Mar. 2023, doi: 10.3390/bios13030396.

[75] Y. Jiao, A. Hellman, Y. Fang, S. Gao, and M. Käll, “Schottky barrier formation and band bending revealed by first- principles calculations,” *Sci Rep*, vol. 5, no. 1, p. 11374, Jun. 2015, doi: 10.1038/srep11374.

[76] C. Buzea and I. Pacheco, “Gold and silver nanoparticles: Properties and toxicity,” in *Gold and Silver Nanoparticles*, Elsevier, 2023, pp. 59–82. doi: 10.1016/B978-0-323-99454-5.00007-X.

[77] K. Kim, J. Oh, T. W. Kim, J. H. Park, J. W. Han, and Y.-W. Suh, “Different catalytic behaviors of Pd and Pt metals in decalin dehydrogenation to naphthalene,” *Catal Sci Technol*, vol. 7, no. 17, pp. 3728–3735, 2017, doi: 10.1039/C7CY00569E.

[78] Z. Li and X. Meng, “Recent development on palladium enhanced photocatalytic activity: A review,” *J Alloys Compd*, vol. 830, p. 154669, Jul. 2020, doi: 10.1016/j.jallcom.2020.154669.

[79] H. Wang, B. Shi, Y. Liu, J. Guo, N. Chang, and X. Zhao, “Construction of Ag/Bi2WO6/BiOCl with enhanced photocatalytic performance for efficient degradation of organic pollutant,” *Inorg Chem Commun*, vol. 153, p. 110816, Jul. 2023, doi: 10.1016/j.inoche.2023.110816.

[80] X. Meng, Z. Li, and Z. Zhang, “Highly efficient degradation of phenol over a Pd-BiOBr Mott–Schottky plasmonic photocatalyst,” *Mater Res Bull*, vol. 99, pp. 471–478, Mar. 2018, doi: 10.1016/j.materresbull.2017.11.045.

[81] J. Yang *et al.*, “A compact Z-scheme heterojunction of BiOCl/Bi2WO6 for efficiently photocatalytic degradation of gaseous toluene,” *J Colloid Interface Sci*, vol. 631, pp. 44–54, Feb. 2023, doi: 10.1016/j.jcis.2022.11.023.

[82] M. Guo *et al.*, “Bi2WO6–BiOCl heterostructure with enhanced photocatalytic activity for efficient degradation of oxytetracycline,” *Sci Rep*, vol. 10, no. 1, p. 18401, Oct. 2020, doi: 10.1038/s41598-020-75003-x.

[83] B. Yao *et al.*, “Cost-effective Bi2WO6 for efficient degradation of rhodamine B and tetracycline,” *Journal of Materials Science: Materials in Electronics*, vol. 34, no. 4, p. 246, Feb. 2023, doi: 10.1007/s10854-022-09654-z.

[84] X. Meng, Z. Li, and Z. Zhang, “Pd-nanoparticle-decorated peanut-shaped BiVO4 with improved visible light-driven photocatalytic activity comparable to that of TiO2 under UV light,” *J Catal*, vol. 356, pp. 53–64, Dec. 2017, doi: 10.1016/j.jcat.2017.09.005.

[85] Z. Lu *et al.*, “Selective photodegradation of 2-mercaptobenzothiazole by a novel imprinted CoFe $_2$ O $_4$ /MWCNTs photocatalyst,” *RSC Adv*, vol. 5, no. 59, pp. 47820–47829, 2015, doi: 10.1039/C5RA08795C.

[86] Z. Wang and E. Hisahiro, “Recent trends in phenol synthesis by photocatalytic oxidation of benzene,” *Dalton Transactions*, vol. 52, no. 28, pp. 9525–9540, 2023, doi: 10.1039/D3DT01360J.

[87] A. A. Dubale *et al.*, “A highly stable metal–organic framework derived phosphorus doped carbon/Cu $_2$ O structure for efficient photocatalytic phenol degradation and hydrogen production,” *J Mater Chem A Mater*, vol. 7, no. 11, pp. 6062–6079, 2019, doi: 10.1039/C8TA12544A.

[88] P. O. Oladoye, T. O. Ajiboye, E. O. Omotola, and O. J. Oyewola, “Methylene blue dye: Toxicity and potential elimination technology from wastewater,” *Results in Engineering*, vol. 16, p. 100678, Dec. 2022, doi: 10.1016/j.rineng.2022.100678.

[89] H. Jiang, Y. Li, X. Wang, and X. Hong, “Construction of a hydrangea-like Bi $_2$ WO $_6$ /BiOCl composite as a high-performance photocatalyst,” *New Journal of Chemistry*, vol. 46, no. 6, pp. 2627–2634, 2022, doi: 10.1039/D1NJ05409K.

[90] J. Chen *et al.*, “Preparation of BiOCl/Bi2WO6 Photocatalyst for Efficient Fixation on Cotton Fabric: Applications in UV Shielding and Self-Cleaning Performances,” *Materials*, vol. 14, no. 22, p. 7002, Nov. 2021, doi: 10.3390/ma14227002.

[91] A. A. Oyekanmi, A. Ahmad, K. Hossain, and M. Rafatullah, “Adsorption of Rhodamine B dye from aqueous solution onto acid treated banana peel: Response surface methodology, kinetics and isotherm studies,” *PLoS One*, vol. 14, no. 5, p. e0216878, May 2019, doi: 10.1371/journal.pone.0216878.

[92] S. Khanam and S. K. Rout, “Enhanced Photocatalytic Oxidation of RhB and MB Using Plasmonic Performance of Ag Deposited on Bi2WO6,” *Chemistry (Easton)*, vol. 4, no. 2, pp. 272–296, Apr. 2022, doi: 10.3390/chemistry4020022.

[93] M. Utami, S. Wang, F. I. Fajarwati, S. N. Salsabilla, T. A. Dewi, and M. Fitri, “Enhanced Photodegradation of Rhodamine B Using Visible-Light Sensitive N-TiO2/rGO Composite,” *Crystals (Basel)*, vol. 13, no. 4, p. 588,

Chapter 3: Optimization of Synthesis Conditions of Hydrothermal-Prepared Bi_2WO_6/BiOCl Composite Heterojunctions

Abstract

In recent times, photocatalysis has gained attention for its application in water decontamination. Owing to its ambient operating conditions, low operating cost, and complete degradation of a variety of molecules, photocatalysis offers an effective means of water treatment. One such photocatalyst, Bi_2WO_6/BiOCl, has shown great promise for organic pollutant removal under visible light conditions. Herein, Bi_2WO_6/BiOCl composite heterojunction catalysts were fabricated using a typical hydrothermal technique. Multiple studies were conducted to examine the effects of several synthesis parameters on the photocatalytic properties of Bi_2WO_6/BiOCl. The optimal composition ratio between Bi_2WO_6:BiOCl, the calcination temperature, and the calcination time were determined through the degradation of a model organic dye, Rhodamine B (RhB). The as-prepared samples were analyzed using XRD and SEM to determine their crystal structure and surface morphologies. It was determined that samples prepared with a Bi_2WO_6:BiOCl ratio of 1:0.3 and calcined at 135°C for 12 hours exhibited the best photodegradation of RhB under visible-light illumination.

3.1 Introduction

Rapid population growth and increased industrialization have led to the release of many harmful materials into essential water supplies. Classical methods of water treatment, including membrane filtration, ion exchange, and adsorption, are often limited by the incomplete degradation of organic pollutants, all the while incurring substantial costs of operation [9]. Moreover, some of these processes have been linked to cancer-causing toxins. In order to address these challenges and provide better organic pollutant treatment, advanced oxidation processes (AOPs) have received growing attention [5], [6]. Among the AOPs, heterogeneous photocatalysis has proven to be an effective technique that is capable of providing complete treatment of aqueous organic pollutants without producing harmful by-products [40]. Photocatalysis uses semiconductor catalysts, which are activated upon exposure to light of the appropriate wavelength. When photocatalysts are excited, electrons (e^-) in the valence band (VB) move to the conduction band (CB), leaving positively charged holes (h^+) behind. The charge carrier species, electrons, and holes subsequently participate in redox reactions, providing non-selective treatment of a variety of target molecules [9].

Titanium dioxide (TiO_2) has long been regarded as the quintessential photocatalyst due to its high photocatalytic efficiency in the decomposition of a plethora of organic molecules [6], [10]. However, TiO_2 is limited by its wide band gap of 3.2 eV, making it usable only under UV radiation [6]. As ultraviolet radiation only accounts for a mere 4% of the solar spectrum, the use of this catalyst becomes expensive and impractical [11]. As such, research in this field aims to develop photocatalysts with low band gaps and high photocatalytic efficiencies.

One group of photocatalysts that has shown potential for water treatment is the Aurivillius family. This class of compounds is known for having several beneficial qualities, including good chemical stability, high conductivity, and excellent photoactivity [12]. Among the Aurivillius group, bismuth tungstate (Bi_2WO_6) has shown the most promising results. Consisting of a hierarchical structure made of $[WO_4]^{2-}$ layers located between $[Bi_2O_2]^{2+}$ units, Bi_2WO_6 has a narrow band gap in the range of 2.6-2.9 eV, making it visible-light responsive [12], [61]. Several studies have shown that Bi_2WO_6 displays excellent visible light degradation of several organic pollutants. However, this compound is hindered by high e^-/h^+ recombination, limiting its degradation rate [14]. One way of improving the performance of this catalyst is to composite it with a structure with good charge carrier separation. Such a material exists in bismuth oxychloride (BiOCl). Belonging to the bismuth oxyhalides, BiOCl comprises layers of $[Bi_2O_2]^{2+}$ intertwined between Cl^- atoms [15]. BiOCl exhibits considerable photocatalytic efficiency for organic pollutants with low-charge carrier recombination. It is important to note that BiOCl has a wide band gap of 3.2 eV, making it inapplicable for visible light application [14], [15]. However, this issue can be addressed by the fact that effective heterojunctions are often constructed by pairing large-band gap catalysts with low-band gap catalysts. Recent studies have shown that Bi_2WO_6/BiOCl composites display excellent visible light-responsive activity [20], [21], [22], [23], [24].

In this work, a simple hydrothermal method was used to synthesize Bi_2WO_6/BiOCl composite heterojunctions. Various synthesis parameters, including the composition ratio of Bi_2WO_6:BiOCl, calcination temperature, and calcination time, were optimized. The prepared samples were assessed through the degradation of a model dye, Rhodamine B (RhB), under visible light conditions.

3.2 Experimental

3.2.1 Hydrothermal Synthesis of Bi_2WO_6/BiOCl

All reagents were purchased from Sigma Aldrich and were used in their reagent grade without any additional purification. Bi_2WO_6/BiOCl composite heterojunctions were synthesized using a typical hydrothermal process [66], [67], [68]. First, 5 mmol of $Bi(NO_3)_3 \cdot 5H_2O$ (reagent grade, 98%) was added to 40 mL of distilled and deionized water (DDW) under magnetic stirring for 30 minutes at room temperature. Next, 2.5 mmol of $Na_2WO_4 \cdot 2H_2O$ (ACS reagent grade, ≥ 99%) was added to the solution under magnetic stirring for 30 minutes. Finally, a designated amount of NaCl (ACS reagent grade, ≥ 99 %) was dissolved in 20 mL of DDW, which was subsequently added to the previous solution in a dropwise manner over a period of 60 minutes under magnetic stirring. The combined mixture was transferred to a 100-mL Teflon-lined stainless-steel autoclave (Parr Instrument Company) and placed in a mechanical heater for a certain period at a select temperature. After cooling naturally to room temperature, the autoclave was removed from the heater, and the white precipitates were separated by centrifugation and rinsed several times with DDW and ethanol to remove any potential ionic species and impurities in the final product. The precipitates were dried overnight at a temperature of 60°C to obtain the composite Bi_2WO_6/BiOCl in its powdered form. To examine the effects of various synthesis parameters on photocatalytic performance, the amount of NaCl added, duration of thermal treatment, and time of thermal treatment were varied. First, the effect of the Bi_2WO_6:BiOCl composition ratio was studied by altering the amount of NaCl by preparing samples with 0.25, 0.50, 0.75, 1.0, 1.25, and 1.50 mmol of NaCl at 150°C for 12 hours. Next, the effect of the temperature of the thermal treatment was tested by heating samples for a period of 12 hours at temperatures of 120, 130, 135, 140, 150, and 180°C. Finally, to analyze the time of treatment, samples were heated for 9, 10.5, 12, 13.5, and 15 hours at a temperature of 135°C. Pure BiOCl and Bi_2WO_6 samples were also synthesized under the same conditions without the use of $Na_2WO_4 \cdot 2H_2O$ and $Bi(NO_3)_3 \cdot 5H_2O$ respectively.

3.2.2 Characterization

X-ray diffraction (XRD) was used to analyze the crystal structure of the as-prepared samples by using a Rigaku Ultima IV XRD with Cu K(α) radiation (λ = 0.15418 nm) operating at 40 mA and

40 kV from 10 to 80° (2θ). The surface morphology of the samples was evaluated through the use of scanning electron microscopy (SEM, JEOL JSM-7500F).

3.2.3 Photocatalytic Degradation Testing

The photocatalytic activity of the prepared samples was assessed through the degradation of the common textile dye Rhodamine B in water. 200 mL of 10 ppm RhB solution was added to the photoreactor alongside 0.5 g/L of catalyst samples. The mixture was stirred magnetically in the dark for a period of 20 minutes to allow for an adsorption-desorption equilibrium to be established between the catalyst and dye. Illumination was achieved using a 300 W tungsten halogen lamp (Ushio, USA) with a wavelength ranging from 310 to 800 nm. The lamp was equipped with a Kenko-Zeta filter (transmittance > 90%) to block irradiation with a wavelength less than 410 nm, ensuring photocatalysis would take place strictly under visible light. A cooling jacket was used to ensure the temperature would remain fixed at 20.0 ± 2.0°C. Once the light was turned on, 2 mL aliquots were drawn every 5 minutes and centrifuged for 5 minutes at a rate of 13,300 rpm using an accuSpin Micro 17 (Fisher Scientific) centrifuge to separate the catalyst from the solution. The supernatant was assessed using a UV-vis spectrophotometer (Genesys 10 UV, Thermo Scientific) with a fixed wavelength of 554 nm, corresponding to the characteristic absorption peak of RhB. The concentration of RhB was determined for each time interval using a calibration curve for the dye. The degradation rate of the RhB solution was calculated according to the following equation:

$$\text{RhB Degradation Efficiency (\%)} = \frac{c_0 - c}{c_0} \times 100\% \tag{3-1}$$

where c_0 and c are the RhB concentrations (ppm) initially and at time t (min) respectively.

3.3 Results and Discussion

3.3.1 XRD Analysis

XRD analysis was performed to investigate the crystallinity and phase purity of the hydrothermally synthesized Bi_2WO_6, BiOCl, and Bi_2WO_6/BiOCl samples under various conditions. Figure 3-1 shows the XRD patterns for Bi_2WO_6, BiOCl, and Bi_2WO_6/BiOCl fabricated with different ratios. The pure Bi_2WO_6 and BiOCl samples can be indexed according to the standardized JCPDS cards 39-0256 and 06-0249, respectively [94], [95]. By varying the amount of NaCl added during the synthesis process, the amount of BiOCl present in the composite was varied. Understanding the XRD patterns of the pure and mixed composites can help give insight into the properties that the composites will display. For Bi_2WO_6, some of the major peaks located at $2\theta = 28.3$, 32.8, 47.1, 58.5, 68.7, and 78.4° can be attributed to the planes of (131), (002), (202), (262), (004), and (204) respectively. These planes suggest that bismuth tungstate exists in a distinctive orthorhombic russelite phase [82], [83], [94]. The major diffraction peaks for BiOCl are located at $2\theta = 12.0$, 24.1, 25.9, 33.4, 36.5, 40.9, and 49.7°, corresponding to the planes of (100), (200), (101), (102), (111), (112), and (113). This specific sequence is unique to the tetragonal morphology of BiOCl, consisting of stacked [Cl-Bi-O-Bi-Cl] layers held together by van der Waals forces with Cl atoms [56], [57], [95]. This layered arrangement creates internal electric fields present along the (100) plane, resulting in excellent e^-/h^+ separation as well as low-charge carrier recombination. This makes BiOCl desirable in the modification of Bi_2WO_6.

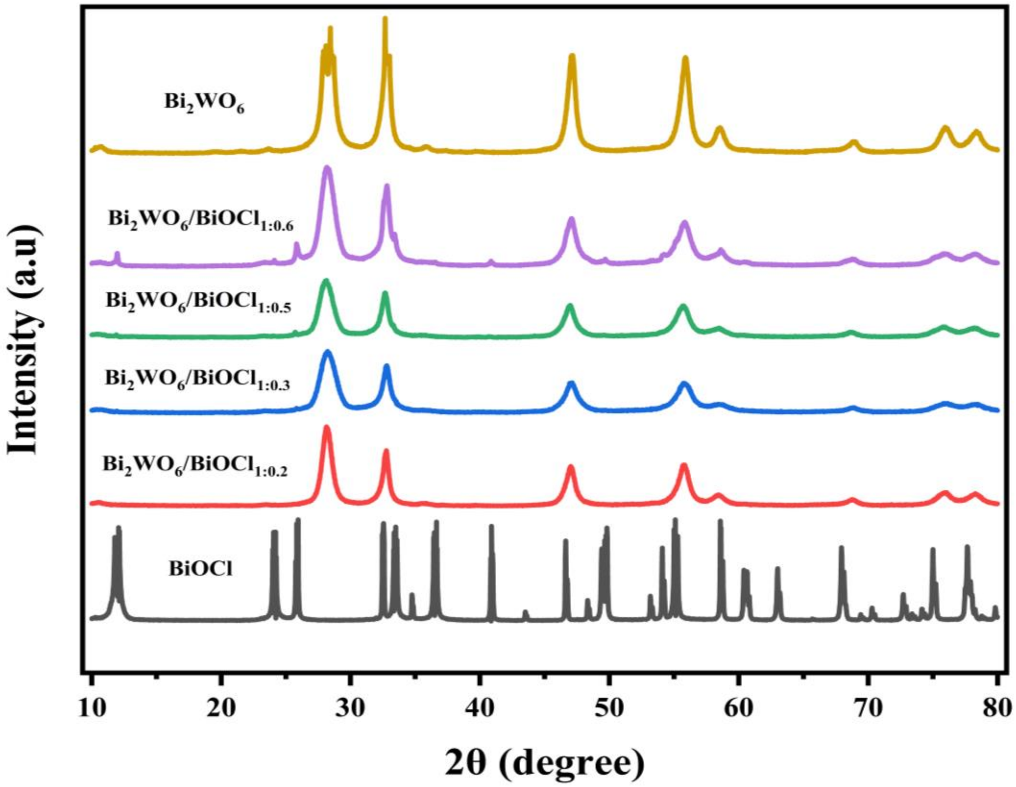

Figure 3-1: XRD patterns of Bi_2WO_6, BiOCl, and Bi_2WO_6/BiOCl with different composition ratios (calcination temperature 150℃ and calcination time 12 hours).

When considering the effects of changing the Bi_2WO_6:BiOCl ratio, the Figure 3-1 XRD plot indicates the co-existence of both Bi_2WO_6 and BiOCl, confirming the formation of the heterojunction. Since the composites mainly consisted of bismuth tungstate, their XRD patterns resembled very closely those of Bi_2WO_6, containing all of its major peaks. However, as more BiOCl is added, the peak intensities increase, indicating a higher degree of crystallinity. This is especially the case for the (100) crystal plane at $2\theta = 12.0°$, which becomes more pronounced. This is important as this peak is associated with strong e^-/h^+ separation, suggesting that the addition of BiOCl bolsters the charge carrier separation ability of the composite. Moreover, as with Bi_2WO_6, all the composites displayed their most intense peaks at (131) and (002), exhibiting preferential growth in that direction.

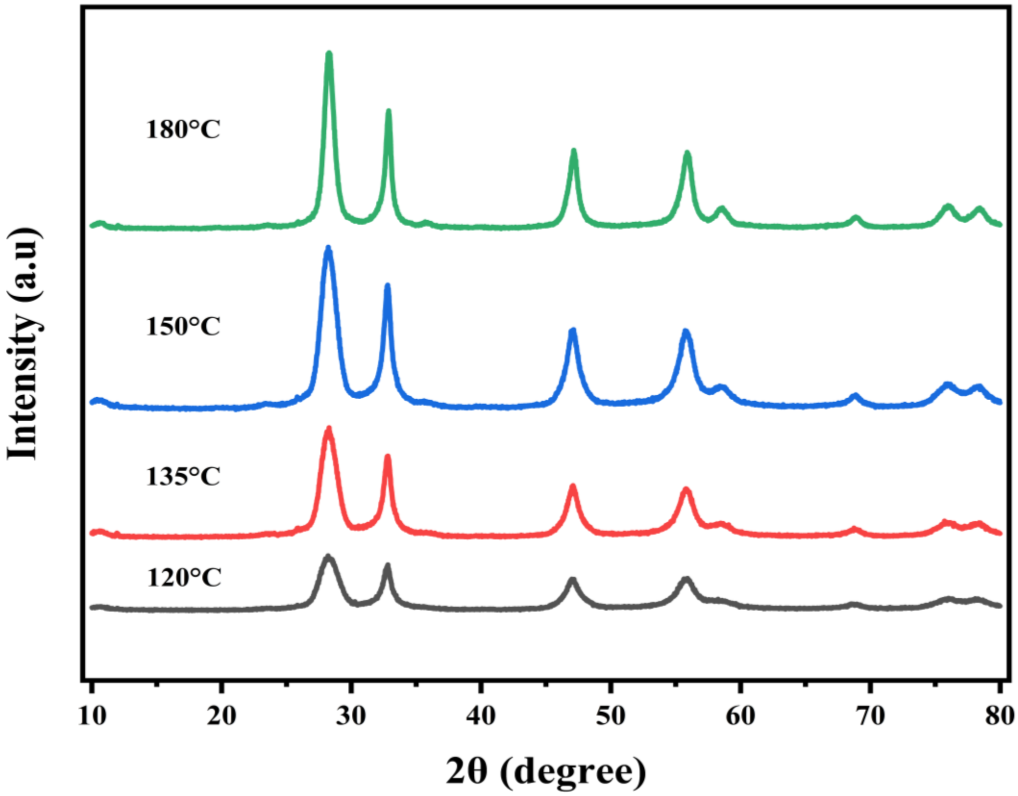

Figure 3-2: XRD patterns of $Bi_2WO_6/BiOCl$ samples synthesized under different temperatures (composition ratio 1:0.3 and calcination time 12 hours).

When considering the effects of the thermal treatment on the structure of $Bi_2WO_6/BiOCl$, it can be seen from Figure 3-2 that as the temperature of calcination is increased from 120 to 180°C, the XRD peaks become narrower and higher, suggesting better crystallite formation. This finding is consistent with similar studies conducted on this composite, which found that temperatures greater than 120°C are required to supply enough energy for sufficient crystal growth [82], [83], [84]. As mentioned, the crystal structure is closely related to the adsorption capacity of the catalyst. Thus, it is important to supply sufficient heat to form enough pores that contain active sites for pollutant adsorption.

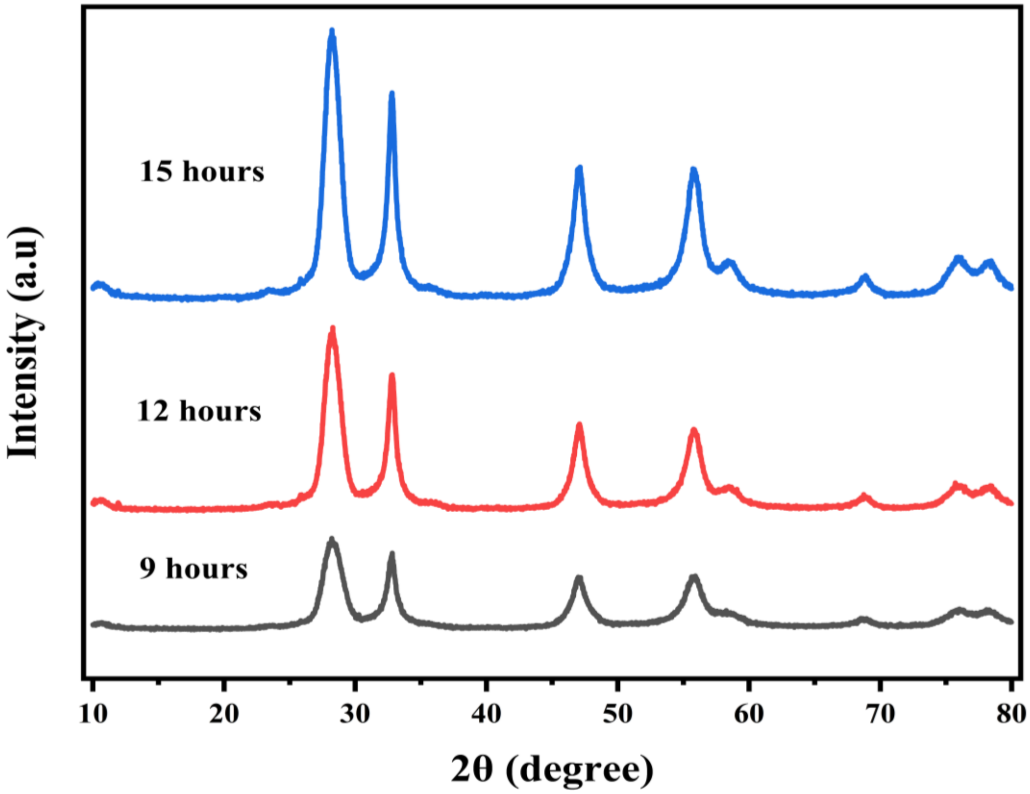

Figure 3-3: XRD patterns of Bi_2WO_6/BiOCl samples synthesized under different calcination times (composition ratio 1:0.3 and calcination temperature 135°C).

Much like the previous case, the XRD patterns for samples synthesized at different durations shown in Figure 3-3, display increased peaks at greater thermal exposure from 9 to 12 hours. This reveals that the degree of crystallinity of the Bi_2WO_6/BiOCl increases with longer treatment times. As with elevated temperatures, longer treatment times can increase the average particle size. This is important as larger particles have a lower surface area-to-volume ratio, decreasing the adsorption of pollutant molecules [11]. Moreover, the number of active sites also increases with longer treatment, allowing for more pollutants to be adsorbed. As such, in order to optimize the adsorption of pollutants, a balance must be found between a sufficient number of active sites and excessive particle size.

3.3.2 SEM Analysis

The surface morphologies of the prepared catalysts were observed through the use of SEM imaging. It can be seen in Figure 3-4 (a) that BiOCl consists of a nanosized plate structure. This presentation is a hallmark of the tetragonal matlockite structure of hydrothermally synthesized BiOCl, consisting of $[Bi_2O_2]^{2+}$ slabs held by double slabs of Cl^- atoms. The internal electric fields generated by the interactions between the bismuth oxide units and the chlorine atom induce electron-hole separation [96], [97]. As a result, this structure imparts excellent charge-charge separation and low recombination, which are beneficial properties for photocatalysts. The structure of Bi_2WO_6, as shown in Figure 3-4 (b), comprises ball-like structures with a mean diameter of 4.4 µm. This structure is consistent with hydrothermally fabricated Bi_2WO_6, resulting from a unique orthorhombic symmetry [23], [82]. Due to the high surface area of microspheres, Bi_2WO_6 is generally more conducive to the capture of light and sufficient adsorption for target pollutants, making it an effective photocatalyst.

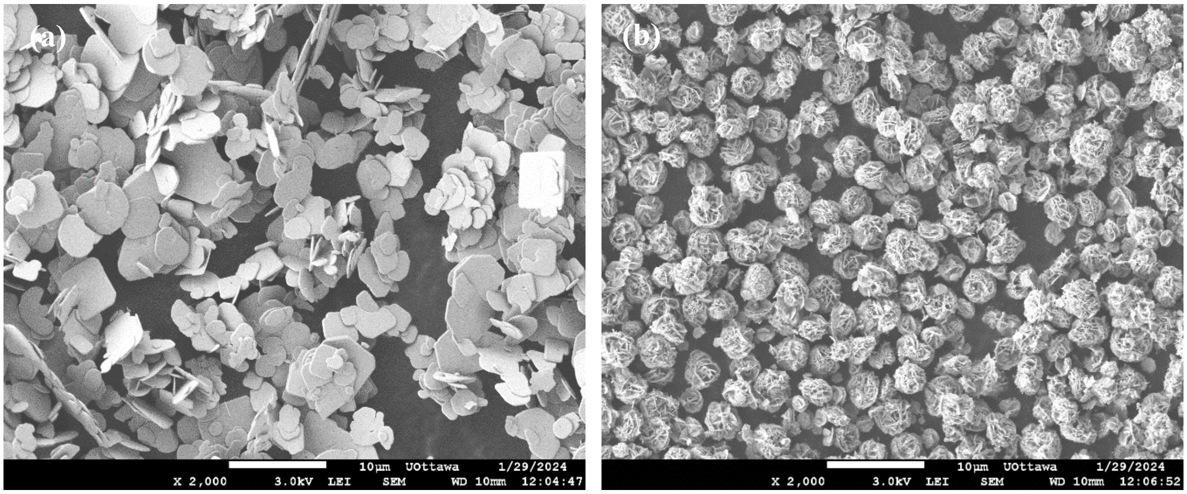

Figure 3-4: SEM images of (a) BiOCl and (b) Bi_2WO_6 synthesized at 150°C with a calcination time of 12 hours).

To study the effects of the composition ratio on the morphology of the composites, a constant temperature and time of calcination were set to 150°C for 12 hours. Since the samples are mostly composed of Bi_2WO_6, all of the composites resemble the SEM imaging of Bi_2WO_6 found in Figure 3-4 (b). Moreover, it was observed that as the fraction of BiOCl in the samples increased from 0.1 to 0.6, the heterojunctions exhibited plate-like extensions on their surface. This is most apparent in Figure 3-5 (d). This can affect the adsorption capability of the catalyst, as an excess number of plate-like structures can decrease the effective surface area, limiting the amount of target pollutant that can be captured on the catalytic surface.

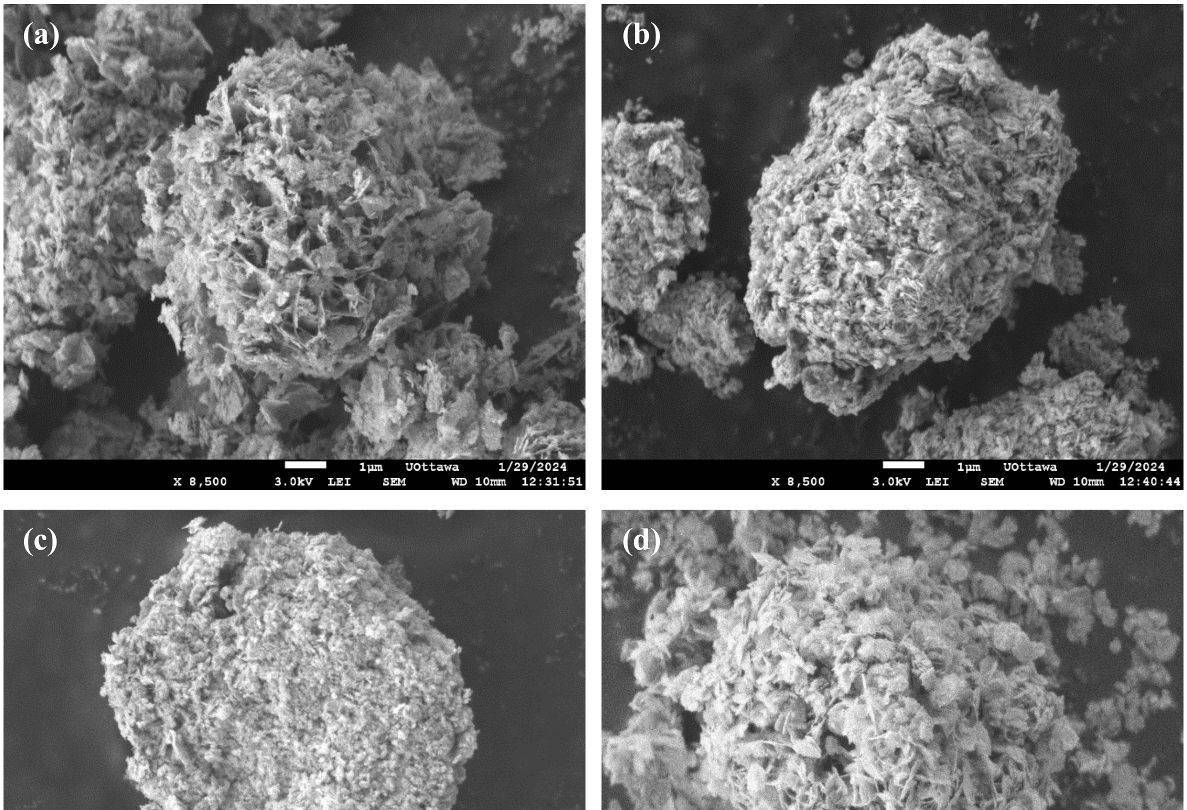

Figure 3-5: SEM images of Bi_2WO_6/BiOCl synthesized with different composition ratios of (a) 1:0.1 (b) 1:0.2 (c) 1:0.3 and (d) 1:0.6 (temperature of calcination 150°C, time of calcination of 12 hours).

To study the effects of the synthesis temperature on the catalyst morphology, samples were prepared at temperatures ranging from 120 to 180°C. It was observed from Figures 3-6 to 3-8 that an increase in temperature led to a decrease in the average particle size. When samples were synthesized at 120°C, it was determined that the average particle size was 13.42 µm, whereas samples prepared at 135°C and 180°C presented average sizes of 6.33 and 3.67 µm, respectively. This shows that temperature plays a significant role in determining the size of the Bi_2WO_6/BiOCl samples. This is important because the particle size of a catalyst impacts its adsorption and photocatalytic kinetics. Typically, it is the case that smaller particles have a greater surface area, improving the adsorption of target pollutants and, hence, enhancing the degradation kinetics.

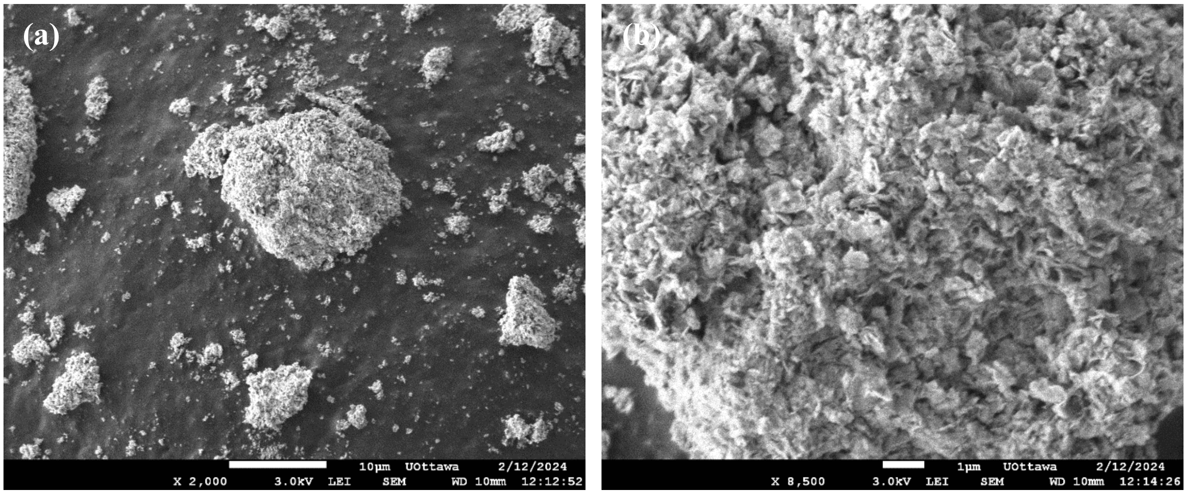

Figure 3-6: SEM images of Bi_2WO_6/BiOCl synthesized at 120°C at (a) low magnification and (b) high magnification (Bi_2WO_6:BiOCl ratio of 1:0.3, calcination time of 12 hours).

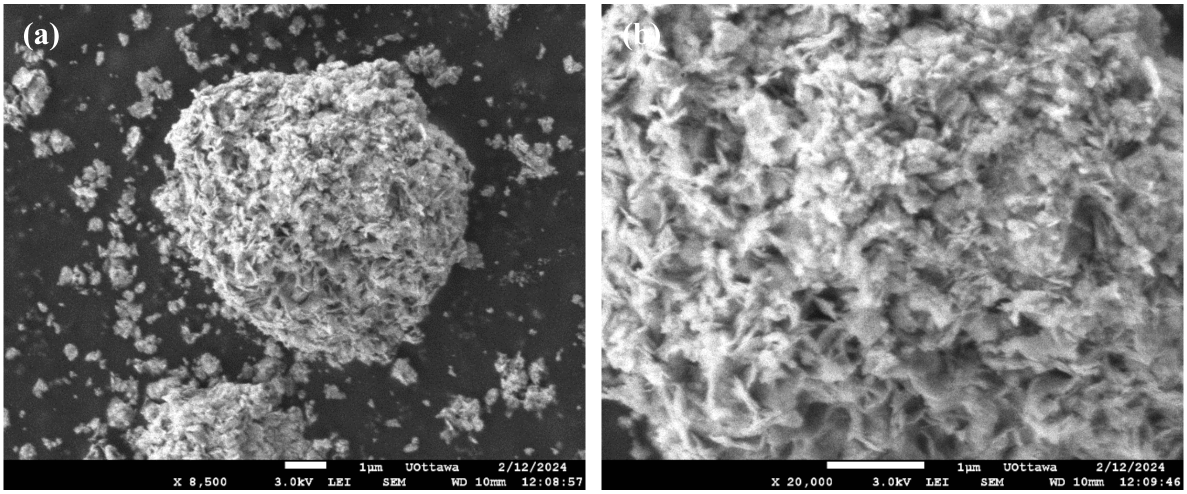

Figure 3-7: SEM images of Bi_2WO_6/BiOCl synthesized at 135°C at (a) low magnification and (b) high magnification (Bi_2WO_6:BiOCl ratio of 1:0.3, calcination time of 12 hours).

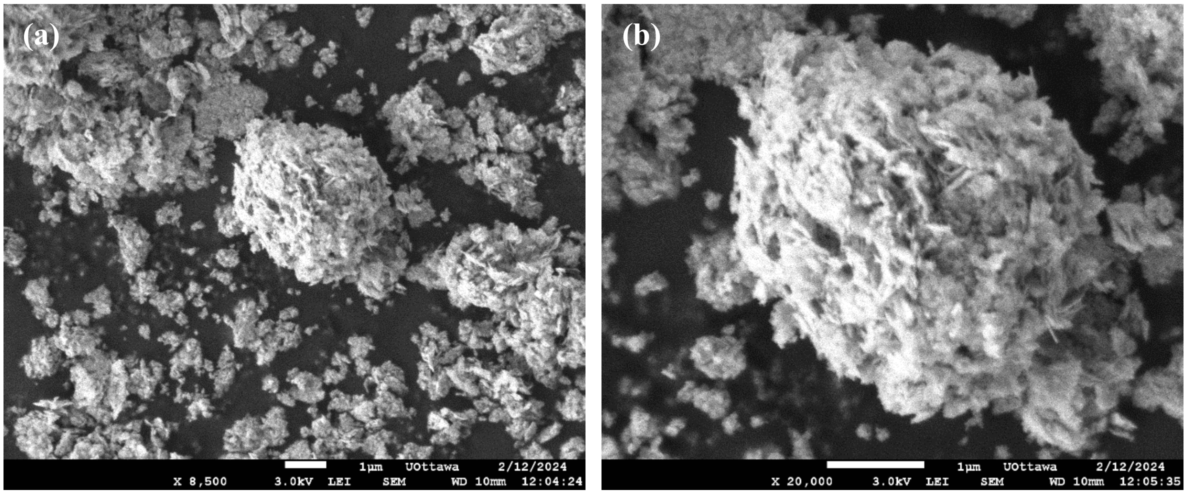

Figure 3-8: SEM images of Bi_2WO_6/BiOCl synthesized at 180°C at (a) low magnification and (b) high magnification (Bi_2WO_6:BiOCl ratio of 1:0.3, calcination time of 12 hours).

To assess the effects of the calcination time on the catalyst morphology, samples were prepared with a ratio of $Bi_2WO_6/BiOCl_{1:0.3}$ at 135°C for durations ranging from 9 to 15 hours. When the time of thermal treatment decreased from 12 to 9 hours (Figures 3-7 and 3-9), there was a less pronounced plate structure on the surface of the catalyst. Whereas when the time of treatment increased from 12 to 15 hours (Figures 3-7 and 3-10), the plates assumed a more closed presentation. This is interesting because it suggests that sufficient time is needed to allow for appropriate plate growth. However, it should be noted that at longer periods of treatment (i.e., 15 hours), the plates begin to exhibit preferential inward growth. This can affect the performance of the catalyst, as open-plated structures tend to be more conducive to pollutant adsorption and proper light harvesting.

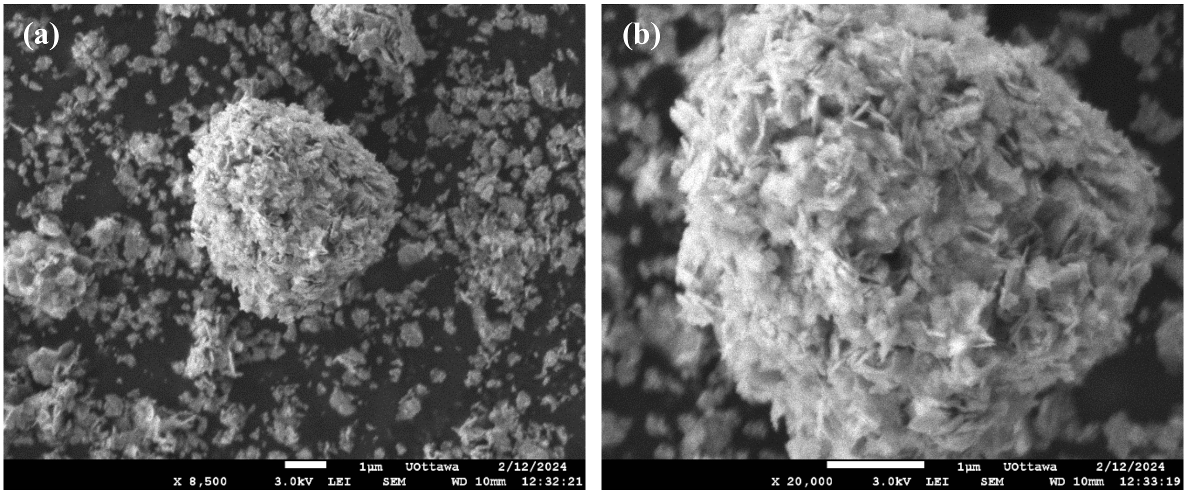

Figure 3-9: SEM images of Bi_2WO_6/BiOCl synthesized at a calcination time of 9 hours at (a) low magnification and (b) high magnification (Bi_2WO_6:BiOCl ratio of 1:0.3, calcination temperature of 135°C).

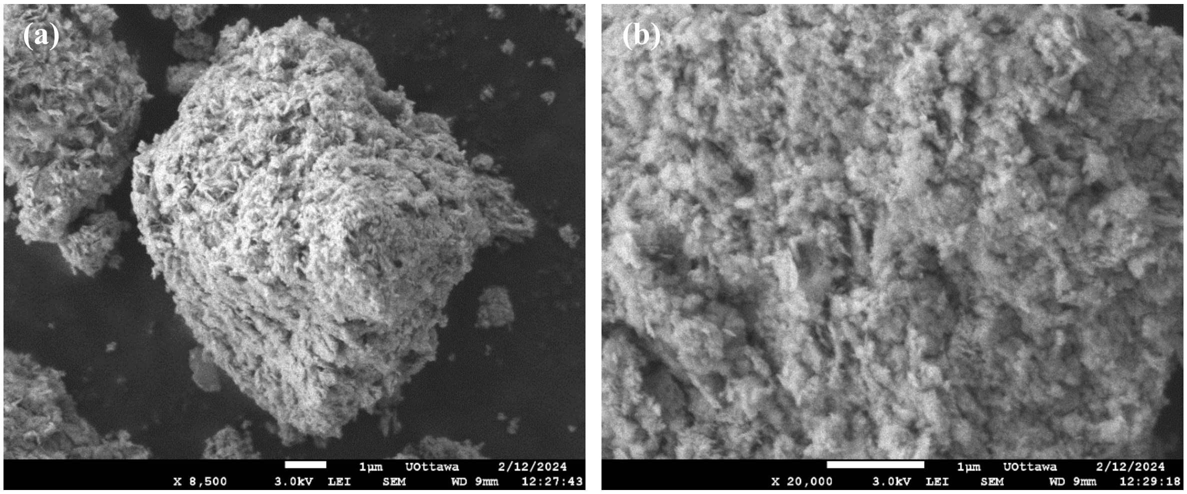

Figure 3-10: SEM images of Bi_2WO_6/BiOCl synthesized at a calcination time of 15 hours at (a) low magnification and (b) high magnification (Bi_2WO_6:BiOCl ratio of 1:0.3, calcination temperature of 135°C).

3.3.3 Photodegradation Experiments

3.3.3.1 Effect of Composition

The photocatalytic performance of the samples was tested through the decomposition of RhB dye under visible light illumination. In order to allow for an adsorption-desorption equilibrium to be established between the catalyst and dye, a 20-minute dark reaction was performed before each photocatalysis reaction was initiated. Additionally, RhB photolysis without the presence of a catalyst was investigated to measure the extent of RhB self-decomposition. It was found that after a period of 2 hours, photolysis resulted in negligible degradation of RhB, ruling out any potential dye-sensitization effect. To assess the effect of catalyst composition on photocatalytic performance, 0.5 g/L of samples were added to a photoreactor containing 200 mL of a 10 ppm RhB solution. When comparing the parent catalysts, it was found that BiOCl exhibited significantly greater degradation than Bi_2WO_6. This can be attributed to the excellent charge separation capacity arising from the plate-like structure of BiOCl.

Bi_2WO_6/BiOCl samples were tested under the same conditions as shown in Figure 3-11 and Table 3-1 below. It was found that higher amounts of BiOCl in the composites resulted in a significant improvement in photocatalytic activity. The highest recorded degradation was observed for the 1:0.3 sample, which had a rate constant of 0.541 min^{-1} and resulted in the near-complete degradation of RhB dye within 60 minutes of irradiation. This represented an improvement in photoactivity of 6.34 and 1.79 times compared to the pure Bi_2WO_6 and BiOCl samples, respectively. The enhanced photoactivity of the composites can be attributed to the synergistic effects resulting from the combination of Bi_2WO_6 and BiOCl, specifically increased visible light responsiveness and lower e^-/h^+ separation. This finding is consistent with the trends discussed for SEM imaging as well as XRD, which showed an increase in the peak at (100), for composites with BiOCl fractions greater than 0.2, suggesting the presence of electric fields and thus improved charge-carrier separation. Furthermore, the addition of plate structure to the surface of Bi_2WO_6 allows for the reinforcement of various reflections of visible light, thus creating more charge carrier species. It was also noted that the photoactivity began to decline for samples with a BiOCl content greater than 0.6. This could be a result of excess BiOCl plates present in the hierarchical structure of the heterojunction, causing less visible light activity and fewer free active sites needed for RhB adsorption. It is important to note that the samples for 1:0.3, 1:0.4, and 1:0.5 all exhibited similar behaviour in the degradation of RhB dye, as shown in Table 3-1. However, when selecting the optimal composition ratio, it is important to consider the economic feasibility of the project. As such, the sample with the least material required is often selected when multiple samples display similar properties. As a result, the optimal composition ratio of the Bi_2WO_6/BiOCl heterojunction was determined to be 1:0.3.

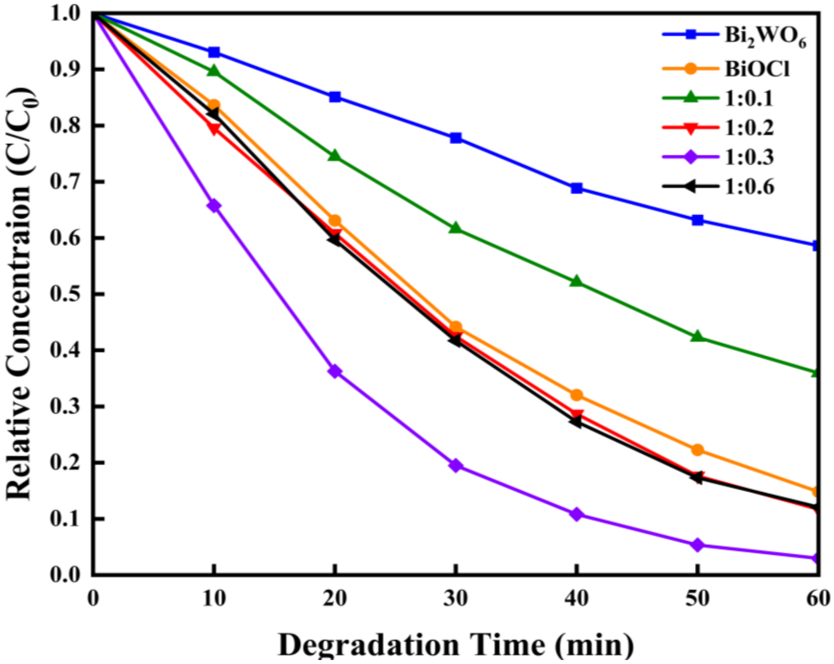

Figure 3-11: Photodegradation performance of BiOCl, Bi_2WO_6, and Bi_2WO_6/BiOCl heterojunctions synthesized with different composition ratios (catalyst dosage: 0.5 g/L, degradation temperature: 20 °C, initial pH: 4.8, and initial RhB concentration of 10 ppm).

Table 3-1: Pseudo-first order rate constant and degradation ratio of BiOCl, Bi_2WO_6, and Bi_2WO_6/BiOCl heterojunctions synthesized with different composition ratios.

Catalyst Composition	Degradation rate constant k_{app} (min^{-1})	Degradation ratio at 60 minutes (%)
Pure Bi_2WO_6	0.0101	41.38
Pure BiOCl	0.0313	85.17
$Bi_2WO_6/BiOCl_{1:0.1}$	0.0165	64.05
$Bi_2WO_6/BiOCl_{1:0.2}$	0.0336	88.28
$Bi_2WO_6/BiOCl_{1:0.3}$	0.0541	97.03
$Bi_2WO_6/BiOCl_{1:0.4}$	0.0525	96.98
$Bi_2WO_6/BiOCl_{1:0.5}$	0.0521	95.08
$Bi_2WO_6/BiOCl_{1:0.6}$	0.0334	87.92

3.3.3.2 Effect of Calcination Temperature

Using the optimized composition ratio found in the previous section, the optimal calcination temperature was determined as depicted in Figure 3-12 and Table 3-2. Samples fabricated for 12 hours at 120, 130, 135, 140, 150, and 180°C were evaluated for the degradation of RhB. When the temperature of calcination was increased from 150 to 180°C, the degradation rate decreased from 0.0565 to 0.0379 min^{-1}. This can be explained by assessing the XRD results, which showed that at higher temperatures, there is preferential growth along the (131) and (200) planes, suggesting that the crystal structure of the composite is significantly impacted by changes in temperature. This is consistent with studies conducted on Bi_2WO_6/BiOCl structures, which found that elevated temperatures can cause changes in the crystal structure and cause the formation of larger crystals from particle aggregation [80], [81], [83]. This can have an adverse impact on the photodegradation capacity, as aggregation on the surface of the catalyst can lead to photon scattering, thus limiting the number of photogenerated e^- and h^+ [11]. To a certain extent, this trait can be beneficial, leading to an appreciable surface area for pollutant adsorption; however, exaggerated crystal growth can also lead to the insufficient formation of charge carrier species, leading to a decline in activity. This is especially the case for higher temperatures with long durations of thermal treatment, such as 12 hours. As such, hydrothermally synthesized catalysts typically exhibit optimal performance at low temperatures with longer durations to allow for appropriate crystal growth. Conversely, it was determined that decreasing the temperature from 150 to 135°C resulted in an increase in activity by a factor of 1.77 with a rate constant of 0.1002 mins^{-1}. This indicates that sufficient crystal growth is achieved, allowing for good adsorption capacity as well as limited photonic scattering, allowing for appreciable charge carrier generation to take place. To fine-tune the optimal temperature, samples were also synthesized at 130 and 120°C. However, these samples demonstrated slightly depleted photocatalytic degradation of RhB, suggesting that their structures did not have sufficient crystal growth, as shown in the XRD and SEM imaging. Therefore, it was determined that for the degradation of RhB, $Bi_2WO_6/BiOCl_{1:0.3}$ composites demonstrate optimal performance when calcined at 135°C.

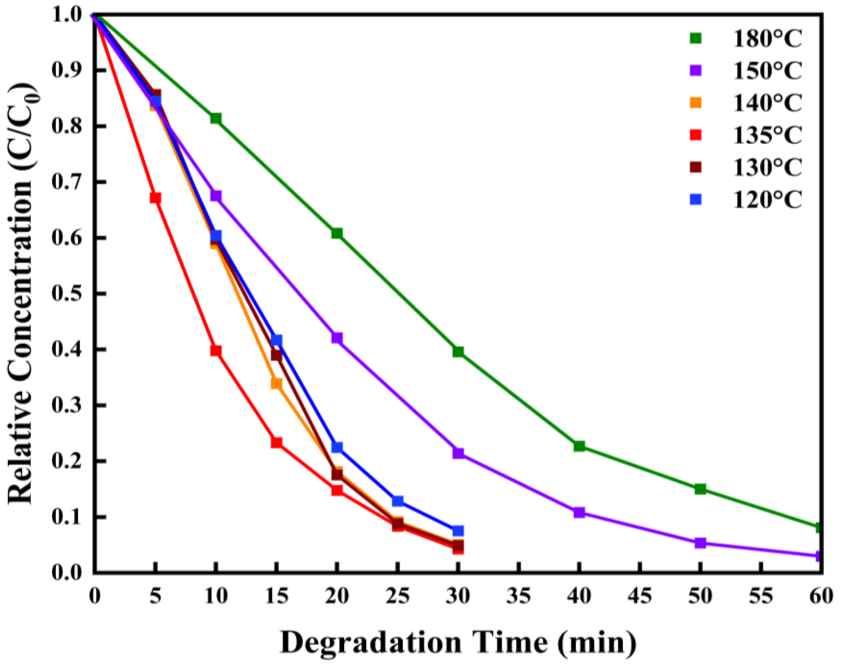

Figure 3-12: Photodegradation performance of Bi_2WO_6/BiOCl heterojunctions under different calcination temperatures (calcination time 12 hours, catalyst dosage: 0.5 g/L, degradation temperature: 20°C; initial pH: 4.8, and initial RhB concentration of 10 ppm).

Table 3-2: Pseudo-first order rate constant and degradation ratio of BiOCl, Bi_2WO_6, and Bi_2WO_6/BiOCl heterojunctions synthesized with different calcination temperatures.

Calcination Temperature (°C)	Degradation rate constant k_{app} (min^{-1})	Degradation ratio at 30 minutes (%)
180	0.0379	60.41
150	0.0541	78.59
140	0.0903	94.89
135	0.1002	97.19
130	0.0918	95.09
120	0.0781	92.46

3.3.3.3 Effect of Calcination Time

The performance of Bi_2WO_6/BiOCl samples synthesized under various times of thermal treatment was tested and shown in Figure 3-13 and Table 3-3 below. Using the optimal composition ratio (1:0.3 of Bi_2WO_6:BiOCl) and the optimal treatment temperature (135°C) determined in the previous sections, samples were synthesized at times ranging from 9 to 13.5 hours. When increasing the duration of treatment from 9 to 12 hours, there was an appreciable increase in the RhB degradation rate from 0.0779 to 0.1002 min^{-1}, representing a 28.6% improvement in photocatalytic activity. This change can be explained by the fact that, much like the temperature, the synthesis time can affect the particle size, ultimately influencing how the catalyst interacts with the pollutant molecules. Typically, it is the case that samples synthesized at low to moderate temperatures (i.e., 135°C) require longer periods of calcination to allow for sufficient pore formation [11], [82], [84]. Therefore, it can be deduced that an increase from 9 to 12 hours leads to sufficient plate and pore formation on the catalytic surface, as shown in Figures 3-9 and 3-7. Furthermore, prolonged thermal treatments can lead to excessive plate formation, increased light scattering, and lower photonic efficiency. This explains why there was a drop in the photocatalytic activity when the time of treatment was increased beyond 12 hours. This trend is also reflected in the XRD results, which showed sequential growth along the major peaks at 15 hours, suggesting exaggerated plate growth along the surface of the heterojunction. Hence, it was determined that $Bi_2WO_6/BiOCl_{1:0.3}$ synthesized at 135°C for 12 hours exhibited the highest photodegradation of RhB under visible light.

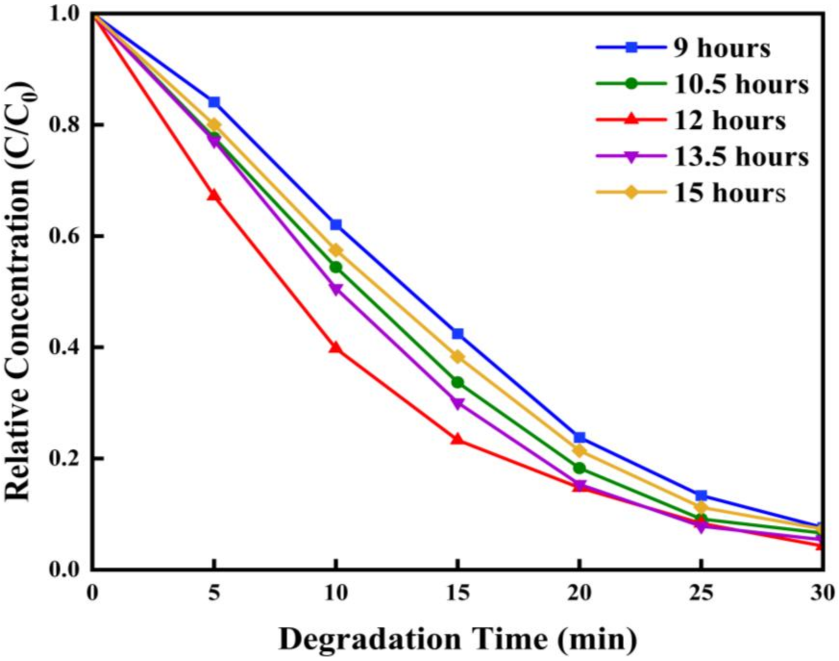

Figure 3-13: Photodegradation performance of Bi_2WO_6/BiOCl heterojunctions under different calcination times (calcination temperature: 135°C, catalyst dosage: 0.5 g/L, degradation temperature: 20°C, initial pH: 4.8, and initial RhB concentration of 10 ppm).

Table 3-3: Pseudo-first order rate constant and degradation ratio of BiOCl, Bi_2WO_6, and Bi_2WO_6/BiOCl heterojunctions synthesized with different calcination times.

Calcination Time (hours)	Degradation rate constant k_{app} (min^{-1})	Degradation ratio at 30 minutes (%)
9	0.0768	92.39
10.5	0.0875	93.40
12	0.1002	97.19
13.5	0.0944	94.58
15	0.0813	92.67

3.4 Conclusion

In this work, Bi_2WO_6/BiOCl composite heterojunctions were synthesized using the hydrothermal technique under various conditions. Through the degradation of the model organic dye, RhB, it was shown that the composition between the parent compounds, Bi_2WO_6:BiOCl, temperature of thermal treatment, and duration of thermal treatment play a significant role in how the catalyst behaves. It was determined that Bi_2WO_6/BiOCl demonstrates the highest photocatalytic performance when prepared with a composition ratio of 1:0.3, a temperature of 135°C, and a period of 12 hours. Through the use of XRD and SEM analyses, it was shown that at these conditions, a sufficient composite particle size and pore formation were reached, allowing for sufficient adsorption and light harvesting, leading to a significant improvement in photocatalytic activity. Overall, this study demonstrated that Bi_2WO_6/BiOCl heterojunctions exhibit excellent visible light-driven performance for organic pollutants and are a worthy candidate for water treatment applications.

3.5 Nomenclature

k_{app}	Apparent degradation rate constant
E_g	Band gap energy
$Bi(NO_3)_3·5H_2O$	Bismuth (III) nitrate pentahydrate
BiOCl	Bismuth oxychloride
BiOX	Bismuth oxyhalide
Bi_2WO_6	Bismuth tungstate
c_t	Concentration at specific time
c	Concentration of substrate
E	Degradation efficiency
e^-	Electron
h^+	Hole
•OH	Hydroxyl radical
c_0	Initial concentration
O_2	Oxygen
ppm	Part per million
NaCl	Sodium chloride
$Na_2WO_4·2H_2O$	Sodium nitrate dihydrate
$O_2^{•-}$	Superoxide radical
t	Time
TiO_2	Titanium dioxide
H_2O	Water

3.6 Greek Letters

θ	Angle between sample and x-ray source

3.7 Abbreviations

AOP	Advanced Oxidation Process
ACS	American Chemical Society
CB	Conduction Band
DDW	Distilled and Deionized Water
JCPDS	Joint Committee on Powder Diffraction Standards
RhB	Rhodamine B
SEM	Scanning Electron Microscopy
UV	Ultraviolet
UV-vis	Ultraviolet Visible
VB	Valence Band
XRD	X-ray Diffraction

References

[1] M. A. Al-Nuaim, A. A. Alwasiti, and Z. Y. Shnain, "The photocatalytic process in the treatment of polluted water," *Chemical Papers 2022 77:2*, vol. 77, no. 2, pp. 677–701, Oct. 2022, doi: 10.1007/S11696-022-02468-7.

[2] E. Koncagül and R. Connor, "The United Nations World Water Development Report 2023: partnerships and cooperation for water; facts, figures and action examples," Paris, 2023.

[3] S. Mishra and B. Sundaram, "A review of the photocatalysis process used for wastewater treatment," *Mater Today Proc*, Jul. 2023, doi: 10.1016/J.MATPR.2023.07.147.

[4] G. Crini and E. Lichtfouse, "Advantages and disadvantages of techniques used for wastewater treatment," *Environ Chem Lett*, vol. 17, no. 1, pp. 145–155, Mar. 2019, doi: 10.1007/s10311-018-0785-9.

[5] A. O. Oluwole, E. O. Omotola, and O. S. Olatunji, "Pharmaceuticals and personal care products in water and wastewater: a review of treatment processes and use of photocatalyst immobilized on functionalized carbon in AOP degradation," *BMC Chem*, vol. 14, no. 1, p. 62, Dec. 2020, doi: 10.1186/s13065-020-00714-1.

[6] G. Ren *et al.*, "Recent Advances of Photocatalytic Application in Water Treatment: A Review," *Nanomaterials 2021, Vol. 11, Page 1804*, vol. 11, no. 7, p. 1804, Jul. 2021, doi: 10.3390/NANO11071804.

[7] S. K. Loeb *et al.*, "The Technology Horizon for Photocatalytic Water Treatment: Sunrise or Sunset?," *Environ Sci Technol*, vol. 53, no. 6, pp. 2937–2947, Mar. 2019, doi: 10.1021/ACS.EST.8B05041.

[8] M. M. Ayyub and C. N. R. Rao, "Design of efficient photocatalysts through band gap engineering," in *Nanostructured Photocatalysts*, Elsevier, 2020, pp. 1–18. doi: 10.1016/B978-0-12-817836-2.00001-6.

[9] S. Mishra and B. Sundaram, "A review of the photocatalysis process used for wastewater treatment," *Mater Today Proc*, Jul. 2023, doi: 10.1016/j.matpr.2023.07.147.

[10] S. Y. Lee and S. J. Park, "TiO2 photocatalyst for water treatment applications," *Journal of Industrial and Engineering Chemistry*, vol. 19, no. 6, pp. 1761–1769, Nov. 2013, doi: 10.1016/J.JIEC.2013.07.012.

[11] L. Wang and J. Yu, "Principles of photocatalysis," 2023, pp. 1–52. doi: 10.1016/B978-0-443-18786-5.00002-0.

[12] D. O. Charkin, D. N. Lebedev, and S. M. Kazakov, "Multiple cation and anion substitutions into the structures of Bi2WO6 and PbBi3WO8Cl," *J Alloys Compd*, vol. 536, pp. 155–160, Sep. 2012, doi: 10.1016/J.JALLCOM.2012.04.113.

[13] Z. Zhu *et al.*, “Recent progress in Bi_2WO_6-Based photocatalysts for clean energy and environmental remediation: Competitiveness, challenges, and future perspectives,” *Nano Select*, vol. 2, no. 2, pp. 187–215, Feb. 2021, doi: 10.1002/nano.202000127.

[14] Z. Li, L. Zhu, W. Wu, S. Wang, and L. Qiang, “Highly efficient photocatalysis toward tetracycline under simulated solar-light by Ag+-CDs-Bi2WO6: Synergistic effects of silver ions and carbon dots,” *Appl Catal B*, vol. 192, pp. 277–285, Sep. 2016, doi: 10.1016/j.apcatb.2016.03.045.

[15] X. Yu, J. Yang, K. Ye, X. Fu, Y. Zhu, and Y. Zhang, “Facile one-step synthesis of BiOCl/BiOI heterojunctions with exposed {001} facet for highly enhanced visible light photocatalytic performances,” *Inorg Chem Commun*, vol. 71, pp. 45–49, Sep. 2016, doi: 10.1016/J.INOCHE.2016.06.034.

[16] Z. Liang, C. Zhou, J. Yang, Q. Mo, Y. Zhang, and Y. Tang, “Visible light responsive Bi 2 WO 6 /BiOCl heterojunction with enhanced photocatalytic activity for degradation of tetracycline and rohdamine B,” *Inorg Chem Commun*, vol. 93, pp. 136–139, Jul. 2018, doi: 10.1016/j.inoche.2018.05.022.

[17] G. Zhang, Y. Tan, Z. Sun, and S. Zheng, “Synthesis of BiOCl/TiO 2 heterostructure composites and their enhanced photocatalytic activity,” *J Environ Chem Eng*, vol. 5, no. 1, pp. 1196–1204, Feb. 2017, doi: 10.1016/j.jece.2017.01.040.

[18] Q. Su *et al.*, “Construction of a Bioinspired Hierarchical $BiVO_4$/BiOCl Heterojunction and Its Enhanced Photocatalytic Activity for Phenol Degradation,” *ACS Appl Mater Interfaces*, vol. 13, no. 28, pp. 32906–32915, Jul. 2021, doi: 10.1021/acsami.1c05117.

[19] X. Zhang, G. Xu, J. Hu, J. Lv, J. Wang, and Y. Wu, “Fabrication and photocatalytic performances of BiOCl nanosheets modified with ultrafine Bi_2O_3 nanocrystals,” *RSC Adv*, vol. 6, no. 68, pp. 63241–63249, 2016, doi: 10.1039/C6RA09919J.

[20] N. Tahmasebi, Z. Maleki, and P. Farahnak, “Enhanced photocatalytic activities of Bi2WO6/BiOCl composite synthesized by one-step hydrothermal method with the assistance of HCl,” *Mater Sci Semicond Process*, vol. 89, pp. 32–40, Jan. 2019, doi: 10.1016/j.mssp.2018.08.026.

[21] Y. Huang *et al.*, “Peroxymonosulfate Activation by Bi2WO6/BiOCl Heterojunction Nanocomposites under Visible Light for Bisphenol A Degradation,” *Nanomaterials*, vol. 11, no. 11, p. 3130, Nov. 2021, doi: 10.3390/nano11113130.

[22] M. Guo *et al.*, “Bi2WO6–BiOCl heterostructure with enhanced photocatalytic activity for efficient degradation of oxytetracycline,” *Sci Rep*, vol. 10, no. 1, p. 18401, Oct. 2020, doi: 10.1038/s41598-020-75003-x.

[23] L. Derikvand and N. Tahmasebi, “Synthesis and photocatalytic performance of Bi2WO6/BiOX (X=Cl, Br, I) composites for RhB degradation under visible light,” *Korean Journal of Chemical Engineering*, vol. 38, no. 1, pp. 163–169, Jan. 2021, doi: 10.1007/s11814-020-0687-y.

[24] J. Chen *et al.*, “Preparation of BiOCl/Bi2WO6 Photocatalyst for Efficient Fixation on Cotton Fabric: Applications in UV Shielding and Self-Cleaning Performances,” *Materials*, vol. 14, no. 22, p. 7002, Nov. 2021, doi: 10.3390/ma14227002.

[25] A. Nazir, P. Huo, H. Wang, Z. Weiqiang, and Y. Wan, “A review on plasmonic-based heterojunction photocatalysts for degradation of organic pollutants in wastewater,” *J Mater Sci*, vol. 58, no. 15, pp. 6474–6515, Apr. 2023, doi: 10.1007/s10853-023-08391-w.

[26] Z. Li and X. Meng, “Recent development on palladium enhanced photocatalytic activity: A review,” *J Alloys Compd*, vol. 830, p. 154669, Jul. 2020, doi: 10.1016/j.jallcom.2020.154669.

[27] M. Arumugam, R. Koutavarapu, K.-K. Seralathan, S. Praserthdam, and P. Praserthdam, “Noble metals (Pd, Ag, Pt, and Au) doped bismuth oxybromide photocatalysts for improved visible light-driven catalytic activity for the degradation of phenol,” *Chemosphere*, vol. 324, p. 138368, May 2023, doi: 10.1016/j.chemosphere.2023.138368.

[28] Z. Li and X. Meng, “Recent development on palladium enhanced photocatalytic activity: A review,” *J Alloys Compd*, vol. 830, p. 154669, Jul. 2020, doi: 10.1016/j.jallcom.2020.154669.

[29] R. Wang, B. Li, Y. Xiao, X. Tao, X. Su, and X. Dong, “Optimizing Pd and Au-Pd decorated Bi2WO6 ultrathin nanosheets for photocatalytic selective oxidation of aromatic alcohols,” *J Catal*, vol. 364, pp. 154–165, 2018, doi: 10.1016/j.jcat.2018.05.015.

[30] S. Y. Lee and S. J. Park, “TiO2 photocatalyst for water treatment applications,” *Journal of Industrial and Engineering Chemistry*, vol. 19, no. 6, pp. 1761–1769, Nov. 2013, doi: 10.1016/J.JIEC.2013.07.012.

[31] Alexander Eibner, “Action of Light on Pigments I,” *Chem-ZTG*, pp. 753–755, 1911.

[32] C. F. Goodeve and J. A. Kitchener, “The mechanism of photosensitisation by solids,” *Transactions of the Faraday Society*, vol. 34, p. 902, 1938, doi: 10.1039/tf9383400902.

[33] V.N. Filimonov, “Photocatalytic Oxidation of Gaseous Isopropanol on ZnO + TiO 2,” *Dokl Akad Nauk SSSR*, vol. 154, no. 4, pp. 922–925, 1964.

[34] A. FUJISHIMA and K. HONDA, “Electrochemical Photolysis of Water at a Semiconductor Electrode,” *Nature*, vol. 238, no. 5358, pp. 37–38, Jul. 1972, doi: 10.1038/238037a0.

[35] S. Zhu and D. Wang, “Photocatalysis: Basic Principles, Diverse Forms of Implementations and Emerging Scientific Opportunities,” *Adv Energy Mater*, vol. 7, no. 23, Dec. 2017, doi: 10.1002/aenm.201700841.

[36] S. Mishra and B. Sundaram, “Efficacy of nanoparticles as photocatalyst in leachate treatment,” *Nanotechnology for Environmental Engineering*, vol. 7, no. 1, pp. 173–192, Mar. 2022, doi: 10.1007/s41204-021-00209-x.

[37] H. Wang *et al.*, “Semiconductor heterojunction photocatalysts: design, construction, and photocatalytic performances,” *Chem Soc Rev*, vol. 43, no. 15, p. 5234, Jul. 2014, doi: 10.1039/C4CS00126E.

[38] P. Doran, *Engineering Principles Second Edition*. 2013. Accessed: Nov. 19, 2022. [Online]. Available: http://www.sciencedirect.com:5070/book/9780122208515/bioprocess-engineering-principles

[39] S. A. Heredia Deba, B. A. Wols, D. R. Yntema, and R. G. H. Lammertink, “Photocatalytic ceramic membrane: Effect of the illumination intensity and distribution,” *J Photochem Photobiol A Chem*, vol. 437, p. 114469, Mar. 2023, doi: 10.1016/j.jphotochem.2022.114469.

[40] Suresh C. Ameta and Rakshit Ameta, *Advanced Oxidation Processes for Wastewater Treatment Emerging Green Chemical Technology*, 1st ed. Elsevier, 2018.

[41] T. G. Mayerhöfer, S. Pahlow, and J. Popp, “The Bouguer-Beer-Lambert Law: Shining Light on the Obscure.,” *Chemphyschem*, vol. 21, no. 18, pp. 2029–2046, Sep. 2020, doi: 10.1002/cphc.202000464.

[42] C. Belver, J. Bedia, M. Peñas-Garzón, V. Muelas-Ramos, A. Gómez-Avilés, and J. J. Rodriguez, “Structured photocatalysts for the removal of emerging contaminants under visible or solar light,” in *Visible Light Active Structured Photocatalysts for the Removal of Emerging Contaminants*, Elsevier, 2020, pp. 41–98. doi: 10.1016/B978-0-12-818334-2.00003-1.

[43] M. Bodzek and M. Rajca, “Photocatalysis in the treatment and disinfection of water. Part I. Theoretical backgrounds / Fotokataliza w oczyszczaniu i dezynfekcji wody część i. podstawy teoretyczne,” *Ecological Chemistry and Engineering S*, vol. 19, no. 4, pp. 489–512, Nov. 2012, doi: 10.2478/v10216-011-0036-5.

[44] Y. Liang and J. Shi, “Effect of Halide Ions on the Microstructure of Bi2WO6 with Enhanced Removal of Rhodamine B,” *J Inorg Organomet Polym Mater*, vol. 30, no. 8, pp. 2872–2880, Aug. 2020, doi: 10.1007/s10904-019-01437-0.

[45] P. O. Oladoye, T. O. Ajiboye, E. O. Omotola, and O. J. Oyewola, “Methylene blue dye: Toxicity and potential elimination technology from wastewater,” *Results in Engineering*, vol. 16, p. 100678, Dec. 2022, doi: 10.1016/j.rineng.2022.100678.

[46] B. Liu, X. Zhao, C. Terashima, A. Fujishima, and K. Nakata, “Thermodynamic and kinetic analysis of heterogeneous photocatalysis for semiconductor systems,” *Physical Chemistry Chemical Physics*, vol. 16, no. 19, p. 8751, 2014, doi: 10.1039/c3cp55317e.

[47] A. H. Navidpour, S. Abbasi, D. Li, A. Mojiri, and J. L. Zhou, “Investigation of Advanced Oxidation Process in the Presence of TiO2 Semiconductor as Photocatalyst: Property, Principle, Kinetic Analysis, and Photocatalytic Activity,” *Catalysts*, vol. 13, no. 2, p. 232, Jan. 2023, doi: 10.3390/catal13020232.

[48] A. Mohamed *et al.*, “Rapid photocatalytic degradation of phenol from water using composite nanofibers under UV,” *Environ Sci Eur*, vol. 32, no. 1, p. 160, Dec. 2020, doi: 10.1186/s12302-020-00436-0.

[49] J. Z. Bloh, “A Holistic Approach to Model the Kinetics of Photocatalytic Reactions,” *Front Chem*, vol. 7, Mar. 2019, doi: 10.3389/fchem.2019.00128.

[50] J. M. Doña *et al.*, “The effect of dosage on the photocatalytic degradation of organic pollutants,” *Research on Chemical Intermediates*, vol. 33, no. 3–5, pp. 351–358, Mar. 2007, doi: 10.1163/156856707779238676.

[51] L. Derikvand and N. Tahmasebi, “Synthesis and photocatalytic performance of Bi2WO6/BiOX (X=Cl, Br, I) composites for RhB degradation under visible light,” *Korean J Chem Eng*, vol. 38, no. 1, pp. 163–169, 2021, doi: 10.1007/s11814-020-0687-y.

[52] M. F. Hanafi and N. Sapawe, “Effect of pH on the photocatalytic degradation of remazol brilliant blue dye using zirconia catalyst,” *Mater Today Proc*, vol. 31, pp. 260–262, 2020, doi: 10.1016/j.matpr.2020.05.746.

[53] Y. Guo, C. Zhou, L. Fang, Z. Liu, W. Li, and M. Yang, “Effect of pH on the Catalytic Degradation of Rhodamine B by Synthesized CDs/g-C $_3$ N $_4$ /Cu $_x$ O Composites,” *ACS Omega*, vol. 6, no. 12, pp. 8119–8130, Mar. 2021, doi: 10.1021/acsomega.0c05915.

[54] Y.-W. Chen and Y.-H. Hsu, “Effects of Reaction Temperature on the Photocatalytic Activity of TiO2 with Pd and Cu Cocatalysts,” *Catalysts*, vol. 11, no. 8, p. 966, Aug. 2021, doi: 10.3390/catal11080966.

[55] N. A. M. Barakat, M. A. Kanjwal, I. S. Chronakis, and H. Y. Kim, “Influence of temperature on the photodegradation process using Ag-doped TiO2 nanostructures: Negative impact with the nanofibers,” *J Mol Catal A Chem*, vol. 366, pp. 333–340, Jan. 2013, doi: 10.1016/j.molcata.2012.10.012.

[56] Y. Zheng, S. Wang, M. Shu, Y. Wang, and D. Cao, “Effective BiOCl Electrons Collector for Enhancing Photocarrier Separation of Bi2WO6/BiOCl Composite,” *Chemistry an international journal*, vol. 4, no. 3, pp. 765–775, 2022, doi: 10.3390/chemistry4030054.

[57] A. M. Ganose, M. Cuff, K. T. Butler, A. Walsh, and D. O. Scanlon, “Interplay of Orbital and Relativistic Effects in Bismuth Oxyhalides: BiOF, BiOCl, BiOBr, and BiOI,” *Chemistry of Materials*, vol. 28, no. 7, pp. 1980–1984, Apr. 2016, doi: 10.1021/acs.chemmater.6b00349.

[58] Z. Liang, C. Zhou, J. Yang, Q. Mo, Y. Zhang, and Y. Tang, “Visible light responsive Bi2WO6/BiOCl heterojunction with enhanced photocatalytic activity for degradation of tetracycline and rohdamine B,” *Inorg Chem Commun*, vol. 93, pp. 136–139, 2018, doi: 10.1016/j.inoche.2018.05.022.

[59] M. Xu *et al.*, “Efficient degradation of pollutants by Bi2WO6/BiOCl heterojunction activated peroxymonosulfate: Performance and mechanism,” *J Environ Chem Eng*, vol. 12, no. 2, p. 112156, Apr. 2024, doi: 10.1016/j.jece.2024.112156.

[60] J. Wang *et al.*, “Constructing of ultrathin Bi2WO6/BiOCl nanosheets with oxygen vacancies for photocatalytic oxidation of cyclohexane with air in solvent-free,” *Appl Surf Sci*, vol. 584, p. 152606, May 2022, doi: 10.1016/j.apsusc.2022.152606.

[61] M. Guo *et al.*, “Bi2WO6–BiOCl heterostructure with enhanced photocatalytic activity for efficient degradation of oxytetracycline,” *Sci Rep*, vol. 10, no. 1, p. 18401, Oct. 2020, doi: 10.1038/s41598-020-75003-x.

[62] W. Yang, B. Ma, W. Wang, Y. Wen, D. Zeng, and B. Shan, “Enhanced photosensitized activity of a BiOCl–Bi2WO6 heterojunction by effective interfacial charge transfer,” *Physical Chemistry Chemical Physics*, vol. 15, no. 44, p. 19387, 2013, doi: 10.1039/c3cp53628a.

[63] Z. K. Cui, J. Q. Zhou, D. W. Zeng, J. L. Zhang, W. J. Fa, and Z. Zheng, “From BiOCl to Bi_2WO_6 in Bi–W–Cl–O solvothermal system: phase-morphology evolution and photocatalytic performance,” *Materials Technology*, vol. 30, no. 1, pp. 23–27, Jan. 2015, doi: 10.1179/1753555714Y.0000000196.

[64] N. A. Dhas, A. Ekhtiarzadeh, and K. S. Suslick, “Sonochemical Preparation of Supported Hydrodesulfurization Catalysts,” *J Am Chem Soc*, vol. 123, no. 34, pp. 8310–8316, Aug. 2001, doi: 10.1021/ja010516y.

[65] S. Zhu, C. Yang, F. Li, T. Li, M. Zhang, and W. Cao, “Improved photocatalytic Bi2WO6/BiOCl heterojunctions: One-step synthesis via an ionic-liquid assisted ultrasonic method and first-principles calculations,” *Molecular Catalysis*, vol. 435, pp. 33–48, Jul. 2017, doi: 10.1016/j.mcat.2017.03.016.

[66] J. Chen *et al.*, “Preparation of BiOCl/Bi2WO6 Photocatalyst for Efficient Fixation on Cotton Fabric: Applications in UV Shielding and Self-Cleaning Performances,” *Materials*, vol. 14, no. 22, p. 7002, Nov. 2021, doi: 10.3390/ma14227002.

[67] Z. Liang, C. Zhou, J. Yang, Q. Mo, Y. Zhang, and Y. Tang, “Visible light responsive Bi 2 WO 6 /BiOCl heterojunction with enhanced photocatalytic activity for degradation of tetracycline and rohdamine B,” *Inorg Chem Commun*, vol. 93, pp. 136–139, Jul. 2018, doi: 10.1016/j.inoche.2018.05.022.

[68] Y. Zhang, Y. Ma, L. Wang, Q. Sun, F. Zhang, and J. Shi, “Facile one-step hydrothermal synthesis of noble-metal-free hetero-structural ternary composites and their application in photocatalytic water purification,” *RSC Adv*, vol. 7, no. 80, pp. 50701–50712, 2017, doi: 10.1039/C7RA10732C.

[69] J. Nie, J. Schneider, F. Sieland, L. Zhou, S. Xia, and D. W. Bahnemann, “New insights into the surface plasmon resonance (SPR) driven photocatalytic H_2 production of Au–TiO_2,” *RSC Adv*, vol. 8, no. 46, pp. 25881–25887, 2018, doi: 10.1039/C8RA05450A.

[70] W. Hou and S. B. Cronin, “A Review of Surface Plasmon Resonance-Enhanced Photocatalysis,” *Adv Funct Mater*, vol. 23, no. 13, pp. 1612–1619, Apr. 2013, doi: 10.1002/adfm.201202148.

[71] M. Lemos de Souza, D. Pereira dos Santos, and P. Corio, “Localized surface plasmon resonance enhanced photocatalysis: an experimental and theoretical mechanistic investigation,” *RSC Adv*, vol. 8, no. 50, pp. 28753–28762, 2018, doi: 10.1039/C8RA03919D.

[72] Z. Chen, Y. Lu, Q. Zhang, D. Zhang, S. Li, and Q. Liu, “Electrochemistry Coupling Localized Surface Plasmon Resonance for Biochemical Detection,” 2022, pp. 15–35. doi: 10.1007/978-1-0716-1803-5_2.

[73] W. M. Haynes, D. R. Lide, and T. J. Bruno, Eds., *CRC Handbook of Chemistry and Physics*. CRC Press, 2016. doi: 10.1201/9781315380476.

[74] S. Das, R. Devireddy, and M. R. Gartia, “Surface Plasmon Resonance (SPR) Sensor for Cancer Biomarker Detection,” *Biosensors (Basel)*, vol. 13, no. 3, p. 396, Mar. 2023, doi: 10.3390/bios13030396.

[75] Y. Jiao, A. Hellman, Y. Fang, S. Gao, and M. Käll, “Schottky barrier formation and band bending revealed by first- principles calculations,” *Sci Rep*, vol. 5, no. 1, p. 11374, Jun. 2015, doi: 10.1038/srep11374.

[76] C. Buzea and I. Pacheco, “Gold and silver nanoparticles: Properties and toxicity,” in *Gold and Silver Nanoparticles*, Elsevier, 2023, pp. 59–82. doi: 10.1016/B978-0-323-99454-5.00007-X.

[77] K. Kim, J. Oh, T. W. Kim, J. H. Park, J. W. Han, and Y.-W. Suh, “Different catalytic behaviors of Pd and Pt metals in decalin dehydrogenation to naphthalene,” *Catal Sci Technol*, vol. 7, no. 17, pp. 3728–3735, 2017, doi: 10.1039/C7CY00569E.

[78] Z. Li and X. Meng, “Recent development on palladium enhanced photocatalytic activity: A review,” *J Alloys Compd*, vol. 830, p. 154669, Jul. 2020, doi: 10.1016/j.jallcom.2020.154669.

[79] H. Wang, B. Shi, Y. Liu, J. Guo, N. Chang, and X. Zhao, “Construction of Ag/Bi2WO6/BiOCl with enhanced photocatalytic performance for efficient degradation of organic pollutant,” *Inorg Chem Commun*, vol. 153, p. 110816, Jul. 2023, doi: 10.1016/j.inoche.2023.110816.

[80] X. Meng, Z. Li, and Z. Zhang, “Highly efficient degradation of phenol over a Pd-BiOBr Mott–Schottky plasmonic photocatalyst,” *Mater Res Bull*, vol. 99, pp. 471–478, Mar. 2018, doi: 10.1016/j.materresbull.2017.11.045.

[81] J. Yang *et al.*, “A compact Z-scheme heterojunction of BiOCl/Bi2WO6 for efficiently photocatalytic degradation of gaseous toluene,” *J Colloid Interface Sci*, vol. 631, pp. 44–54, Feb. 2023, doi: 10.1016/j.jcis.2022.11.023.

[82] M. Guo *et al.*, “Bi2WO6–BiOCl heterostructure with enhanced photocatalytic activity for efficient degradation of oxytetracycline,” *Sci Rep*, vol. 10, no. 1, p. 18401, Oct. 2020, doi: 10.1038/s41598-020-75003-x.

[83] B. Yao *et al.*, “Cost-effective Bi2WO6 for efficient degradation of rhodamine B and tetracycline,” *Journal of Materials Science: Materials in Electronics*, vol. 34, no. 4, p. 246, Feb. 2023, doi: 10.1007/s10854-022-09654-z.

[84] X. Meng, Z. Li, and Z. Zhang, “Pd-nanoparticle-decorated peanut-shaped BiVO4 with improved visible light-driven photocatalytic activity comparable to that of TiO2 under UV light,” *J Catal*, vol. 356, pp. 53–64, Dec. 2017, doi: 10.1016/j.jcat.2017.09.005.

[85] Z. Lu *et al.*, “Selective photodegradation of 2-mercaptobenzothiazole by a novel imprinted CoFe $_2$ O $_4$ /MWCNTs photocatalyst,” *RSC Adv*, vol. 5, no. 59, pp. 47820–47829, 2015, doi: 10.1039/C5RA08795C.

[86] Z. Wang and E. Hisahiro, “Recent trends in phenol synthesis by photocatalytic oxidation of benzene,” *Dalton Transactions*, vol. 52, no. 28, pp. 9525–9540, 2023, doi: 10.1039/D3DT01360J.

[87] A. A. Dubale *et al.*, “A highly stable metal–organic framework derived phosphorus doped carbon/Cu $_2$ O structure for efficient photocatalytic phenol degradation and hydrogen production,” *J Mater Chem A Mater*, vol. 7, no. 11, pp. 6062–6079, 2019, doi: 10.1039/C8TA12544A.

[88] P. O. Oladoye, T. O. Ajiboye, E. O. Omotola, and O. J. Oyewola, “Methylene blue dye: Toxicity and potential elimination technology from wastewater,” *Results in Engineering*, vol. 16, p. 100678, Dec. 2022, doi: 10.1016/j.rineng.2022.100678.

[89] H. Jiang, Y. Li, X. Wang, and X. Hong, “Construction of a hydrangea-like Bi $_2$ WO $_6$ /BiOCl composite as a high-performance photocatalyst,” *New Journal of Chemistry*, vol. 46, no. 6, pp. 2627–2634, 2022, doi: 10.1039/D1NJ05409K.

[90] J. Chen *et al.*, “Preparation of BiOCl/Bi2WO6 Photocatalyst for Efficient Fixation on Cotton Fabric: Applications in UV Shielding and Self-Cleaning Performances,” *Materials*, vol. 14, no. 22, p. 7002, Nov. 2021, doi: 10.3390/ma14227002.

[91] A. A. Oyekanmi, A. Ahmad, K. Hossain, and M. Rafatullah, “Adsorption of Rhodamine B dye from aqueous solution onto acid treated banana peel: Response surface methodology, kinetics and isotherm studies,” *PLoS One*, vol. 14, no. 5, p. e0216878, May 2019, doi: 10.1371/journal.pone.0216878.

[92] S. Khanam and S. K. Rout, “Enhanced Photocatalytic Oxidation of RhB and MB Using Plasmonic Performance of Ag Deposited on Bi2WO6,” *Chemistry (Easton)*, vol. 4, no. 2, pp. 272–296, Apr. 2022, doi: 10.3390/chemistry4020022.

[93] M. Utami, S. Wang, F. I. Fajarwati, S. N. Salsabilla, T. A. Dewi, and M. Fitri, “Enhanced Photodegradation of Rhodamine B Using Visible-Light Sensitive N-TiO2/rGO

Composite," *Crystals (Basel)*, vol. 13, no. 4, p. 588, Mar. 2023, doi: 10.3390/cryst13040588.

Chapter 4: Palladium Modified Bi_2WO_6/BiOCl Composite Heterojunctions for Enhanced Water Treatment

Abstract

As one of the preeminent advanced oxidation processes (AOPs), photocatalysis offers an effective means of decontaminating a wide array of organic pollutants by generating highly oxidative species under illumination. This work explores the synthesis and performance of a novel Pd-Bi_2WO_6/BiOCl heterojunction photocatalyst for the visible-light-driven degradation of RhB dye. The as-prepared samples were assessed through x-ray diffraction (XRD), x-ray photoelectron spectroscopy (XPS), scanning electron microscopy (SEM), UV-visible diffuse reflectance spectroscopy (UV-vis DRS), and Brunauer-Emmett-Teller (BET) analysis. It was determined that samples prepared with a Pd content of 0.5 wt% exhibited the most impressive degradation of RhB under visible light conditions. This represents an enhancement in the photocatalytic activity of 25.45% over the previously optimized Bi_2WO_6/BiOCl precursor. The improved photoactivity can be attributed to a significantly reduced band gap (E_g), a Pd-induced surface plasmon resonance effect (SPR), and lower charge carrier recombination. It was discovered through quenching experiments that the dominant oxidative species responsible for Pd-Bi_2WO_6/BiOCl degradation of RhB are holes (h^+). Whereas hydroxyl radicals (•OH) played a smaller role and superoxide radicals ($O_2^{\bullet-}$) had a negligible impact. Moreover, it was revealed through UV-visible spectrophotometry that the major degradation mechanism of RhB followed the N-de-ethylation pathway, suggesting that Pd-Bi_2WO_6/BiOCl can effectively decontaminate RhB and its various intermediate products. Finally, the effects of several other parameters, including operating temperature, initial solution pH, catalyst dosage, RhB concentration, and catalyst stability, were examined and reported.

4.1 Introduction

In recent times, there has been a growing concern over the amount of toxic wastewater effluent present in the environment. Harmful pollutants ranging from organic pollutants to heavy metals have seen higher levels of detection, posing a danger to the well-being of society and the overall environment. To mitigate the threat posed by toxic water effluent, several water treatment strategies, including sedimentation, filtration, and membrane separation, have been developed. While these classical methods have enjoyed a certain level of success, they mainly rely on phase transfer, rendering them incapable of achieving complete degradation of pollutants [9]. Chemical and biological means of water treatment have also faced drawbacks, including the creation of harmful secondary by-products and high operation costs [9], [10]. As a result, researchers have sought to develop advanced oxidation processes (AOPs) to provide safe, complete, and cost-effective water treatment.

One of these methods, heterogeneous photocatalysis, has attracted attention for its potential application in the treatment of organic pollutants. Photocatalysts are semiconductors that are activated upon the absorption of light with energy equal to or greater than their band gap (E_g). Once activated, electrons (e^-) in the valence band (VB) are excited to the conduction band (CB), leaving positively charged holes (h^+) in their absence. The photogenerated charge carrier species (e^- and h^+) migrate to the surface of the catalyst to participate in redox reactions, degrading the target molecules into safe and innocuous final products [11]. When compared to existing technologies, photocatalysis provides complete treatment without generating any secondary by-products. Moreover, due to semiconductors strictly requiring photonic activation, photocatalysis can be operated under ambient conditions, making it more environmentally and cost-friendly [8], [11]. Despite its promising attributes, several deficiencies exist that hinder the wider industrial application of this method. These include high e^-/h^+ recombination rates and limited visible-light responsiveness resulting from wide band gap materials. Therefore, modern research in this field focuses on the development and preparation of narrow E_g catalysts with low-charge carrier recombination to provide effective, visible-light-driven treatment of aqueous organic pollutants.

Bi_2WO_6 has been the subject of recent attention in the field of photocatalysis due to its excellent conductive properties under visible light. As is the case with most Aurivillius compounds, Bi_2WO_6 consists of a characteristic perovskite structure with a narrow band gap of 2.6-2.9 eV [12]. Its distinctive orthorhombic symmetry is formed by stacking octahedral $[WO_6]$ layers with alternating $[Bi_2O_2]$ units. This induces an electric field parallel to the [001] crystal plane, promoting effective charge transport and adsorption of target molecules on the catalytic surface [12], [44]. Nonetheless, bismuth tungstate is limited by high-charge recombination, curtailing its widespread use for aqueous photocatalytic systems.

A method being used to enhance the performance of bismuth tungstate is the formation of heterojunction composites. This technique involves compositing a high-band gap structure with a low-band gap structure. This creates a heterostructure in which an interface is formed between the two morphologically dissimilar catalysts [9], [22]. A compound that has recently shown promise for being composited with Bi_2WO_6 is bismuth oxychloride (BiOCl). Belonging to the bismuth oxyhalides (BiOX), BiOCl possesses a highly crystalline structure made of repeating units of [Cl-Bi-O-Bi-Cl] alternatively stacked with four surrounding O and Cl atoms, creating an asymmetric conical-decahedral structure [56]. This arrangement creates a large region in which atoms and orbitals can be polarized, creating an electrostatic field along the [001] plane. This promotes excellent charge transfer and minimizes electron-hole recombination. Additionally, BiOCl's wide band gap of 3.2 eV makes it a suitable candidate to pair with Bi_2WO_6 [17]. Several studies conducted on Bi_2WO_6/BiOCl heterojunctions have reported considerable visible-light-driven degradation of organic pollutants.

Recently, noble-metal deposition has been pursued to enhance the visible light activity of heterojunction photocatalysts. The introduction of noble metals, including Au, Ag, Pt, and Pd onto the surface of photocatalysts has two main merits: the formation of a Schottky junction and the surface plasmon resonance (SPR) effect [70], [71]. When a semiconductor comes into contact with a heavy metal, the resulting energy difference between the conduction band of the semiconductor and the Fermi level of the metal creates a space charge region known as the Schottky junction. As free electrons in the space-charge region approach the metal-semiconductor interface, their overall energy increases, resulting in the formation of internal electric fields. This helps to increase charge transfer and reduce electron-hole recombination [71]. Additionally, when noble metals are added to semiconductor photocatalysts, it can result in the SPR effect. This is a result of surface NPs forming localized surface plasmons. As a result, when photonic energy excites NP electrons, it causes an oscillation of electron density, which creates surface plasmons. Due to the minute size of the metal nanoparticles, the oscillation will resemble the frequency of the incoming light, creating electromagnetic fields on the surface of the NPs. This phenomenon is useful as it broadens the absorption spectra of the catalyst, leading to an effective visible-light response [72], [75].

When selecting a suitable metal for modifying a heterojunction, several electronic properties should be considered. Of the four major heavy metals mentioned, Ag and Pd exhibit the lowest work functions (ϕ), making them more likely to lose their electrons [70]. This allows them to form viable Schottky junctions, as effective space-charge barriers are constructed with low ϕ metals. Limited work has been published on the addition of noble metals to Bi_2WO_6/BiOCl. A sole study conducted by Wang et al. explored the application of Ag-Bi_2WO_6/BiOCl for the degradation of organic pollutants [80]. The introduction of Pd NPs to Bi_2WO_6/BiOCl has yet to be explored. Owing to its good chemical stability, tendency to induce the SPR effect, and effective charge trapping properties, palladium should be considered in the construction of plasmonic enhanced-Bi_2WO_6/BiOCl heterojunctions.

In this work, hydrothermally synthesized Bi_2WO_6/BiOCl composites underwent a photoreduction technique to fabricate novel Pd-Bi_2WO_6/BiOCl heterojunction catalysts. The performance of the catalysts was assessed through the degradation of the textile dye, Rhodamine B (RhB), wherein the effects of system temperature, pH, catalyst dosage, and initial pollutant concentration were evaluated. Furthermore, the stability of Pd-Bi_2WO_6/BiOCl was demonstrated through recyclability testing. A possible catalyst mechanism and RhB degradation pathway were also prepared through the use of UV-vis spectra.

4.2 Experimental

4.2.1 Preparation of Pd-Bi_2WO_6/BiOCl

All materials were supplied from Sigma Aldrich in their reagent grade without further modification. Bi_2WO_6/BiOCl was prepared by a typical hydrothermal method [66], [67], [68]. Initially, 5 mmol of $Bi(NO_3)_3 \cdot 5H_2O$ (reagent grade, 98%) was mixed into 40 mL of distilled and deionized water (DDW) and stirred for a period of 30 minutes at ambient conditions. 2.5 mmol $Na_2WO_4 \cdot 2H_2O$ (ACS reagent grade, ≥ 99%) was then added to the solution under magnetic stirring for 30 minutes. This was followed by the addition of 0.75 mmol of NaCl (ACS reagent grade, ≥ 99%) into 20 mL of DDW and mixing for 20 minutes. The NaCl solution was added to the combined initial solution in a dropwise manner over the course of 60 minutes under constant magnetic stirring. The combined mixture was subsequently transferred into a 100-mL Teflon-lined stainless-steel autoclave (Parr Instrument Company) and placed in a mechanical heater for a duration of 12 hours at 135°C. After cooling to room temperature, the autoclave was recovered, and white precipitates were collected and separated by centrifugation. The samples were washed three times with DDW and ethanol to remove ionic species and impurities from the final product. The wet samples were dried overnight at 60°C to obtain solid Bi_2WO_6/BiOCl.

Pd-Bi_2WO_6/BiOCl samples were prepared by a simple photoreduction technique. A well-dispersed $PdCl_2$ suspension was achieved through ultra-sonication for a period of 30 minutes. Next, 1 g of the as-prepared Bi_2WO_6/BiOCl sample was uniformly dispersed into 50 mL of DDW under constant magnetic stirring for 30 minutes. This was followed by the addition of a designated amount of $PdCl_2$ suspension to the Bi_2WO_6/BiOCl suspension. The combined mixture was agitated in the dark for a period of 15 minutes before being illuminated with a 300 W tungsten halogen lamp (Ushio, USA) for 1 hour. The samples were collected via centrifugation and washed three times with DDW to attain products of high purity. The samples were dried overnight at 60°C to obtain powered catalysts. Pd-Bi_2WO_6/BiOCl composites were prepared with Pd contents of 0.3, 0.4, 0.5, 0.6, 0.7, 0.8, and 1.0 wt% to assess the effect of Pd loading.

4.2.2 Characterization

X-ray diffraction (XRD) was used to assess the crystal structure of the prepared samples by using a Rigaku Ultima IV XRD with Cu K(α) radiation ($\lambda = 0.15418$ nm) operating at 40 mA and 40 kV from 10 to 80° (2θ). X-ray photoelectron spectroscopy (XPS) was used to detect the elemental composition and chemical states present on the surface of the samples using AlK_α radiation at 1486.69 eV (150 W, 10 mA), a charge neutralizer, and a delay-line detector (DLD) consisting of three multi-channel plates. Binding energies were referenced according to the C1s peak (adventitious carbon, Csp^3) at 285 eV. The surface morphology of the samples was viewed through field-emission scanning electron microscopy (FE-SEM, JEOL JSM-7500F). The optical properties of the samples were evaluated by ultraviolet-visible diffuse reflectance spectroscopy (UV-vis DRS) using a Thermo Evolution 300 spectrophotometer equipped with a Praying Mantis accessory

(Harrick Scientific, USA). The pore volumes of the samples were found using N_2 adsorption isotherms at 77 K using Tristar II Plus (Micromeritics). The Brunauer-Emmett-Teller (BET) surface area of the samples was calculated by multi-point estimation.

4.2.3 Photocatalytic Activity Testing

The photocatalytic activity of the samples was assessed by monitoring the degradation of RhB in an aqueous solution. The photoreactor consisted of a 500-mL beaker fitted with a thermostatic cooling bath. Illumination was achieved using a 300 W tungsten halogen lamp (Ushio, USA) with a wavelength range of 310 to 800 nm. The lamp was modified using a Kenko-Zeta filter (transmittance > 90%) to block irradiation with a wavelength below 410 nm, ensuring photocatalysis would take place strictly under visible light. Each run consisted of a select concentration of 200 mL of RhB solution as the catalytic substrate. A certain amount of catalyst sample was added to the substrate mixture under constant magnetic stirring. The mixture was allowed to mix magnetically in the dark for a period of 20 minutes to allow for an adsorption-desorption equilibrium to be established between the catalyst and substrate. Once the light was turned on, the photodegradation process commenced, and 2 mL aliquots were drawn using a transfer pipette at select intervals before being centrifuged for 5 minutes at a rate of 13,300 rpm with an accuSpin Micro 17 (Fisher Scientific) centrifuge to separate the catalyst from the solution. The clear supernatant was analyzed using a UV-vis spectrophotometer (Genesys 10 UV, Thermo Scientific) with a set wavelength of 554 nm, corresponding to the characteristic absorption peak of RhB. The concentration of RhB was determined for each time interval using a calibration curve for the dye. The photodegradation rate was calculated using Equation 3-1.

To investigate the effect of operation parameters on the photodegradation process, an Evolution 300 UV-vis spectrophotometer was used to produce absorption spectra of the supernatant samples from 300 to 700 nm. This was conducted to evaluate the potential RhB degradation pathway. To assess the stability of the samples, a four-stage degradation test was performed. After each successive run, catalysts were centrifuged and recovered before being mixed with new RhB solution. Adsorption tests were also conducted during the 20-minute dark mixing period to determine the adsorption capacity of the samples. To determine the role of the main active species in the degradation process, quenching experiments were performed. Isopropanol (IPA), ethylenediaminetetraacetic acid (EDTA), and L-ascorbic acid (LAA) were used as scavengers to suppress the influence of hydroxyl radicals (•OH), holes (h^+), and superoxide radicals ($O_2^{\bullet -}$), respectively. The effect of operating parameters on the photodegradation of RhB, including catalyst dosage, pollutant concentration, initial pH, and system temperature, were also monitored.

4.3 Results and Discussion

4.3.1 XRD Analysis

The crystal structure and phase purity of the Bi_2WO_6/BiOCl and Pd-Bi_2WO_6/BiOCl samples were assessed by XRD analysis. Figure 4-1 shows the XRD patterns for Bi_2WO_6/BiOCl, 0.3% Pd-Bi_2WO_6/BiOCl, 0.5% Pd-Bi_2WO_6/BiOCl, 0.8% Pd-Bi_2WO_6/BiOCl, and 1% Pd-Bi_2WO_6/BiOCl. For Bi_2WO_6/BiOCl, the characteristic diffraction peaks closely resemble those of Bi_2WO_6/BiOCl and can be indexed according to the JCPDS card 39-0256 as 28.3°(131), 32.8°(002), 47.1°(202), 56.1°(133), 58.5°(262), 68.7°(004), 76.2°(102), and 78.4°(204). Additionally, the composite had narrow and broad peaks, indicating a high level of crystallinity. This is significant as effective photocatalysts require a high level of crystallinity to limit the number of defects that act as e^-/h^+ recombination centres [9], [56], [57].

The Pd-modified samples exhibit similar diffraction patterns as Bi_2WO_6/BiOCl, indicating that the introduction of Pd nanoparticles did not significantly alter the crystal structure of the catalyst. Moreover, when compared to a standard palladium diffraction pattern (JCPDS card 01-072-0710), the samples show no characteristic peaks at (001). This could suggest that the Pd-NPs reside on the surface of the Bi_2WO_6/BiOCl rather than being covalently anchored in the lattice structure. It is also possible that since very little Pd was deposited on the samples, the nanoparticles are too dispersed to reach the XRD detection limit, leading to poor diffraction intensity.

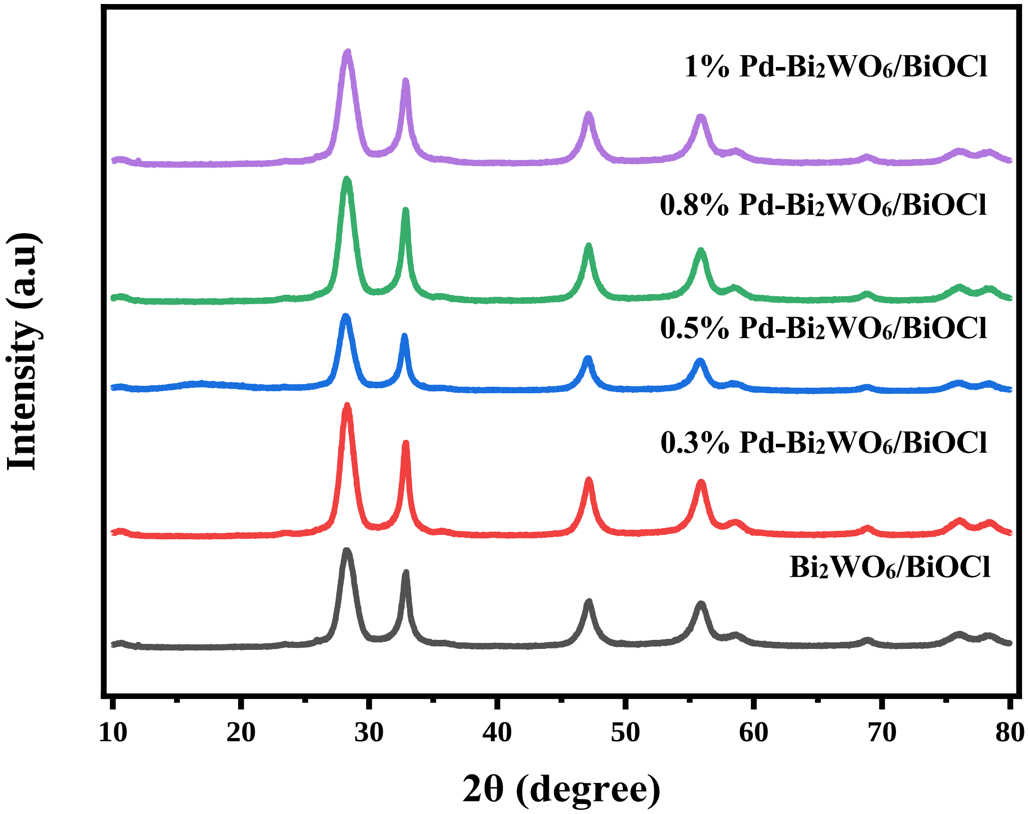

Figure 4-1: XRD patterns of Bi_2WO_6/BiOCl and Pd-Bi_2WO_6/BiOCl composite heterojunction photocatalysts.

4.3.2 XPS Analysis

The elemental composition and oxidation states of the Pd-Bi_2WO_6/BiOCl heterojunction were characterized by XPS analysis. A wide-range spectral scan of the sample revealed the elemental constituents to be Bi, O, W, Cl, Pd, and C. Moreover, individual high-resolution scans were recorded for the individual elements (Figures 4-3 to 4-6). The presence of the C1s peak at 285 eV is attributed to adventitious carbon (Csp^3), which is formed from a small layer of carbon residue deposited on the samples from the atmosphere and is used to calibrate the binding energies [98].

Figure 4-2 shows the broad spectral scan of Pd-Bi_2WO_6/BiOCl from 0 to 1200 eV. All constituent elements are present in their oxidation states (O1s, Pd3d, O1s, C1s, Bi4f, and W4f). This, along with the XRD results shown in Figure 4-1, confirms the successful formation of the catalyst sample. Moreover, there are no impurity peaks present on the survey, suggesting that all of the major constituents of Pd-Bi_2WO_6/BiOCl are present without external contamination.

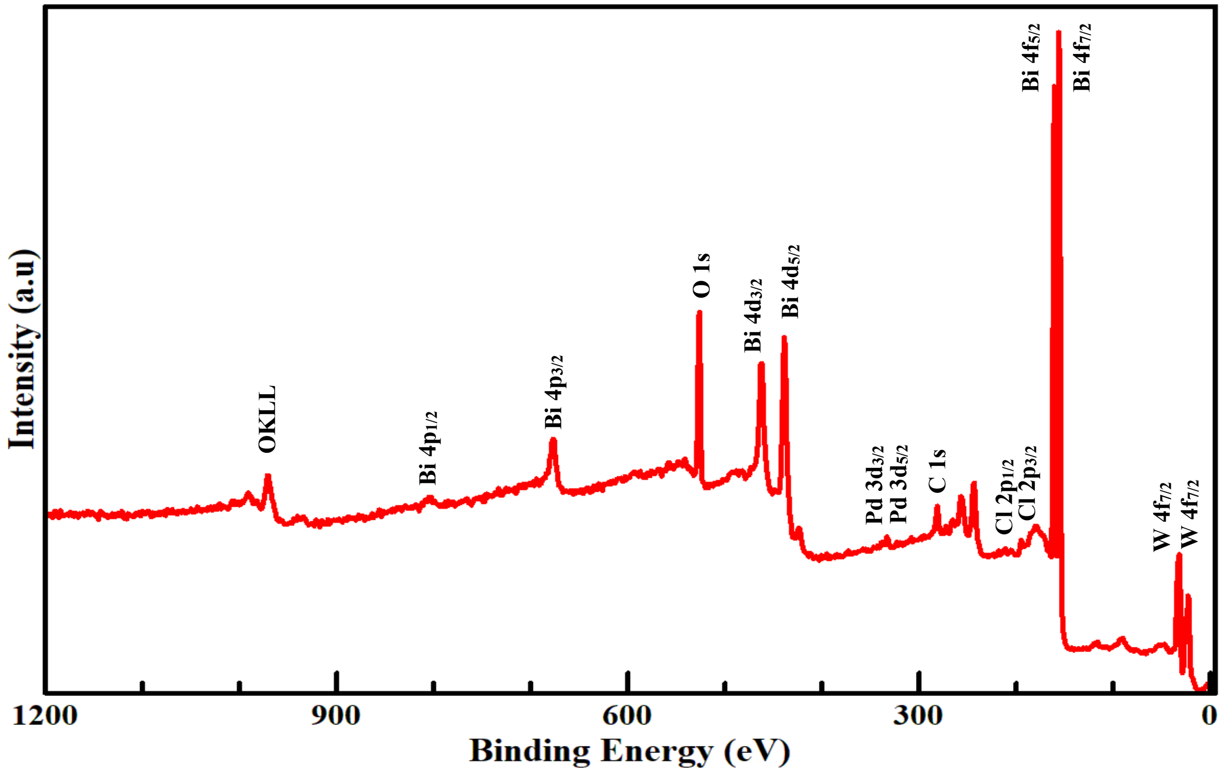

Figure 4-2: XPS survey scan for 0.5% Pd-Bi_2WO_6/BiOCl composite photocatalyst.

Figure 4-3 shows the high-resolution XPS scan for the bismuth (Bi 4f). Through spin-orbit splitting, it can be seen that Bi 4f consists of two peaks located at 162.3 eV and 155.8 eV, corresponding to the binding energies of Bi 4f$_{5/2}$ and Bi 4f$_{7/2}$. These peaks are attributed to the trivalent state of bismuth (Bi^{3+}), present in both Bi_2WO_6 and BiOCl. When compared to the literature data for pure Bi_2WO_6 samples, it is noted that Bi $4f_{5/2}$ and Bi $4f_{7/2}$ exhibit a small shift of 1.8 and 3 eV towards the lower energy region. This is caused by the low-energy Bi-O bond present in BiOCl, indicating an interaction between the parent compounds [99], [100]

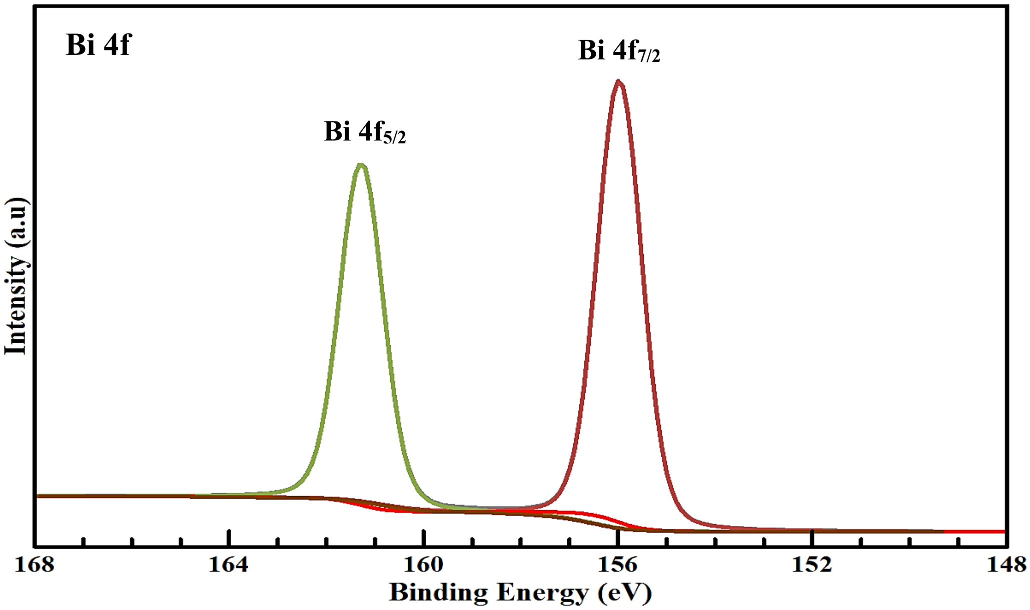

Figure 4-3: High resolution XPS survey of Bi 4f present in 0.5% Pd-Bi_2WO_6/BiOCl composite photocatalyst.

Figure 4-4 below shows that the W 4f spectrum is split into two characteristic peaks at 34.3 eV and 32.8 eV, corresponding to the binding energies of W $4f_{5/2}$ and W $4f_{7/2}$, respectively. This pattern is attributed to the W^{6+} ions present in Bi_2WO_6. It is important to mention that the W 4f spectra in Figure 4-4 remain relatively unchanged as compared to that of Bi_2WO_6. This indicates that the octahedral [WO_6] structure of Bi_2WO_6 is unaltered by BiOCl surface modification and thus does not lose its desirable structure-property relationships during the construction of the heterojunction [101].

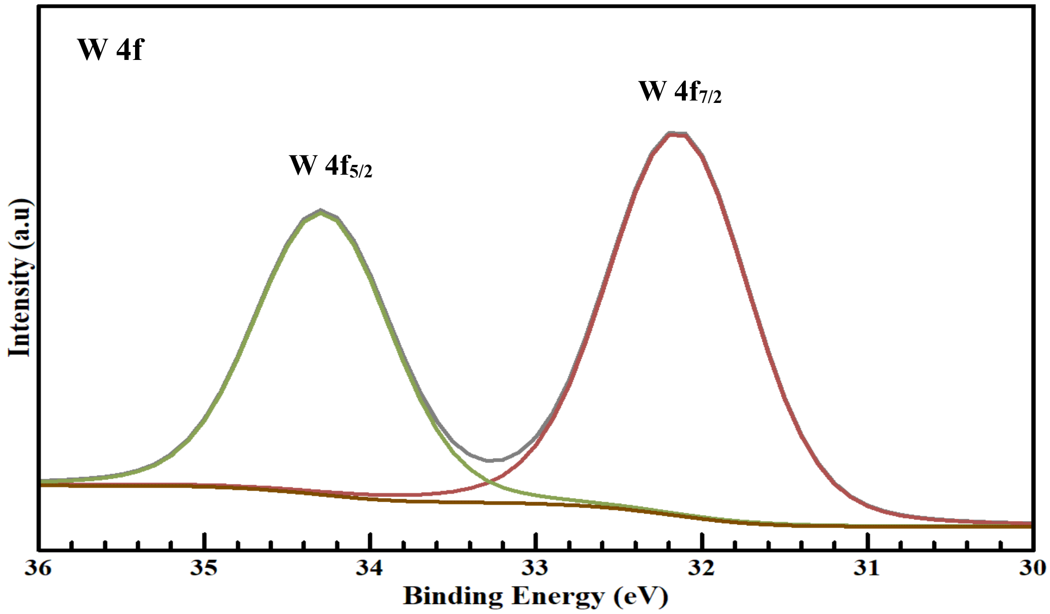

Figure 4-4: High resolution XPS survey of W 4f present in 0.5% Pd-Bi_2WO_6/BiOCl composite photocatalyst.

As shown in Figure 4-5, the O1s spectrum can be deconvoluted into five characteristic peaks, corresponding to five distinct O structures in the sample. The peaks located at 527.8 eV and 527.2 eV could be attributed to the overlapping contributions of O^{2-} ions. The peak located at 527.2 eV can be attributed to the coordination of the oxygen in the Bi-O bond. Whereas the 527.8 eV is a result of the higher energy bond of W-O. The lowest energy peak at 526.7 eV may be ascribed to the hydroxyl group (-OH), however, due to the wide binding energy range of 2.5 eV, it could be a combination of O^{2-} and absorbed H_2O molecules. This finding is significant, as these species act as charge traps for photogenerated e^- and h^+, reducing the overall recombination rate. Furthermore, surface OH groups and H_2O can react with h^+ to produce •OH, which has a high oxidative capacity in the photodegradation process [102].

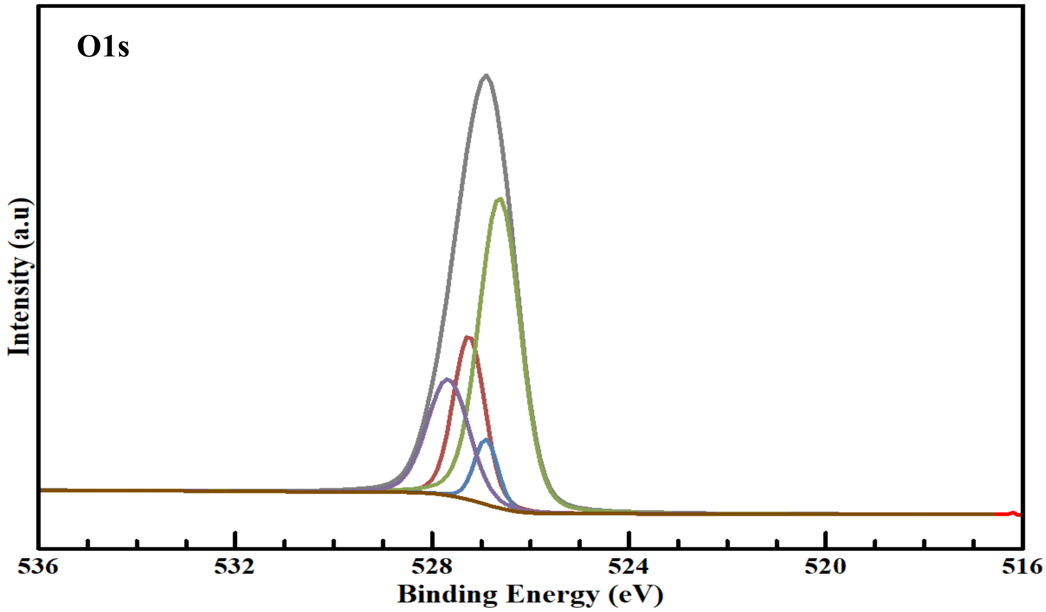

Figure 4-5: High resolution XPS survey of O 1s present in 0.5% Pd-Bi_2WO_6/BiOCl composite photocatalyst.

The chemical states of the photodeposited palladium on Bi_2WO_6/BiOCl were determined using Figure 4-6 below. The XPS spectrum shows that Pd exhibits a set of spin-orbit doublets in the form of Pd 3d possessing binding energies of 338.5 eV (Pd $3d_{3/2}$) and 333.2 eV (Pd $3d_{5/2}$). The separation energy between these two states is 5.3 eV, which is in line with previously reported data for palladium. From this finding, it can be deduced that the chemical state of palladium exists as Pd^{2+}. This is consistent with the palladium found in $PdCl_2$. Furthermore, the wide spectrum and high-resolution scans did not indicate the presence of any major peaks in the regions of 342.9 eV and 337.5 eV. This suggests that no Pd was detected in the form of Pd^0. The wide spectral scan shows two Cl 2p peaks corresponding to 199.9 eV (Cl $2p_{1/2}$) and 198.2 eV (Cl $2p_{3/2}$). These indicate the presence of Cl^{-1} ions in BiOCl. This also shows that $PdCl_2$ was reduced to Pd nanoparticles during the course of the photoreduction process [100], [101].

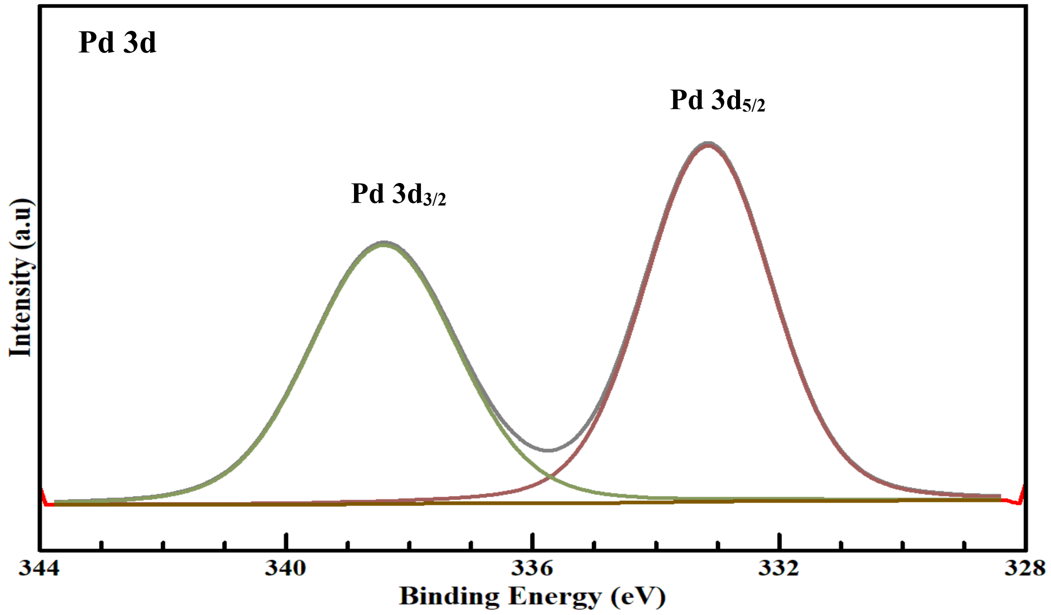

Figure 4-6: High resolution XPS survey of Pd 3d present in 0.5% Pd-Bi_2WO_6/BiOCl composite photocatalyst.

4.3.3 SEM Analysis

SEM imaging was used to observe the surface morphology of pure Bi_2WO_6/BiOCl and 0.5% Pd-Bi_2WO_6/BiOCl samples. Low- and high-magnification images are provided in Figures 4-7 to 4-8 below. Both samples were prepared under the same thermal conditions of 12 hours and 135°C. As a result, both exhibit similar microsphere structures with plate-like projections, which are hallmarks of typical hydrothermally synthesized Bi_2WO_6/BiOCl catalysts. However, the samples do display slightly varied mean diameters. Bi_2WO_6/BiOCl was found to have a mean diameter of 6.33 µm, whereas the palladium-modified sample had a larger diameter of 9.8 µm. This finding is reasonable, as it has been reported that the addition of palladium nanoparticles to the surface can promote the production of slightly larger crystallites, leading to a slight decline in the available surface area [67], [68].

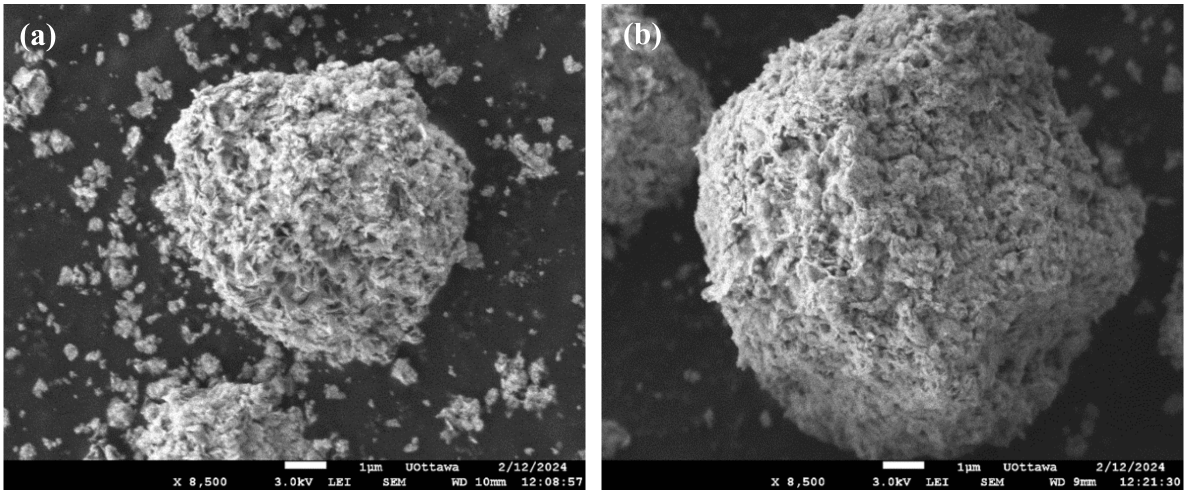

Figure 4-7: SEM Image of (a) pure Bi_2WO_6/BiOCl and (b) 0.5% Pd-Bi_2WO_6/BiOCl composite photocatalysts.

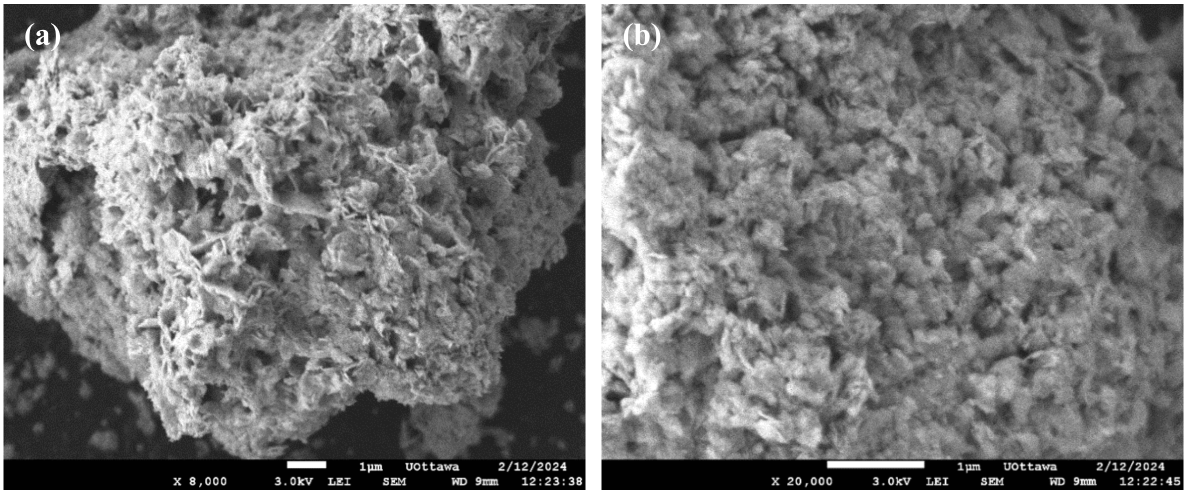

Figure 4-8: SEM Images of 0.5% Pd-Bi_2WO_6/BiOCl under (a) low magnification and (b) high magnification.

4.3.4 UV-vis Diffuse Reflectance Spectra

UV-vis DRS was used to detect the optical absorption properties of the as-prepared samples. Figure 4-9 displays the absorbance plots for Bi_2WO_6, BiOCl, Bi_2WO_6/BiOCl, and the various samples of Pd-Bi_2WO_6/BiOCl. Absorption edges were determined from Figure 4-9 and used to calculate the band gaps for each sample using the Planck relations presented in Equations 2-1 and 2.2, as summarized in Table 4-1 below. All samples exhibit a high level of absorbance in the region of 300-400 nm, indicating high responsiveness to ultraviolet light. The absorbance for each sample starts to decrease at 350 nm, which can be attributed to the band gap transition. When assessing the parent compounds, it was found that Bi_2WO_6 and BiOCl had E_g of 2.89 and 3.35 eV, respectively. This finding is consistent with previously reported band gaps for these compounds. Since BiOCl has a high band gap, it is photoactivated in the UV range. In contrast, Bi_2WO_6 is able to access a much broader portion of the spectrum due to its lower band gap, making it visible light active. When these two compounds were combined to synthesize Bi_2WO_6/BiOCl, the resulting absorbance profile revealed a band gap of 2.93 eV. This shows that the composite is visible-light-active. It should be noted, however, that the heterojunction having a slightly higher band gap than pure Bi_2WO_6, is a result of the added BiOCl nanoplates, which are mainly responsive to UV radiation. For the palladium-modified composites, there was an evident red shift in the spectra, indicating a significantly stronger absorption profile in the visible-light range. Samples synthesized with Pd content of 0.3 and 0.8 wt% Pd exhibited band gaps of 2.63 and 2.74 eV, representing a clear improvement in visible-light activation. The most impressive absorbance profile belonged to 0.5% Pd-Bi_2WO_6/BiOCl which had the widest spectral coverage and the lowest E_g of 2.54 eV. The red shift of the modified samples is due to the surface plasmon resonance effect, which imparts excellent visible light absorbance for Pd nanoparticles. Moreover, the formation of a Schottky junction between the semiconductor and metal interface allows for more visible light capture, leading to a broader profile. This finding is consistent with previously reported Pd-modified catalysts, which displayed lower band gaps and larger spectral coverage. Therefore, it can be stated that the addition of Pd NPs on the surface of Bi_2WO_6/BiOCl heterojunctions enhances the spectral coverage, thereby improving visible light responsiveness [26], [28].

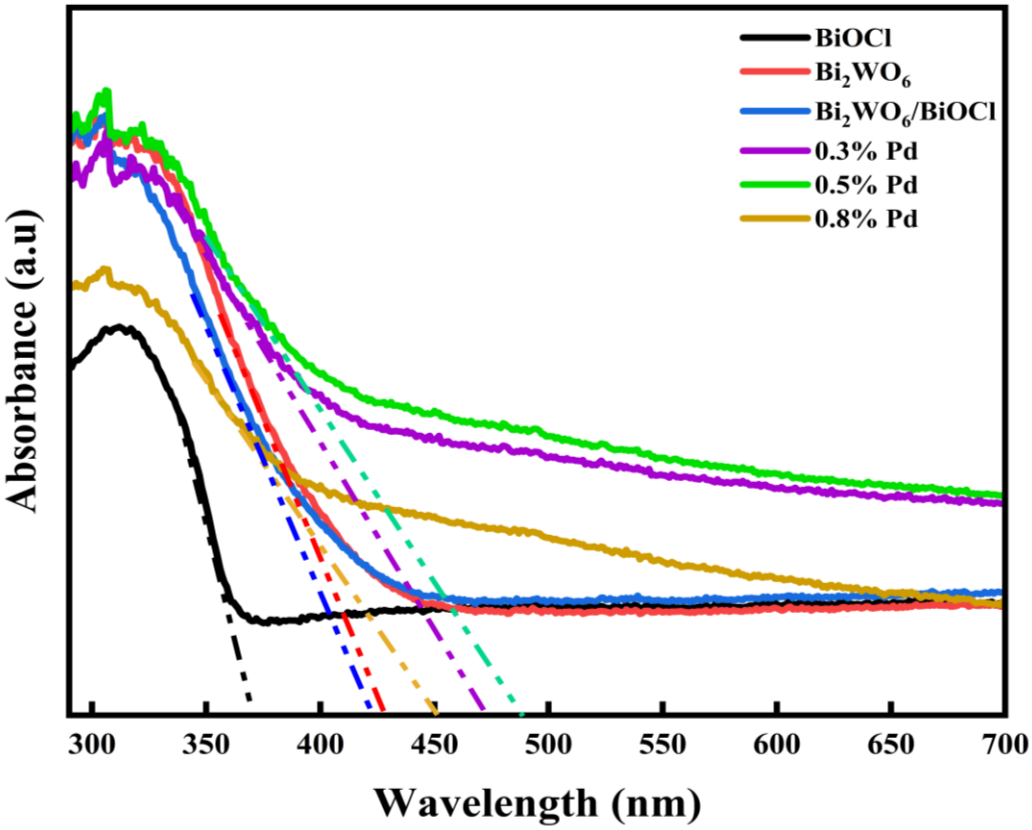

Figure 4-9: UV-vis DRS absorbance spectra of BiOCl, Bi_2WO_6/BiOCl, and Pd-Bi_2WO_6/BiOCl heterojunction photocatalysts.

Table 4-1: Estimated absorption edges and band gaps of as-prepared samples.

Photocatalyst	Absorption Edge (nm)	Band Gap (eV)
Bi_2WO_6	428.82	2.89
BiOCl	370.49	3.35
Bi_2WO_6/BiOCl	423.11	2.93
0.3% Pd-Bi_2WO_6/BiOCl	471.07	2.63
0.5% Pd-Bi_2WO_6/BiOCl	487.24	2.54
0.8% Pd-Bi_2WO_6/BiOCl	451.81	2.74

4.3.5 N_2 Sorption Isotherms

To assess the adsorption properties of the samples, N_2 sorption isotherms were measured and recorded for Bi_2WO_6, BiOCl, Bi_2WO_6/BiOCl, and 0.5% Pd-Bi_2WO_6/BiOCl at 77 K. From Figure 4-10, all four isotherms exhibit patterns consistent with type IV physisorption as per IUPAC conventions. The adsorption associated with this profile is described as proceeding via multilayer adsorption followed by capillary condensation [103].

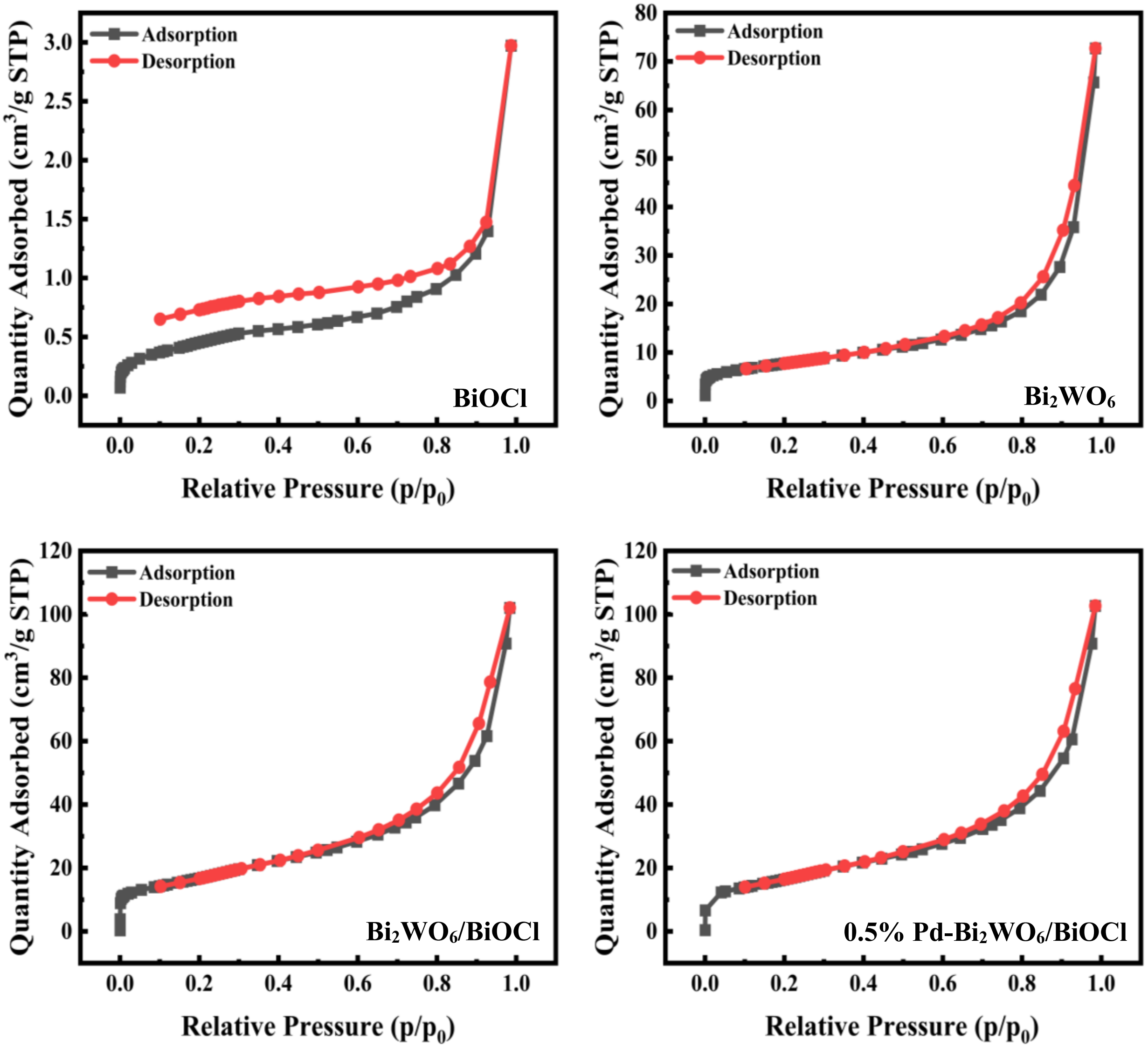

Figure 4-10: N_2 sorption isotherms for BiOCl, Bi_2WO_6, Bi_2WO_6/BiOCl, and 0.5% Pd-Bi_2WO_6/BiOCl samples (isotherm temperature: 77 K).

A distinctive feature of type IV isotherms is the presence of a hysteresis loop, associated with capillary condensation in the mesopore structure. This limits N_2 uptake in the high relative pressure range. Moreover, the initial phase of type IV isotherms resembles closely to type II behaviour and is associated with monolayer-multilayer adsorption [103]. The type of hysteresis loop in the isotherm can help to describe the thermodynamic and network effects occurring in the mesoporous structure. Typically, it is the case that the steepness of the isotherm declines from H1 to H4 types. From the adsorption isotherm prepared in Figure 4-10, it is shown that BiOCl exhibits an H3 hysteresis loop resulting from the aggregation of plate structures with slit-like pores [103], [104]. This finding is consistent with the SEM images, which revealed the plate-like morphology of this catalyst. As for the other three cases, they all presented traits of H4 hysteresis loops with a more gradual desorption slope. This is generally a hallmark of particles with narrow slit-like pores of spherical structure and is consistent with the SEM images for Bi_2WO_6, Bi_2WO_6/BiOCl, and Pd-Bi_2WO_6/BiOCl, which revealed spherical structures.

The specific BET surface areas and the pore volume of the samples were calculated from the isotherms and are presented in Table 4-2 below. BiOCl had the smallest surface area of 1.48 m^2/g, indicting a poor adsorption capacity. This is explained by the presence of plate-like morphology, which is less conducive to pollutant uptake. Bi_2WO_6 had a specific surface area of 26.08 m^2/g, which is a result of its sphere structure, resulting in better adsorptive capacity. The composite Bi_2WO_6/BiOCl samples showed a significantly greater surface area of 56.37 m^2/g, implying a very high adsorption capacity. When Pd was added to the surface of the composite, there was a similar surface area of 56.22 m^2/g. This can be accounted for by the fact that the palladium-modified samples were calcined under the same thermal conditions as the precursor composites, resulting in a similar surface area. Moreover, the Pd samples displayed a slightly greater pore volume of

0.641×10^{-3} cm^3/g compared to the bare sample, suggesting that the addition of the nanoparticle may increase the average pore volume size.

Table 4-2: BET surface area and average pore volume of BiOCl, Bi_2WO_6, Bi_2WO_6/BiOCl, and 0.5% Pd-Bi_2WO_6/BiOCl samples.

Photocatalyst	S_{BET} (m^2/g)	Pore Volume (10^{-3} cm^3/g)
BiOCl	1.480	0.108
Bi_2WO_6	26.08	1.80
Bi_2WO_6/BiOCl	56.37	0.533
0.5% Pd-Bi_2WO_6/BiOCl	56.22	0.641

4.4 Adsorption Analysis

To add further insight into the adsorption properties of the catalysts discussed in the previous section, adsorption kinetic profiles were elucidated through dark reactions. These properties are important in describing the solute uptake rate and gaining a better understanding of the adsorbate-adsorbent interactions. The adsorption equilibrium profile of a sample assesses its adsorption capacity once dynamic equilibrium is achieved. To assess the RhB adsorption capacity of the samples, equilibrium kinetic models were prepared and presented in Figures 4-11 and 4-12.

Using the slopes of the profiles shown in Figure 4-12, the sorption capacities (q_e) of BiOCl and Bi_2WO_6 were found to be 2.44 and 5.32 mg/g respectively. This clearly shows that the Bi_2WO_6 microspheres are more conducive to RhB adsorption. This finding supports the N_2 adsorption experiments, which found the surface area for Bi_2WO_6 to be much larger than that of BiOCl, explaining the greater sorption capacity for RhB. Composite Bi_2WO_6/BiOCl exhibited the most impressive uptake of RhB, with a q_e of 11.20 mg/g. This result is consistent with the BET analysis, which showed that the composite had the highest specific surface area, making it capable of adsorbing more RhB molecules. Finally, 0.5% Pd-Bi_2WO_6/BiOCl had a q_e of 10.24 mg/g. The slight decline is consistent with the trend found in the N_2 experiments, which showed a slight decrease in surface area when palladium was added. This is reasonable, as the presence of palladium nanoparticles can block binding sites on the catalytic surface, leading to less RhB adsorption. However, the difference between the bare and modified composites is minimal owing to the similar thermal conditions during their synthesis.

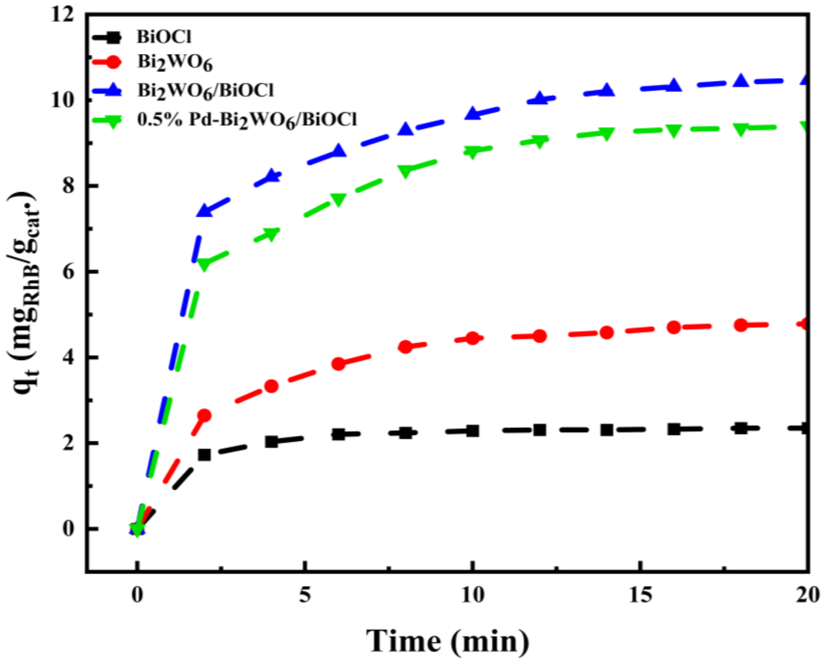

Figure 4-11: RhB adsorption isotherms at 20°C for BiOCl, Bi_2WO_6, $Bi_2WO_6/BiOCl$, and 0.5% Pd-$Bi_2WO_6/BiOCl$ samples.

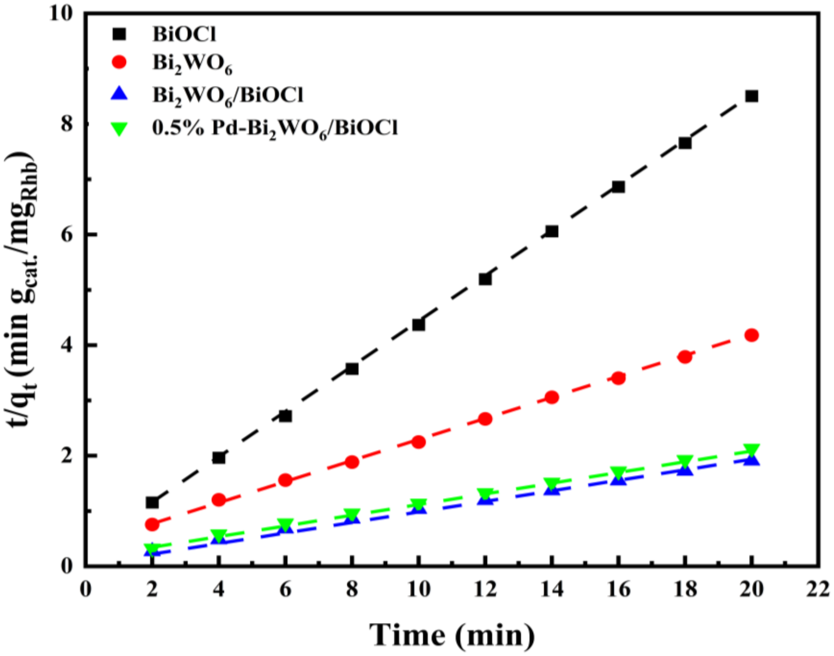

Figure 4-12: Pseudo-second-order adsorption modelling for BiOCl, Bi_2WO_6, Bi_2WO_6/BiOCl, and 0.5% Pd-Bi_2WO_6/BiOCl samples (where dashed lines represent linear regression fitting).

It is important to mention that the kinetic modelling performed to ascertain the sorption capacities for each sample was achieved by using the pseudo second-order model, shown in Equations 4-1 and 4-2 below:

$$\frac{dq_t}{dt} = k_2(q_e - q_t)^2 \tag{4-1}$$

$$\frac{t}{q_t} = \frac{1}{k_2 q_e^2} + \frac{1}{q_e} t \tag{4-2}$$

Where k_2 represents the equilibrium rate constant for the pseudo second-order adsorption ($g_{adsorbent}$/mg adsorbate^{-1}min^{-1}). The k_2 values were calculated for each sample using the linear region of the plot shown in Figure 4-12. It was found that all four data sets had R^2 greater than 0.99, confirming the appropriate model was selected. It should be noted that most photocatalytic adsorption processes exhibit this behaviour due to their rapid uptake of target pollutants on the catalytic surface.

4.5 Photocatalytic Degradation Testing

4.5.1 Effect of Pd Loading

The photocatalytic activity of samples with different Pd loading contents was evaluated via the degradation of aqueous RhB dye under visible light illumination, as shown in Figure 4-13 below. The first-order rate constant (k_{app}) and the R^2 were also collected and listed in Table 4-3.

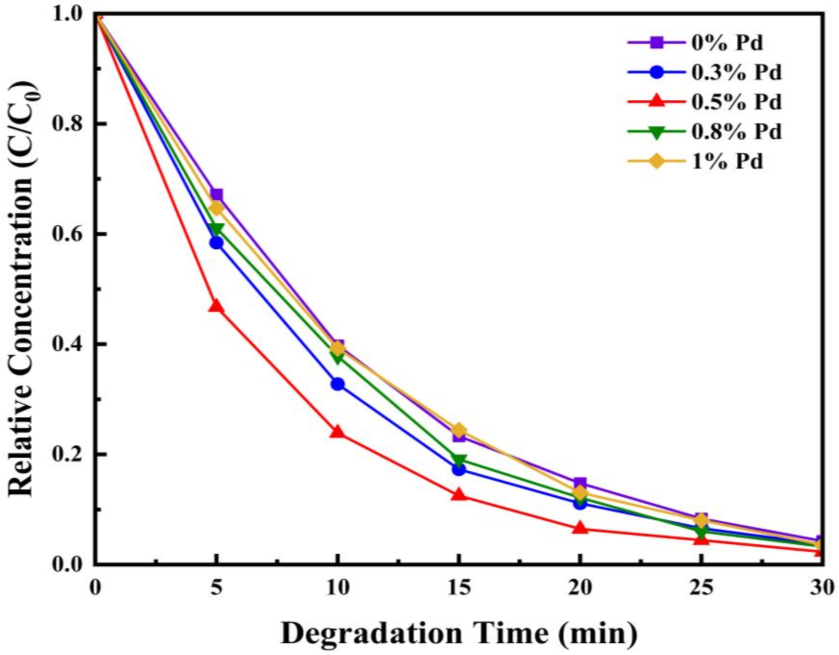

Figure 4-13: Photodegradation performance of Pd-Bi_2WO_6/BiOCl samples under varying wt% of Pd (calcination temperature: 135°C, calcination time: 12 hours, catalyst dosage: 0.5 g/L, degradation temperature: 20°C, initial pH: 4.8, and initial RhB concentration of 10 ppm).

Table 4-3: Pseudo-first order rate constant (k_{app}) and R^2 for Bi_2WO_6/BiOCl samples with different Pd loading.

Pd Content in Bi_2WO_6/BiOCl (wt %)	k_{app} (min^{-1})	R^2
0	0.1002	0.9906
0.3	0.1037	0.9978
0.5	0.1257	0.9974
0.8	0.1099	0.9980
1.0	0.1038	0.9963

The bare Bi_2WO_6/BiOCl sample exhibited a degradation rate of 0.1002 min^{-1} over a period of 30 minutes. When palladium was introduced, modified samples showed improvements in photoactivity. Samples synthesized with Pd loadings of 0.3%, 0.5%, 0.8%, and 1.0% had pseudo-first-order rate constants of 0.1037, 0.1257, 0.1009, and 0.1038 min^{-1}, respectively. This trend can be attributed to the presence of Pd NPs on the catalytic surface, creating surface plasmons that induce the SPR effect. As a result, the samples are able to absorb a greater amount of the solar spectrum, including the visible light region. This was demonstrated by the results in Section 4.3.4, which showed that palladium-modified samples had lower band gaps, allowing them to better access visible light radiation. As such, under the same illumination conditions, Pd-loaded samples are able to generate more e^-/h^+, leading to a greater number of active species that degrade the target pollutants. Additionally, the formation of a Schottky junction between the Pd and Bi_2WO_6/BiOCl interlayer enhances the separation of photogenerated e^- and h^+ due to electric fields present in the space-charge region, leading to lower recombination rates [79], [85].

From Table 4-3, as the Pd content increases from 0 to 0.5%, there is an increase in photoactivity of up to 25.45%. However, after 0.5%, there is a slight decline in activity, likely due to photonic scattering. As such, it was determined that 0.5% loading is the optimal amount for this system. This is consistent with the absorbance plots in Figure 4-9, which revealed that the 0.5% Pd sample had the broadest absorbance spectrum, ranging from 300 to 700 nm. The presence of an optimal loading quantity is an inherent trait of photocatalysts and is a result of an increase in photonic scattering. This is because an excess of palladium nanoparticles on the surface of Bi_2WO_6/BiOCl can cause light shielding, leading to fewer photons being absorbed by the catalyst. As a result, there is a decline in photonic efficiency, and fewer charge carriers are generated, causing a drop in the degradation rate. Moreover, an excess of nanoparticles can block active sites on the catalytic surface, reducing the number of pollutant molecules that can be adsorbed [85]. Such a study aims to balance the benefits of the plasmonic-induced SPR effect and excess NP loading. Therefore, it was determined that the optimal dopant concentration for Bi_2WO_6/BiOCl synthesized hydrothermally at 135°C for 12 hours is 0.5 wt% for maximal RhB degradation.

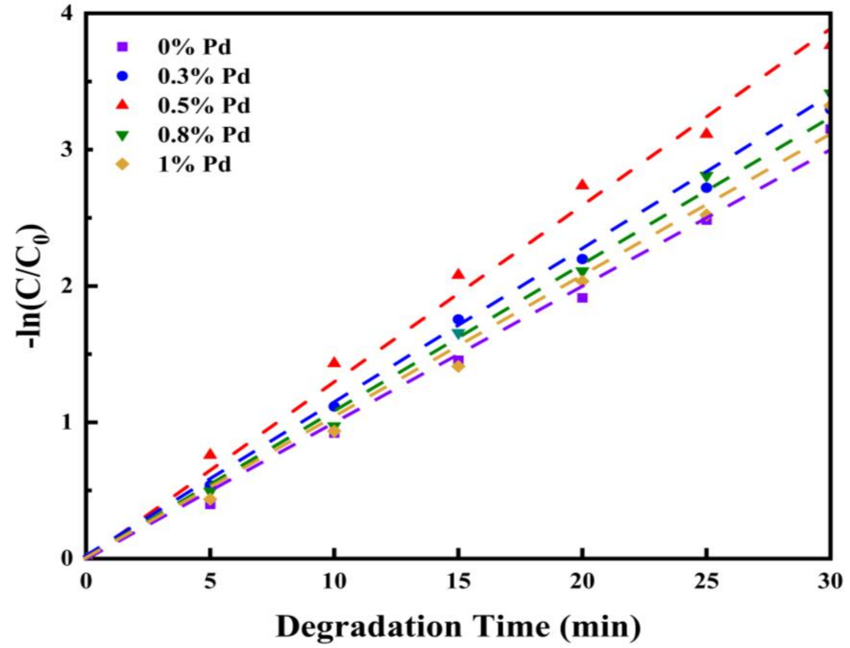

Figure 4-14: Pseudo-first order kinetic modelling of Pd-Bi_2WO_6/BiOCl samples with different Pd loading (catalyst dosage: 0.5 g/L, degradation temperature: 20°C, initial pH: 4.8, and initial RhB concentration of 10 ppm).

The kinetics of the RhB photodegradation process were evaluated as shown in Figure 4-14. It was determined that the data can be fitted according to the pseudo-first order kinetic model shown in Equation 2.22. The calculated k_{app} and R^2 values are shown in Table 4-3. All the samples exhibited R^2 values greater than 0.98, indicating good adherence to the pseudo-first order model.

4.5.2 Effect of Reaction Temperature

Since photocatalysis is mainly driven by photonic activation, it can be performed at moderate temperatures. This is a beneficial trait, as external heating sources are seldom required, thereby lowering energy and cost expenditure [54], [55]. Nonetheless, to better understand the behaviour of a newly synthesized catalyst, it is important to assess the effect of temperature on its degradation capacity. The influence of temperature in the range of 10 to 70°C with 0.5% Pd-Bi_2WO_6/BiOCl on the degradation of RhB was tested (Figure 4-15 and Table 4-4). When the system temperature was raised from 10 to 20°C, the rate doubled from 0.0616 to 0.1257 min^{-1}. Overall, as the temperature increased to 60°C, there was an increase in the degradation rate of RhB. The highest rate was recorded as 0.2477 min^{-1} at 60°C. This result matches previous studies, which found that most photocatalytic systems exhibit optimal activity in the range of 10 to 80°C. Beyond 60°C, there was a noticeable decline in the rate. This is because at elevated temperatures, there is an increased suppression of e^- and h^+, leading to a lower photonic efficiency. It is also important to note that at higher temperatures, the amount of dissolved oxygen content in the solution decreases, leading to fewer superoxide radicals being produced. This can hinder the rate of degradation, as $O_2^{\bullet -}$ radicals are major active species that can degrade pollutants. Finally, high temperatures can increase the desorption of attached substrate, causing less pollutant to be degraded [46], [54], [55].

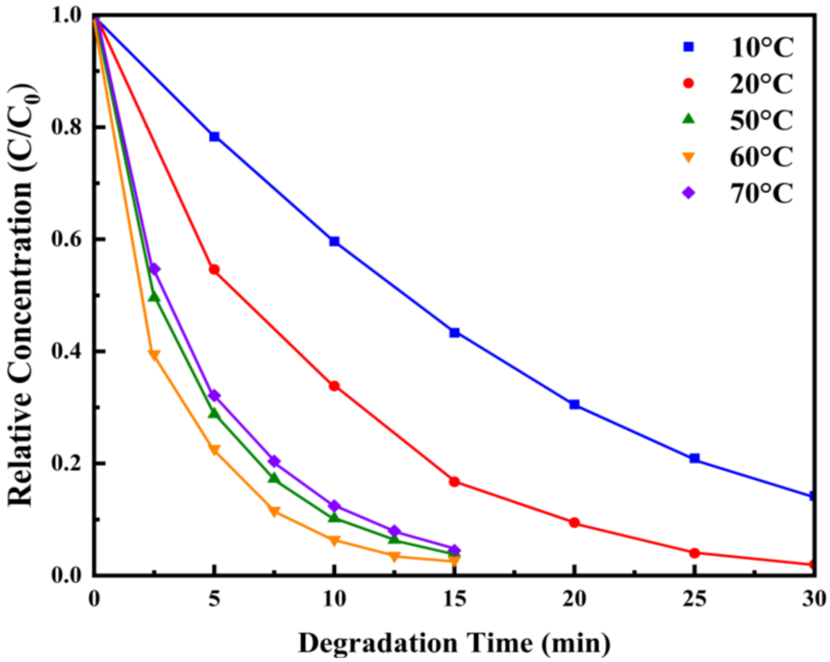

Figure 4-15: Photodegradation performance of Pd-Bi_2WO_6/BiOCl samples tested under different degradation temperatures (catalyst dosage: 0.5 g/L, initial pH: 4.8, and initial RhB concentration of 10 ppm).

Table 4-4: Pseudo-first order rate constant (k_{app}) and R^2 for Pd-Bi_2WO_6/BiOCl samples tested under different degradation temperatures.

Degradation Temperature (°C)	k_{app} (min^{-1})	R^2
10	0.0616	0.9960
20	0.1257	0.9974
50	0.2228	0.9977
60	0.2477	0.9944
70	0.2150	0.9920

4.5.3 Effect of Initial pH

The initial pH of a photocatalytic system is an important factor to consider, as it can influence the electrostatic interactions between the catalytic surface and substrate. Moreover, changes in pH can cause shifts in the redox reaction, ultimately increasing the number of reactive species generated [11]. As such, the effect of initial pH on the degradation of RhB was investigated. HCl and NaOH were used to control the pH in the acidic and basic ranges, respectively. Prior to any adjustment, the pH of 10 ppm aqueous RhB was determined to be 4.8, which is in line with literature data. Photodegradation tests were conducted from pH values of 3 to 11. The results shown in Figure 4-16 and Table 4-5 demonstrate that 0.5% Pd-Bi_2WO_6/BiOCl performed best at a pH of 6, with a high rate of 0.1563 min^{-1}. When the pH was lowered from 4.8 to 3, there was a noticeable decline in activity. A similar trend was observed when the pH was increased beyond 7 in the acidic range, indicating the catalyst is sensitive to extreme pH conditions. This relates to the studies conducted in Section 4.3.4, which showed that Bi_2WO_6 structures possess excellent adsorption capacities. It can be deduced that since extreme pH conditions produce excess H_3O^+ and OH^-, more species are adsorbed by the catalyst. This indiscriminate adsorption of non-pollutant species limits the available active sites for RhB. As a result, the adsorption capacity for the target pollutant is greatly diminished.

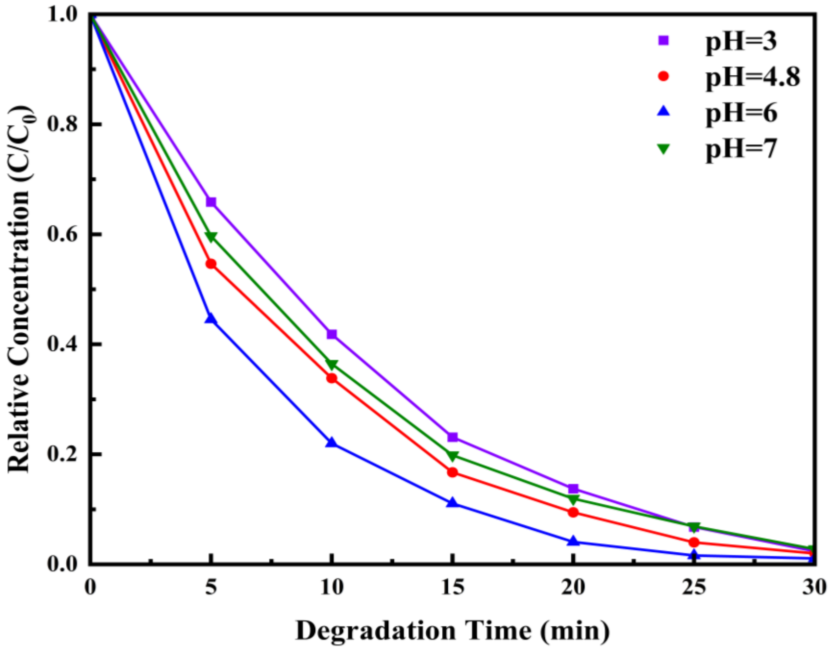

Figure 4-16: Photodegradation performance of Pd-Bi_2WO_6/BiOCl samples tested under different initial solution pH (catalyst dosage: 0.5 g/L, degradation temperature: 20°C, initial RhB concentration of 10 ppm).

Table 4-5: Pseudo-first order rate constant (k_{app}) and R^2 for Pd-Bi_2WO_6/BiOCl samples tested under different solution pH.

pH	k_{app} (min^{-1})	R^2
3	0.1016	0.9960
4.8	0.1257	0.9974
6	0.1563	0.9982
7	0.1160	0.9965
11	0.0043	0.9919

4.5.4 Effect of Photocatalyst Dosage

The amount of catalyst injected into a system is a key environmental and economic design consideration. As such, it is important to establish an optimal dosage to reduce excessive material costs. The effect of 0.5% Pd-Bi_2WO_6/BiOCl dosage on the photodegradation of RhB was evaluated in the range of 0.25 to 2 g/L. The results are listed in Figure 4-17 and Table 4-6. When catalyst concentration increased from 0.25 to 1 g/L, there was a significant increase in the degradation rate from 0.0279 to 0.1950 min^{-1}. This finding supports the idea that higher catalyst concentrations provide a greater number of active sites, thereby facilitating better adsorption of RhB molecules [11], [50]. When the dosage increased from 1 to 2 g/L, there was a slight decline in activity. This is a result of excessive catalyst particles increasing the turbidity of the suspension and obstructing light penetration. This causes photonic scattering, impeding catalysts from absorbing light energy, thereby reducing the generation of e$^-$ and h$^+$ [51]. As such, it was concluded that the optimal activity occurred at a dosage of 1 g/L of 0.5% Pd-Bi_2WO_6/BiOCl.

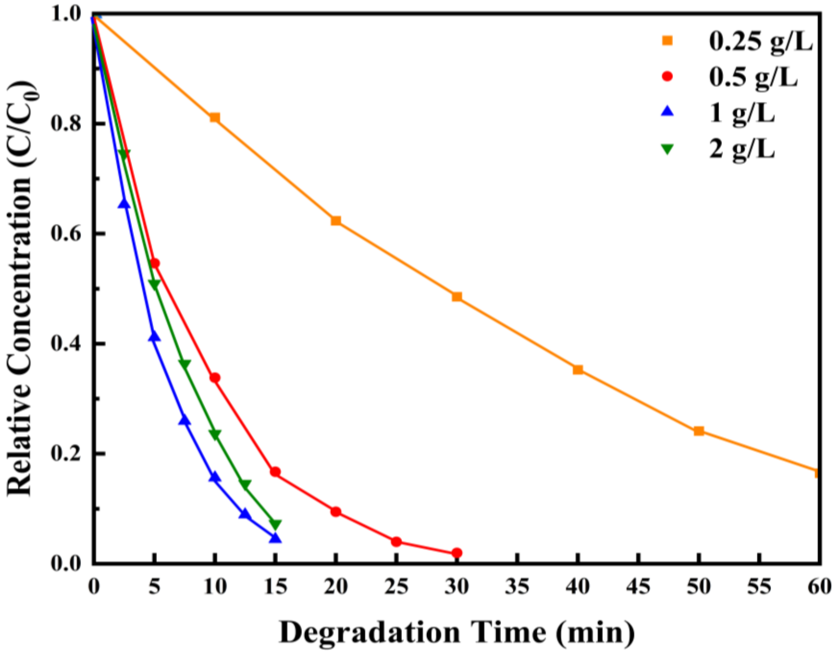

Figure 4-17: Photodegradation performance of Pd-Bi_2WO_6/BiOCl samples tested with different catalyst dosage (initial pH: 4.8, degradation temperature: 20°C, and initial RhB concentration of 10 ppm).

Table 4-6: Pseudo-first order rate constant (k_{app}) and R^2 for Pd-Bi_2WO_6/BiOCl samples tested with different catalyst dosage.

Catalyst Dosage (g/L)	k_{app} (min^{-1})	R^2
0.25	0.0279	0.9933
0.50	0.1257	0.9974
1.0	0.1950	0.9969
2.0	0.1574	0.9903

4.5.5 Effect of RhB Concentration

Further to the discussion in the previous section on the economic feasibility of photocatalytic systems, the substrate concentration should also be considered. As such, the degradation rate was evaluated by varying the concentration of RhB from 5 to 20 ppm. As shown in Figure 4-18 and Table 4-7, when the concentration was increased from 5 to 20 ppm, there was a notable decrease in the degradation rate. The most significant drop was noted from 10 to 20 ppm (57.72%). These results indicate that photodegradation is preferable at low pollutant levels. This phenomenon can be attributed to several reasons. First, at elevated substrate levels, there is an insufficient number of active sites, creating a competition between adsorption and degradation kinetics. Moreover, the influence of reactive intermediates becomes more prominent, interfering with target pollutants. Finally, more RhB molecules in the suspension and catalytic surface cause increased photonic scattering and less light absorption [11], [23].

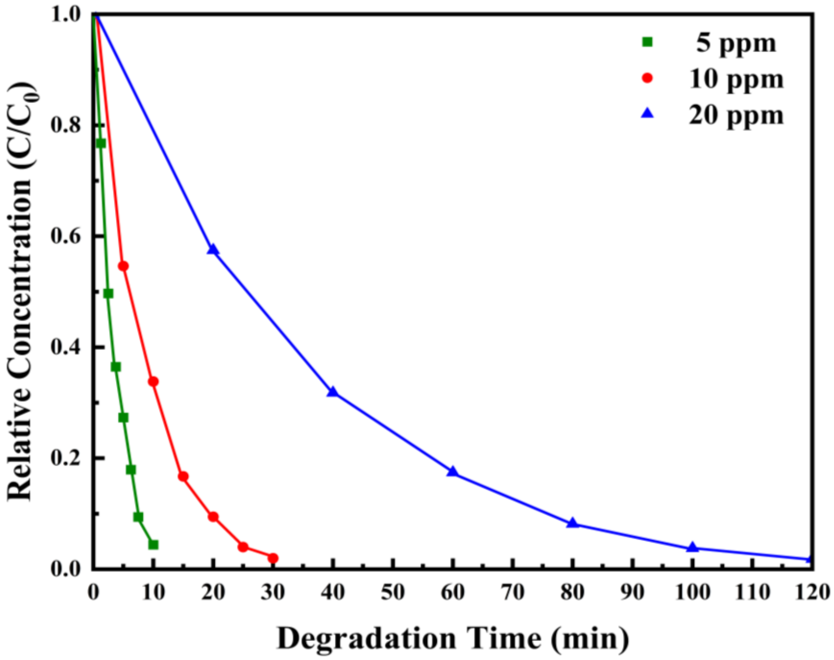

Figure 4-18: Photodegradation performance of Pd-Bi_2WO_6/BiOCl samples tested with different initial RhB concentrations (catalyst dosage: 0.5 g/L, degradation temperature: 20°C, initial pH of 4.8).

Table 4-7: Pseudo-first order rate constant (k_{app}) and R^2 for Pd-Bi_2WO_6/BiOCl samples tested with different initial RhB concentration.

RhB Concentration (ppm)	k_{app} (min^{-1})	R^2
5	0.2973	0.9944
10	0.1257	0.9974
20	0.0321	0.9977

4.5.6 RhB Degradation Pathway

The RhB degradation pathway was assessed through the use of UV-vis spectroscopy. The UV-vis spectra of samples taken during the course of a photodegradation process is shown in the plot below.

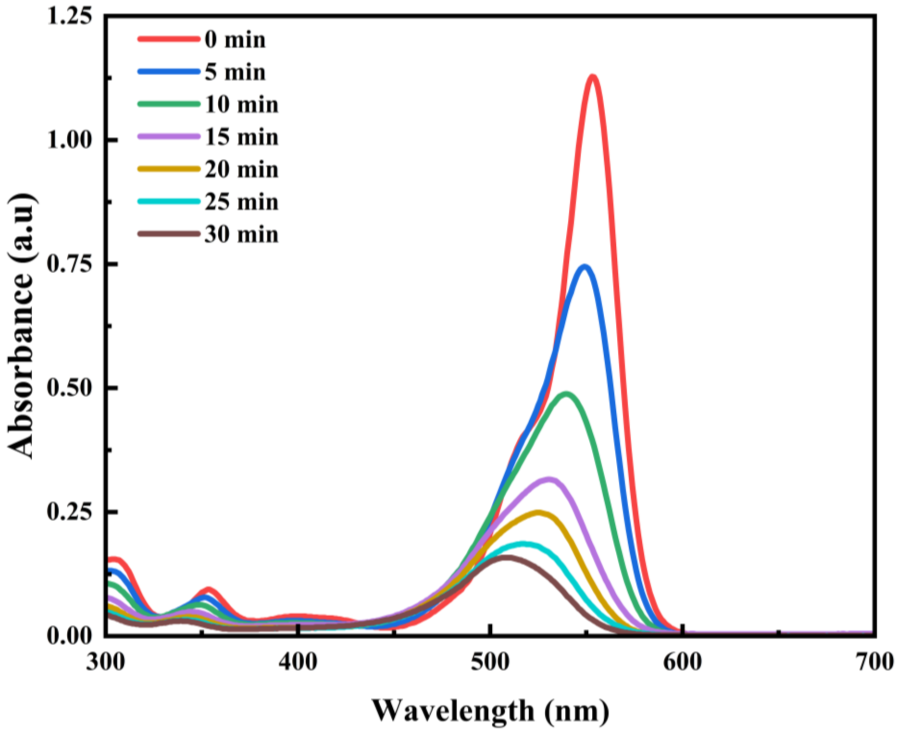

Figure 4-19: UV-vis spectra of RhB under different irradiation times (Pd-Bi_2WO_6/BiOCl dosage: 0.5 g/L, degradation temperature 20°C, initial pH: 4.8, and initial RhB concentration of 10 ppm).

The degradation of RhB consists of two main pathways. The first pathway occurs via the destruction of the central conjugated structure. This mechanism includes •OH radicals attacking the central chromophore rings of RhB molecules [105]. This process can be detected if there is no observable shift in the peak wavelength in the absorbance plot. However, the plot above shows a clear shift in the peak wavelength during the course of the degradation process. As such, it was determined that 0.5% Pd-Bi_2WO_6/BiOCl degrades RhB via the *N-de-ethylation* process, wherein multiple intermediates are produced in the form of *N,N,N'-triethyl Rhodamine* (TER), *N,N'-diethyl*

Rhodamine (DER), *N-ethyl Rhodamine* (ER), and *Rhodamine* with peaks located at 539 nm, 520 nm, 510 nm, and 500 nm, respectively [106]. From Figure 4-19, there is a characteristic blue shift in the absorbance peak wavelength coinciding with lower absorbance, indicating the presence of various intermediates over time. This is depicted in Figure 4-20, which shows the variation in the major absorbance peak wavelength and the relative absorbance values as a function of time.

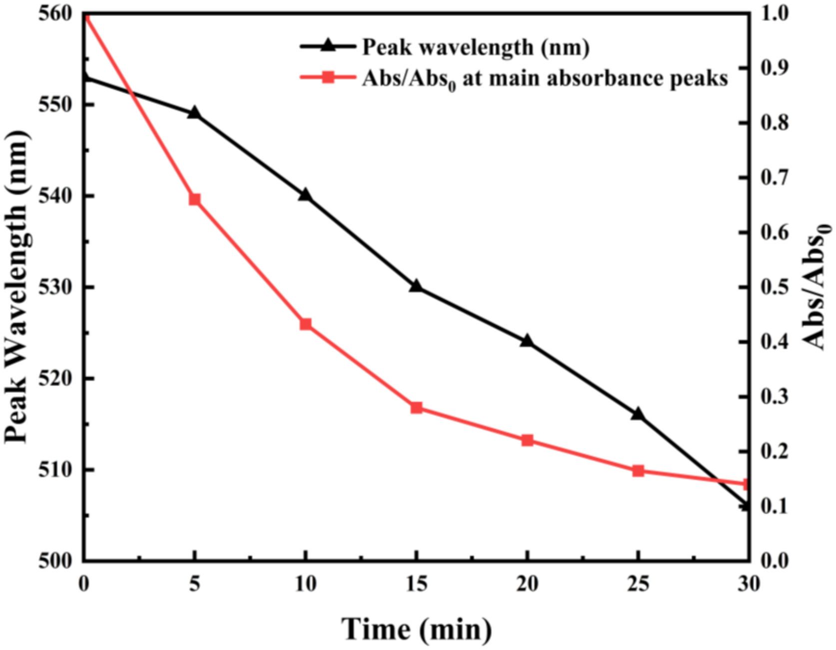

Figure 4-20: Corresponding wavelengths of major absorbance peaks and relative absorbance values of RhB under different irradiation times.

4.5.7 Quenching Experiments

One of the main qualities of photocatalytic water treatment is the formation of oxidative species. These include holes (h^+), superoxide radicals ($O_2^{\bullet -}$), and hydroxyl radicals (•OH), which provide effective breakdown of organic molecules. As such, to gain further insight into RhB degradation, a series of quenching experiments with different scavengers was conducted to assess the role of the active species. Ethylenediaminetetraacetic acid disodium salt (EDTA-2Na) was used to inhibit the degradation ability of h^+, isopropanol (IPA) was used to inhibit •OH, and L-ascorbic acid (LAA) was used to inhibit $O_2^{\bullet -}$ [106]. It was observed that the RhB degradation rate decreased with the addition of each of the scavengers. It was found that the addition of EDTA-2Na had the greatest impact on the photodegradation of RhB, with the rate decreasing from 0.1257 to 0.0364 min^{-1}, indicating that h^{+} served as the primary degrading agent. This finding supports the results in the previous section, which revealed that the optimal operating pH is 6. This is because at slightly acidic conditions, the presence of holes is favoured, allowing for more oxidation to occur. According to Equation 2-12 to 2-15*,* holes are involved in several reactions, including reacting with OH^{-} to form •OH, reacting with H_2O molecules to produce •OH, and in directly oxidizing target pollutants. To uncover which mechanism was dominant, the effect of hydroxyl species was assessed. When IPA was introduced, there was a notable drop-in activity of 36.74%, indicating that hydroxyl radicals are also active species. As such, it can be assumed that there is a synergistic effect of holes and hydroxyl radicals in the degradation of RhB, following the second pathway described in Equation 2-13. Moreover, when LAA was added, there was a negligible difference in rate, suggesting that the role of superoxide radicals in RhB photodegradation is limited. The results of the quenching experiments are presented in Figure 4-21.

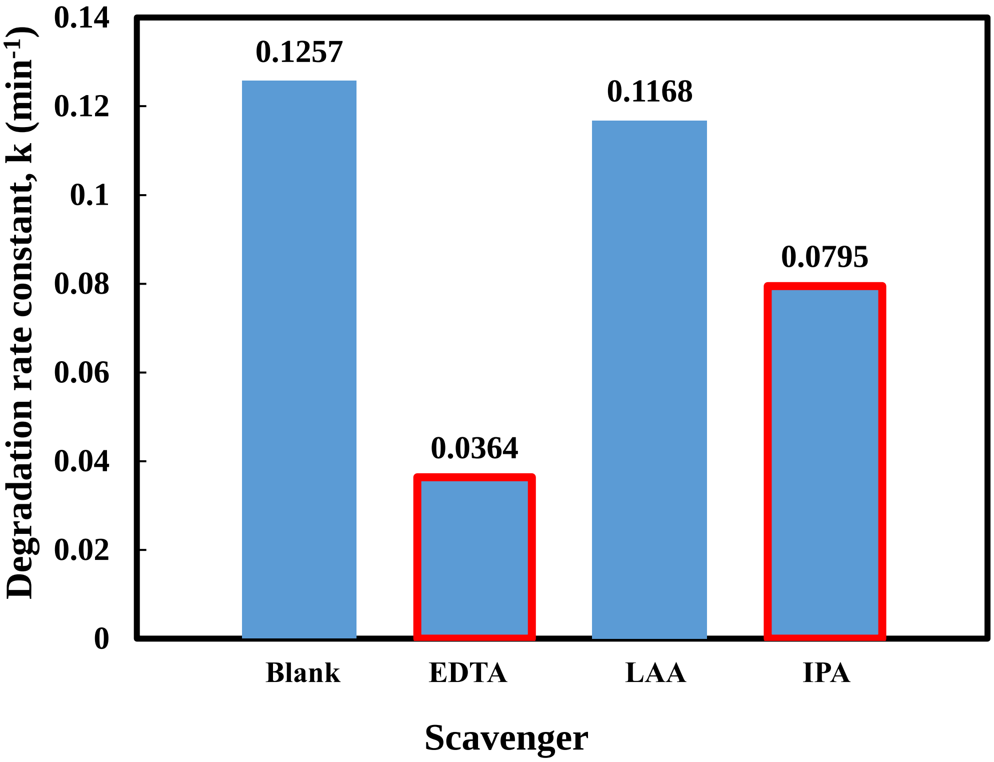

Figure 4-21: Degradation rates of RhB tested with different scavengers (catalyst dosage: 0.5 g/L, degradation temperature: 20°C, initial pH: 4.8, and initial RhB concentration of 10 ppm).

4.5.8 Photocatalytic Mechanism

The results found in the previous passage can help in understanding the photocatalytic mechanism for 0.5% Pd-Bi_2WO_6/BiOCl. In order to achieve this, it is important to first use the band gap of Bi_2WO_6 and BiOCl to ascertain the band positions. Using the electronegativity theory proposed by Mulliken in Equations 2-2 and 2-3, the valence (E_{VB}) and conduction band (E_{CB}) positions can be estimated. As shown in Table 4-8, the valence band positions for Bi_2WO_6 and BiOCl were calculated to be 3.15 and 3.53 eV, respectively. This suggests that the photogenerated holes possess a significantly greater redox potential relative to other oxidative species, including •OH/OH^- (+1.99 eV). From the data collected in Table 4-8, a schematic mechanism can be constructed for 0.5% Pd-Bi_2WO_6/BiOCl, as presented in Figure 4-22.

Table 4-8: Estimated band positions for Bi_2WO_6 and BiOCl photocatalysts. Electronic properties (χ_p and E^e) were collected from CRC handbook [107].

Photocatalyst	χ_p (eV)	E^e (eV)	E_g (eV)	E_{CB} (eV)	E_{VB} (eV)
Bi_2WO_6	6.21	4.50	2.89	0.26	3.15
BiOCl	6.36	4.50	3.35	0.18	3.53

Based on the valence and conduction layers of BiOCl being located at greater depths, it was determined that Bi_2WO_6/BiOCl formed a type I heterojunction. Typically, photogenerated h^+ and e^- in a type I heterojunction readily transport from the structure with the lower valence and higher conduction band to the other structure [11]. It should be noted that it can be limited by poor spatial separation of the charge carrier species, leading to an accumulation of electrons and holes and a lower photonic efficiency. However, the addition of a Schottky junction between Pd metal and Bi_2WO_6 induces an electromagnetic field in the space-charge region, allowing for increased charge separation [70], [72]. This allows the Pd nanoparticles to act as charge traps for e^- in the CB of Bi_2WO_6, thereby preventing recombination. Moreover, the surface plasmon resonance effect helps to capture a significant amount of incoming visible light photons, allowing for more conduction band electrons to be produced. A detailed photocatalytic diagram is proposed in the figure below.

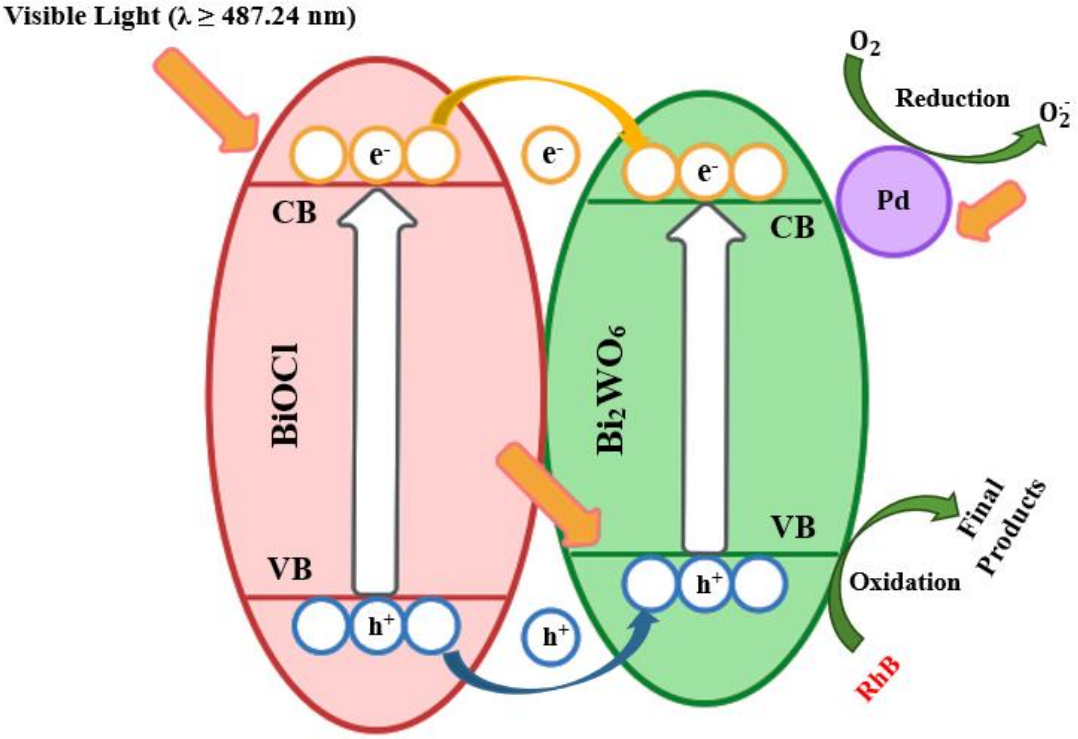

Figure 4-22: Proposed photocatalytic mechanism for 0.5% Pd-Bi_2WO_6/BiOCl.

From the diagram above, it can be seen that when the catalyst absorbs light with energy greater than or equal to its band gap (2.74 eV), electrons from the valence bands of both BiOCl and Bi_2WO_6 are excited to their respective conduction bands, leaving holes behind. However, since the BiOCl valence and conduction bands are higher and lower than those of Bi_2WO_6, the electrons and holes accumulate on Bi_2WO_6. This is consistent with type I heterojunctions. The electrons from the CB_{Bi2WO6} subsequently move to Pd, which acts as a charge trap, mitigating recombination. These electrons are then able to participate in the reduction of O_2 to form superoxide radicals. This species, however, is inconsequential in the context of RhB degradation, as was revealed by the quenching experiments. Rather, the dominant active species are h^+ and •OH. As such, holes accumulated on VB_{Bi2WO6} react with OH^- to form •OH, leading to the degradation of RhB. Moreover, some of the h^+ should be considered as directly attacking the pollutants as well. This is because of the high redox potential of the two semiconductors in the heterojunctions. As such, a synergistic effect between h^+ and •OH combines to provide effective degradation of RhB molecules.

4.5.9 Catalyst Stability

The reusability and stability of catalyst is crucial in understanding its practical application. Recyclability tests for 0.5% Pd-Bi_2WO_6/BiOCl were conducted in order to assess the catalyst stability over several runs. After each run, the catalyst was centrifuged, recovered, and subsequently mixed with a fresh RhB solution. The results are shown in the plot below.

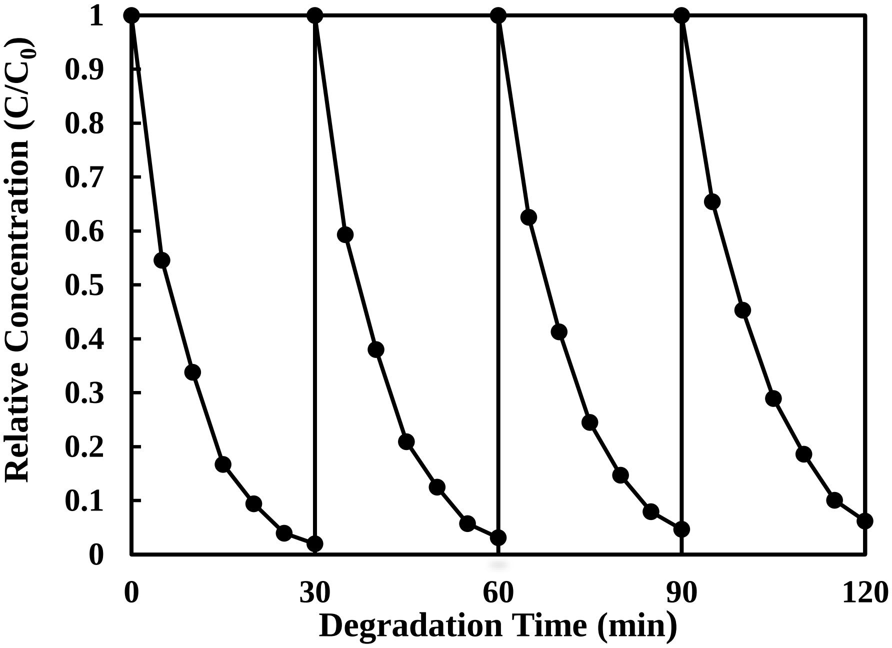

Figure 4-23: Photodegradation performance of 0.5% Pd-Bi_2WO_6/BiOCl over a four stage recycle test (catalyst dosage: 0.5 g/L, degradation temperature: 20°C, initial pH: 4.8, RhB concentration of 10 ppm).

The results from Figure 4-23 demonstrate that 0.5% Pd-Bi_2WO_6/BiOCl exhibits considerable stability after four successive runs. This result indicates that the intrinsic crystal structure of the catalyst remains intact after multiple photodegradation tests. Since the reactions take place on the surface of the catalyst, it is reasonable that the lattice structure remains intact. It is also worth considering the role of the surface palladium in the overall stability of the sample. As mentioned in the XRD discussion in Section 4.3.1, Pd resides on the surface of the heterojunction rather than in the crystal lattice. As such, it could be reasonable to assume that the surface nanoparticles may face a greater level of stress during the course of a photodegradation process. However, several studies have shown that among the noble metals, Pd nanoparticles possess a very stable structure, which makes them resilient during photocatalysis [26]. This consideration is supported by the findings in the plot above, which show that the photocatalyst exhibited similar behaviour during the initial phase of each process, indicating that the Pd-driven visible light responsiveness was unaltered. Therefore, it is reasonable to assume that Pd NPs did indeed remain stable after each reaction. This result is important from an economic perspective as well, as the catalyst can be reused several times to yield effective pollutant decontamination. When assessing the slight decline in activity over the several stages of the study, it can be attributed to adsorbed intermediates that remain on the surface of the catalyst, occupy active sites, and prevent RhB from being adsorbed. However, the extent of intermediate interference seems inconsequential, owing to the minimal loss of activity after four runs.

4.6 Conclusion

In this work, a photoreduction technique was used to deposit palladium nanoparticles on the surface of hydrothermally synthesized Bi_2WO_6/BiOCl composites. The photocatalytic activity of the samples was tested to highlight the effects of several experimental and operational conditions. It was determined that the addition of Pd to Bi_2WO_6/BiOCl significantly improves its visible light activity by 25.45%, with the optimal loading quantity being 0.5 wt%. It was also determined that the novel catalyst displays preferable results in slightly acidic conditions at moderate temperatures. Moreover, a higher number of active sites due to high surface area, lower pollutant levels, and slightly higher catalyst dosages led to maximum photodegradation. Quenching experiments revealed that both hydroxyl radicals (•OH) and holes (h^+) played significant roles in the oxidation process, with the latter being the dominant active species. Recycle tests indicated that Pd-

Bi_2WO_6/BiOCl exhibits substantial stability over the course of multiple runs, owing to its stable crystal and surface structure. Overall, the synthesis and testing of novel Pd-Bi_2WO_6/BiOCl serve as evidence that the modification of heterojunction catalysts with metal nanoparticles can be an effective way to enhance the visible-light treatment of organic pollutants in water.

4.7 Nomenclature

k_{app}	Apparent rate constant
E_g	Band gap energy
$Bi(NO_3)_3 \cdot 5H_2O$	Bismuth (III) nitrate pentahydrate
Bi_2O_2	Bismuth oxide
BiOCl	Bismuth oxychloride
BiOX	Bismuth oxyhalide
Bi_2WO_6	Bismuth tungstate
CO_2	Carbon dioxide
c_t	Concentration at specific time
c	Concentration of substrate
E_{CB}	Conduction band edge
k_2	Equilibrium rate constant for pseudo second-order adsorption
e^-	Electron
E^e	Free electron energy
h^+	Hole
H_3O^+	Hydronium ion
OH^-	Hydroxide anion
•OH	Hydroxyl radical
c_0	Initial concentration
O_2	Oxygen
Pd	Palladium
ppm	Part per million

NaCl	Sodium chloride
$Na_2WO_4 \cdot 2H_2O$	Sodium tungstate dihydrate
q_e	Sorption capacity at equilibrium
q_t	Sorption capacity at specific time
$O_2^{\bullet -}$	Superoxide radical
t	Time
WO_6	Tungstate
E_{VB}	Valence band edge
H_2O	Water

4.8 Greek Letters

λ	Absorbance-edge wavelength
θ	Angle between sample and x-ray source
χ_p	Semiconductor electronegativity
ϕ	Work function

4.9 Abbreviations

AOP	Advanced Oxidation Process
ACS	American Chemical Society
BET	Brunauer-Emmett-Teller
CB	Conduction Band
DLD	Delay Line Detector
DER	Diethyl Rhodamine
DRS	Diffuse Reflectance Spectroscopy
DDW	Distilled and Deionized Water

EDTA	Ethylenediaminetetraacetic Acid
ER	Ethyl Rhodamine
FE	Field Emission
IUPAC	International Union of Pure and Applied Chemistry
IPA	Isopropanol
JCPDS	Joint Committee on Powder Diffraction Standards
LAA	L-Ascorbic Acid
NP	Nanoparticle
RhB	Rhodamine B
SEM	Scanning Electron Microscopy
SPR	Surface Plasmon Resonance
TER	Triethyl Rhodamine
UV	Ultraviolet
UV-vis	Ultraviolet Visible
VB	Valence Band
XRD	X-ray Diffraction
XPS	X-ray Photoelectron Spectroscopy

References

[1] M. A. Al-Nuaim, A. A. Alwasiti, and Z. Y. Shnain, "The photocatalytic process in the treatment of polluted water," *Chemical Papers 2022 77:2*, vol. 77, no. 2, pp. 677–701, Oct. 2022, doi: 10.1007/S11696-022-02468-7.

[2] E. Koncagül and R. Connor, "The United Nations World Water Development Report 2023: partnerships and cooperation for water; facts, figures and action examples," Paris, 2023.

[3] S. Mishra and B. Sundaram, "A review of the photocatalysis process used for wastewater treatment," *Mater Today Proc*, Jul. 2023, doi: 10.1016/J.MATPR.2023.07.147.

[4] G. Crini and E. Lichtfouse, "Advantages and disadvantages of techniques used for wastewater treatment," *Environ Chem Lett*, vol. 17, no. 1, pp. 145–155, Mar. 2019, doi: 10.1007/s10311-018-0785-9.

[5] A. O. Oluwole, E. O. Omotola, and O. S. Olatunji, "Pharmaceuticals and personal care products in water and wastewater: a review of treatment processes and use of photocatalyst immobilized on functionalized carbon in AOP degradation," *BMC Chem*, vol. 14, no. 1, p. 62, Dec. 2020, doi: 10.1186/s13065-020-00714-1.

[6] G. Ren *et al.*, "Recent Advances of Photocatalytic Application in Water Treatment: A Review," *Nanomaterials 2021, Vol. 11, Page 1804*, vol. 11, no. 7, p. 1804, Jul. 2021, doi: 10.3390/NANO11071804.

[7] S. K. Loeb *et al.*, "The Technology Horizon for Photocatalytic Water Treatment: Sunrise or Sunset?," *Environ Sci Technol*, vol. 53, no. 6, pp. 2937–2947, Mar. 2019, doi: 10.1021/ACS.EST.8B05041.

[8] M. M. Ayyub and C. N. R. Rao, "Design of efficient photocatalysts through band gap engineering," in *Nanostructured Photocatalysts*, Elsevier, 2020, pp. 1–18. doi: 10.1016/B978-0-12-817836-2.00001-6.

[9] S. Mishra and B. Sundaram, "A review of the photocatalysis process used for wastewater treatment," *Mater Today Proc*, Jul. 2023, doi: 10.1016/j.matpr.2023.07.147.

[10] S. Y. Lee and S. J. Park, "TiO2 photocatalyst for water treatment applications," *Journal of Industrial and Engineering Chemistry*, vol. 19, no. 6, pp. 1761–1769, Nov. 2013, doi: 10.1016/J.JIEC.2013.07.012.

[11] L. Wang and J. Yu, "Principles of photocatalysis," 2023, pp. 1–52. doi: 10.1016/B978-0-443-18786-5.00002-0.

[12] D. O. Charkin, D. N. Lebedev, and S. M. Kazakov, "Multiple cation and anion substitutions into the structures of Bi2WO6 and PbBi3WO8Cl," *J Alloys Compd*, vol. 536, pp. 155–160, Sep. 2012, doi: 10.1016/J.JALLCOM.2012.04.113.

[13] Z. Zhu *et al.*, “Recent progress in Bi_2WO_6-Based photocatalysts for clean energy and environmental remediation: Competitiveness, challenges, and future perspectives,” *Nano Select*, vol. 2, no. 2, pp. 187–215, Feb. 2021, doi: 10.1002/nano.202000127.

[14] Z. Li, L. Zhu, W. Wu, S. Wang, and L. Qiang, “Highly efficient photocatalysis toward tetracycline under simulated solar-light by Ag+-CDs-Bi2WO6: Synergistic effects of silver ions and carbon dots,” *Appl Catal B*, vol. 192, pp. 277–285, Sep. 2016, doi: 10.1016/j.apcatb.2016.03.045.

[15] X. Yu, J. Yang, K. Ye, X. Fu, Y. Zhu, and Y. Zhang, “Facile one-step synthesis of BiOCl/BiOI heterojunctions with exposed {001} facet for highly enhanced visible light photocatalytic performances,” *Inorg Chem Commun*, vol. 71, pp. 45–49, Sep. 2016, doi: 10.1016/J.INOCHE.2016.06.034.

[16] Z. Liang, C. Zhou, J. Yang, Q. Mo, Y. Zhang, and Y. Tang, “Visible light responsive Bi 2 WO 6 /BiOCl heterojunction with enhanced photocatalytic activity for degradation of tetracycline and rohdamine B,” *Inorg Chem Commun*, vol. 93, pp. 136–139, Jul. 2018, doi: 10.1016/j.inoche.2018.05.022.

[17] G. Zhang, Y. Tan, Z. Sun, and S. Zheng, “Synthesis of BiOCl/TiO 2 heterostructure composites and their enhanced photocatalytic activity,” *J Environ Chem Eng*, vol. 5, no. 1, pp. 1196–1204, Feb. 2017, doi: 10.1016/j.jece.2017.01.040.

[18] Q. Su *et al.*, “Construction of a Bioinspired Hierarchical $BiVO_4$/BiOCl Heterojunction and Its Enhanced Photocatalytic Activity for Phenol Degradation,” *ACS Appl Mater Interfaces*, vol. 13, no. 28, pp. 32906–32915, Jul. 2021, doi: 10.1021/acsami.1c05117.

[19] X. Zhang, G. Xu, J. Hu, J. Lv, J. Wang, and Y. Wu, “Fabrication and photocatalytic performances of BiOCl nanosheets modified with ultrafine Bi_2O_3 nanocrystals,” *RSC Adv*, vol. 6, no. 68, pp. 63241–63249, 2016, doi: 10.1039/C6RA09919J.

[20] N. Tahmasebi, Z. Maleki, and P. Farahnak, “Enhanced photocatalytic activities of Bi2WO6/BiOCl composite synthesized by one-step hydrothermal method with the assistance of HCl,” *Mater Sci Semicond Process*, vol. 89, pp. 32–40, Jan. 2019, doi: 10.1016/j.mssp.2018.08.026.

[21] Y. Huang *et al.*, “Peroxymonosulfate Activation by Bi2WO6/BiOCl Heterojunction Nanocomposites under Visible Light for Bisphenol A Degradation,” *Nanomaterials*, vol. 11, no. 11, p. 3130, Nov. 2021, doi: 10.3390/nano11113130.

[22] M. Guo *et al.*, “Bi2WO6–BiOCl heterostructure with enhanced photocatalytic activity for efficient degradation of oxytetracycline,” *Sci Rep*, vol. 10, no. 1, p. 18401, Oct. 2020, doi: 10.1038/s41598-020-75003-x.

[23] L. Derikvand and N. Tahmasebi, “Synthesis and photocatalytic performance of Bi2WO6/BiOX (X=Cl, Br, I) composites for RhB degradation under visible light,” *Korean Journal of Chemical Engineering*, vol. 38, no. 1, pp. 163–169, Jan. 2021, doi: 10.1007/s11814-020-0687-y.

[24] J. Chen *et al.*, “Preparation of BiOCl/Bi2WO6 Photocatalyst for Efficient Fixation on Cotton Fabric: Applications in UV Shielding and Self-Cleaning Performances,” *Materials*, vol. 14, no. 22, p. 7002, Nov. 2021, doi: 10.3390/ma14227002.

[25] A. Nazir, P. Huo, H. Wang, Z. Weiqiang, and Y. Wan, “A review on plasmonic-based heterojunction photocatalysts for degradation of organic pollutants in wastewater,” *J Mater Sci*, vol. 58, no. 15, pp. 6474–6515, Apr. 2023, doi: 10.1007/s10853-023-08391-w.

[26] Z. Li and X. Meng, “Recent development on palladium enhanced photocatalytic activity: A review,” *J Alloys Compd*, vol. 830, p. 154669, Jul. 2020, doi: 10.1016/j.jallcom.2020.154669.

[27] M. Arumugam, R. Koutavarapu, K.-K. Seralathan, S. Praserthdam, and P. Praserthdam, “Noble metals (Pd, Ag, Pt, and Au) doped bismuth oxybromide photocatalysts for improved visible light-driven catalytic activity for the degradation of phenol,” *Chemosphere*, vol. 324, p. 138368, May 2023, doi: 10.1016/j.chemosphere.2023.138368.

[28] Z. Li and X. Meng, “Recent development on palladium enhanced photocatalytic activity: A review,” *J Alloys Compd*, vol. 830, p. 154669, Jul. 2020, doi: 10.1016/j.jallcom.2020.154669.

[29] R. Wang, B. Li, Y. Xiao, X. Tao, X. Su, and X. Dong, “Optimizing Pd and Au-Pd decorated Bi2WO6 ultrathin nanosheets for photocatalytic selective oxidation of aromatic alcohols,” *J Catal*, vol. 364, pp. 154–165, 2018, doi: 10.1016/j.jcat.2018.05.015.

[30] S. Y. Lee and S. J. Park, “TiO2 photocatalyst for water treatment applications,” *Journal of Industrial and Engineering Chemistry*, vol. 19, no. 6, pp. 1761–1769, Nov. 2013, doi: 10.1016/J.JIEC.2013.07.012.

[31] Alexander Eibner, “Action of Light on Pigments I,” *Chem-ZTG*, pp. 753–755, 1911.

[32] C. F. Goodeve and J. A. Kitchener, “The mechanism of photosensitisation by solids,” *Transactions of the Faraday Society*, vol. 34, p. 902, 1938, doi: 10.1039/tf9383400902.

[33] V.N. Filimonov, “Photocatalytic Oxidation of Gaseous Isopropanol on ZnO + TiO 2,” *Dokl Akad Nauk SSSR*, vol. 154, no. 4, pp. 922–925, 1964.

[34] A. FUJISHIMA and K. HONDA, “Electrochemical Photolysis of Water at a Semiconductor Electrode,” *Nature*, vol. 238, no. 5358, pp. 37–38, Jul. 1972, doi: 10.1038/238037a0.

[35] S. Zhu and D. Wang, “Photocatalysis: Basic Principles, Diverse Forms of Implementations and Emerging Scientific Opportunities,” *Adv Energy Mater*, vol. 7, no. 23, Dec. 2017, doi: 10.1002/aenm.201700841.

[36] S. Mishra and B. Sundaram, “Efficacy of nanoparticles as photocatalyst in leachate treatment,” *Nanotechnology for Environmental Engineering*, vol. 7, no. 1, pp. 173–192, Mar. 2022, doi: 10.1007/s41204-021-00209-x.

[37] H. Wang *et al.*, "Semiconductor heterojunction photocatalysts: design, construction, and photocatalytic performances," *Chem Soc Rev*, vol. 43, no. 15, p. 5234, Jul. 2014, doi: 10.1039/C4CS00126E.

[38] P. Doran, *Engineering Principles Second Edition*. 2013. Accessed: Nov. 19, 2022. [Online]. Available: http://www.sciencedirect.com:5070/book/9780122208515/bioprocess-engineering-principles

[39] S. A. Heredia Deba, B. A. Wols, D. R. Yntema, and R. G. H. Lammertink, "Photocatalytic ceramic membrane: Effect of the illumination intensity and distribution," *J Photochem Photobiol A Chem*, vol. 437, p. 114469, Mar. 2023, doi: 10.1016/j.jphotochem.2022.114469.

[40] Suresh C. Ameta and Rakshit Ameta, *Advanced Oxidation Processes for Wastewater Treatment Emerging Green Chemical Technology*, 1st ed. Elsevier, 2018.

[41] T. G. Mayerhöfer, S. Pahlow, and J. Popp, "The Bouguer-Beer-Lambert Law: Shining Light on the Obscure.," *Chemphyschem*, vol. 21, no. 18, pp. 2029–2046, Sep. 2020, doi: 10.1002/cphc.202000464.

[42] C. Belver, J. Bedia, M. Peñas-Garzón, V. Muelas-Ramos, A. Gómez-Avilés, and J. J. Rodriguez, "Structured photocatalysts for the removal of emerging contaminants under visible or solar light," in *Visible Light Active Structured Photocatalysts for the Removal of Emerging Contaminants*, Elsevier, 2020, pp. 41–98. doi: 10.1016/B978-0-12-818334-2.00003-1.

[43] M. Bodzek and M. Rajca, "Photocatalysis in the treatment and disinfection of water. Part I. Theoretical backgrounds / Fotokataliza w oczyszczaniu i dezynfekcji wody część i. podstawy teoretyczne," *Ecological Chemistry and Engineering S*, vol. 19, no. 4, pp. 489–512, Nov. 2012, doi: 10.2478/v10216-011-0036-5.

[44] Y. Liang and J. Shi, "Effect of Halide Ions on the Microstructure of Bi2WO6 with Enhanced Removal of Rhodamine B," *J Inorg Organomet Polym Mater*, vol. 30, no. 8, pp. 2872–2880, Aug. 2020, doi: 10.1007/s10904-019-01437-0.

[45] P. O. Oladoye, T. O. Ajiboye, E. O. Omotola, and O. J. Oyewola, "Methylene blue dye: Toxicity and potential elimination technology from wastewater," *Results in Engineering*, vol. 16, p. 100678, Dec. 2022, doi: 10.1016/j.rineng.2022.100678.

[46] B. Liu, X. Zhao, C. Terashima, A. Fujishima, and K. Nakata, "Thermodynamic and kinetic analysis of heterogeneous photocatalysis for semiconductor systems," *Physical Chemistry Chemical Physics*, vol. 16, no. 19, p. 8751, 2014, doi: 10.1039/c3cp55317e.

[47] A. H. Navidpour, S. Abbasi, D. Li, A. Mojiri, and J. L. Zhou, "Investigation of Advanced Oxidation Process in the Presence of TiO2 Semiconductor as Photocatalyst: Property, Principle, Kinetic Analysis, and Photocatalytic Activity," *Catalysts*, vol. 13, no. 2, p. 232, Jan. 2023, doi: 10.3390/catal13020232.

[48] A. Mohamed *et al.*, “Rapid photocatalytic degradation of phenol from water using composite nanofibers under UV,” *Environ Sci Eur*, vol. 32, no. 1, p. 160, Dec. 2020, doi: 10.1186/s12302-020-00436-0.

[49] J. Z. Bloh, “A Holistic Approach to Model the Kinetics of Photocatalytic Reactions,” *Front Chem*, vol. 7, Mar. 2019, doi: 10.3389/fchem.2019.00128.

[50] J. M. Doña *et al.*, “The effect of dosage on the photocatalytic degradation of organic pollutants,” *Research on Chemical Intermediates*, vol. 33, no. 3–5, pp. 351–358, Mar. 2007, doi: 10.1163/156856707779238676.

[51] L. Derikvand and N. Tahmasebi, “Synthesis and photocatalytic performance of Bi2WO6/BiOX (X=Cl, Br, I) composites for RhB degradation under visible light,” *Korean J Chem Eng*, vol. 38, no. 1, pp. 163–169, 2021, doi: 10.1007/s11814-020-0687-y.

[52] M. F. Hanafi and N. Sapawe, “Effect of pH on the photocatalytic degradation of remazol brilliant blue dye using zirconia catalyst,” *Mater Today Proc*, vol. 31, pp. 260–262, 2020, doi: 10.1016/j.matpr.2020.05.746.

[53] Y. Guo, C. Zhou, L. Fang, Z. Liu, W. Li, and M. Yang, “Effect of pH on the Catalytic Degradation of Rhodamine B by Synthesized CDs/g-C$_3$N$_4$/Cu$_x$O Composites,” *ACS Omega*, vol. 6, no. 12, pp. 8119–8130, Mar. 2021, doi: 10.1021/acsomega.0c05915.

[54] Y.-W. Chen and Y.-H. Hsu, “Effects of Reaction Temperature on the Photocatalytic Activity of TiO2 with Pd and Cu Cocatalysts,” *Catalysts*, vol. 11, no. 8, p. 966, Aug. 2021, doi: 10.3390/catal11080966.

[55] N. A. M. Barakat, M. A. Kanjwal, I. S. Chronakis, and H. Y. Kim, “Influence of temperature on the photodegradation process using Ag-doped TiO2 nanostructures: Negative impact with the nanofibers,” *J Mol Catal A Chem*, vol. 366, pp. 333–340, Jan. 2013, doi: 10.1016/j.molcata.2012.10.012.

[56] Y. Zheng, S. Wang, M. Shu, Y. Wang, and D. Cao, “Effective BiOCl Electrons Collector for Enhancing Photocarrier Separation of Bi2WO6/BiOCl Composite,” *Chemistry an international journal*, vol. 4, no. 3, pp. 765–775, 2022, doi: 10.3390/chemistry4030054.

[57] A. M. Ganose, M. Cuff, K. T. Butler, A. Walsh, and D. O. Scanlon, “Interplay of Orbital and Relativistic Effects in Bismuth Oxyhalides: BiOF, BiOCl, BiOBr, and BiOI,” *Chemistry of Materials*, vol. 28, no. 7, pp. 1980–1984, Apr. 2016, doi: 10.1021/acs.chemmater.6b00349.

[58] Z. Liang, C. Zhou, J. Yang, Q. Mo, Y. Zhang, and Y. Tang, “Visible light responsive Bi2WO6/BiOCl heterojunction with enhanced photocatalytic activity for degradation of tetracycline and rohdamine B,” *Inorg Chem Commun*, vol. 93, pp. 136–139, 2018, doi: 10.1016/j.inoche.2018.05.022.

[59] M. Xu *et al.*, “Efficient degradation of pollutants by Bi2WO6/BiOCl heterojunction activated peroxymonosulfate: Performance and mechanism,” *J Environ Chem Eng*, vol. 12, no. 2, p. 112156, Apr. 2024, doi: 10.1016/j.jece.2024.112156.

[60] J. Wang *et al.*, “Constructing of ultrathin Bi2WO6/BiOCl nanosheets with oxygen vacancies for photocatalytic oxidation of cyclohexane with air in solvent-free,” *Appl Surf Sci*, vol. 584, p. 152606, May 2022, doi: 10.1016/j.apsusc.2022.152606.

[61] M. Guo *et al.*, “Bi2WO6–BiOCl heterostructure with enhanced photocatalytic activity for efficient degradation of oxytetracycline,” *Sci Rep*, vol. 10, no. 1, p. 18401, Oct. 2020, doi: 10.1038/s41598-020-75003-x.

[62] W. Yang, B. Ma, W. Wang, Y. Wen, D. Zeng, and B. Shan, “Enhanced photosensitized activity of a BiOCl–Bi2WO6 heterojunction by effective interfacial charge transfer,” *Physical Chemistry Chemical Physics*, vol. 15, no. 44, p. 19387, 2013, doi: 10.1039/c3cp53628a.

[63] Z. K. Cui, J. Q. Zhou, D. W. Zeng, J. L. Zhang, W. J. Fa, and Z. Zheng, “From BiOCl to Bi_2WO_6 in Bi–W–Cl–O solvothermal system: phase-morphology evolution and photocatalytic performance,” *Materials Technology*, vol. 30, no. 1, pp. 23–27, Jan. 2015, doi: 10.1179/1753555714Y.0000000196.

[64] N. A. Dhas, A. Ekhtiarzadeh, and K. S. Suslick, “Sonochemical Preparation of Supported Hydrodesulfurization Catalysts,” *J Am Chem Soc*, vol. 123, no. 34, pp. 8310–8316, Aug. 2001, doi: 10.1021/ja010516y.

[65] S. Zhu, C. Yang, F. Li, T. Li, M. Zhang, and W. Cao, “Improved photocatalytic Bi2WO6/BiOCl heterojunctions: One-step synthesis via an ionic-liquid assisted ultrasonic method and first-principles calculations,” *Molecular Catalysis*, vol. 435, pp. 33–48, Jul. 2017, doi: 10.1016/j.mcat.2017.03.016.

[66] J. Chen *et al.*, “Preparation of BiOCl/Bi2WO6 Photocatalyst for Efficient Fixation on Cotton Fabric: Applications in UV Shielding and Self-Cleaning Performances,” *Materials*, vol. 14, no. 22, p. 7002, Nov. 2021, doi: 10.3390/ma14227002.

[67] Z. Liang, C. Zhou, J. Yang, Q. Mo, Y. Zhang, and Y. Tang, “Visible light responsive Bi 2 WO 6 /BiOCl heterojunction with enhanced photocatalytic activity for degradation of tetracycline and rohdamine B,” *Inorg Chem Commun*, vol. 93, pp. 136–139, Jul. 2018, doi: 10.1016/j.inoche.2018.05.022.

[68] Y. Zhang, Y. Ma, L. Wang, Q. Sun, F. Zhang, and J. Shi, “Facile one-step hydrothermal synthesis of noble-metal-free hetero-structural ternary composites and their application in photocatalytic water purification,” *RSC Adv*, vol. 7, no. 80, pp. 50701–50712, 2017, doi: 10.1039/C7RA10732C.

[69] J. Nie, J. Schneider, F. Sieland, L. Zhou, S. Xia, and D. W. Bahnemann, “New insights into the surface plasmon resonance (SPR) driven photocatalytic H_2 production of Au–TiO_2,” *RSC Adv*, vol. 8, no. 46, pp. 25881–25887, 2018, doi: 10.1039/C8RA05450A.

[70] W. Hou and S. B. Cronin, “A Review of Surface Plasmon Resonance-Enhanced Photocatalysis,” *Adv Funct Mater*, vol. 23, no. 13, pp. 1612–1619, Apr. 2013, doi: 10.1002/adfm.201202148.

[71] M. Lemos de Souza, D. Pereira dos Santos, and P. Corio, “Localized surface plasmon resonance enhanced photocatalysis: an experimental and theoretical mechanistic investigation,” *RSC Adv*, vol. 8, no. 50, pp. 28753–28762, 2018, doi: 10.1039/C8RA03919D.

[72] Z. Chen, Y. Lu, Q. Zhang, D. Zhang, S. Li, and Q. Liu, “Electrochemistry Coupling Localized Surface Plasmon Resonance for Biochemical Detection,” 2022, pp. 15–35. doi: 10.1007/978-1-0716-1803-5_2.

[73] W. M. Haynes, D. R. Lide, and T. J. Bruno, Eds., *CRC Handbook of Chemistry and Physics*. CRC Press, 2016. doi: 10.1201/9781315380476.

[74] S. Das, R. Devireddy, and M. R. Gartia, “Surface Plasmon Resonance (SPR) Sensor for Cancer Biomarker Detection,” *Biosensors (Basel)*, vol. 13, no. 3, p. 396, Mar. 2023, doi: 10.3390/bios13030396.

[75] Y. Jiao, A. Hellman, Y. Fang, S. Gao, and M. Käll, “Schottky barrier formation and band bending revealed by first- principles calculations,” *Sci Rep*, vol. 5, no. 1, p. 11374, Jun. 2015, doi: 10.1038/srep11374.

[76] C. Buzea and I. Pacheco, “Gold and silver nanoparticles: Properties and toxicity,” in *Gold and Silver Nanoparticles*, Elsevier, 2023, pp. 59–82. doi: 10.1016/B978-0-323-99454-5.00007-X.

[77] K. Kim, J. Oh, T. W. Kim, J. H. Park, J. W. Han, and Y.-W. Suh, “Different catalytic behaviors of Pd and Pt metals in decalin dehydrogenation to naphthalene,” *Catal Sci Technol*, vol. 7, no. 17, pp. 3728–3735, 2017, doi: 10.1039/C7CY00569E.

[78] Z. Li and X. Meng, “Recent development on palladium enhanced photocatalytic activity: A review,” *J Alloys Compd*, vol. 830, p. 154669, Jul. 2020, doi: 10.1016/j.jallcom.2020.154669.

[79] H. Wang, B. Shi, Y. Liu, J. Guo, N. Chang, and X. Zhao, “Construction of Ag/Bi2WO6/BiOCl with enhanced photocatalytic performance for efficient degradation of organic pollutant,” *Inorg Chem Commun*, vol. 153, p. 110816, Jul. 2023, doi: 10.1016/j.inoche.2023.110816.

[80] X. Meng, Z. Li, and Z. Zhang, “Highly efficient degradation of phenol over a Pd-BiOBr Mott–Schottky plasmonic photocatalyst,” *Mater Res Bull*, vol. 99, pp. 471–478, Mar. 2018, doi: 10.1016/j.materresbull.2017.11.045.

[81] J. Yang *et al.*, “A compact Z-scheme heterojunction of BiOCl/Bi2WO6 for efficiently photocatalytic degradation of gaseous toluene,” *J Colloid Interface Sci*, vol. 631, pp. 44–54, Feb. 2023, doi: 10.1016/j.jcis.2022.11.023.

[82] M. Guo *et al.*, “Bi2WO6–BiOCl heterostructure with enhanced photocatalytic activity for efficient degradation of oxytetracycline,” *Sci Rep*, vol. 10, no. 1, p. 18401, Oct. 2020, doi: 10.1038/s41598-020-75003-x.

[83] B. Yao *et al.*, “Cost-effective Bi2WO6 for efficient degradation of rhodamine B and tetracycline,” *Journal of Materials Science: Materials in Electronics*, vol. 34, no. 4, p. 246, Feb. 2023, doi: 10.1007/s10854-022-09654-z.

[84] X. Meng, Z. Li, and Z. Zhang, “Pd-nanoparticle-decorated peanut-shaped BiVO4 with improved visible light-driven photocatalytic activity comparable to that of TiO2 under UV light,” *J Catal*, vol. 356, pp. 53–64, Dec. 2017, doi: 10.1016/j.jcat.2017.09.005.

[85] Z. Lu *et al.*, “Selective photodegradation of 2-mercaptobenzothiazole by a novel imprinted $CoFe_2O_4$/MWCNTs photocatalyst,” *RSC Adv*, vol. 5, no. 59, pp. 47820–47829, 2015, doi: 10.1039/C5RA08795C.

[86] Z. Wang and E. Hisahiro, “Recent trends in phenol synthesis by photocatalytic oxidation of benzene,” *Dalton Transactions*, vol. 52, no. 28, pp. 9525–9540, 2023, doi: 10.1039/D3DT01360J.

[87] A. A. Dubale *et al.*, “A highly stable metal–organic framework derived phosphorus doped carbon/Cu_2O structure for efficient photocatalytic phenol degradation and hydrogen production,” *J Mater Chem A Mater*, vol. 7, no. 11, pp. 6062–6079, 2019, doi: 10.1039/C8TA12544A.

[88] P. O. Oladoye, T. O. Ajiboye, E. O. Omotola, and O. J. Oyewola, “Methylene blue dye: Toxicity and potential elimination technology from wastewater,” *Results in Engineering*, vol. 16, p. 100678, Dec. 2022, doi: 10.1016/j.rineng.2022.100678.

[89] H. Jiang, Y. Li, X. Wang, and X. Hong, “Construction of a hydrangea-like Bi_2WO_6/BiOCl composite as a high-performance photocatalyst,” *New Journal of Chemistry*, vol. 46, no. 6, pp. 2627–2634, 2022, doi: 10.1039/D1NJ05409K.

[90] J. Chen *et al.*, “Preparation of BiOCl/Bi2WO6 Photocatalyst for Efficient Fixation on Cotton Fabric: Applications in UV Shielding and Self-Cleaning Performances,” *Materials*, vol. 14, no. 22, p. 7002, Nov. 2021, doi: 10.3390/ma14227002.

[91] A. A. Oyekanmi, A. Ahmad, K. Hossain, and M. Rafatullah, “Adsorption of Rhodamine B dye from aqueous solution onto acid treated banana peel: Response surface methodology, kinetics and isotherm studies,” *PLoS One*, vol. 14, no. 5, p. e0216878, May 2019, doi: 10.1371/journal.pone.0216878.

[92] S. Khanam and S. K. Rout, “Enhanced Photocatalytic Oxidation of RhB and MB Using Plasmonic Performance of Ag Deposited on Bi2WO6,” *Chemistry (Easton)*, vol. 4, no. 2, pp. 272–296, Apr. 2022, doi: 10.3390/chemistry4020022.

[93] M. Utami, S. Wang, F. I. Fajarwati, S. N. Salsabilla, T. A. Dewi, and M. Fitri, “Enhanced Photodegradation of Rhodamine B Using Visible-Light Sensitive N-TiO2/rGO

Composite," *Crystals (Basel)*, vol. 13, no. 4, p. 588, Mar. 2023, doi: 10.3390/cryst13040588.

[94] G. Li, "Electrospinning fabrication and photocatalytic activity of Bi2WO6 nanofibers," *Journal of Materials Science: Materials in Electronics*, vol. 28, no. 16, pp. 12320–12325, Aug. 2017, doi: 10.1007/s10854-017-7050-z.

[95] Y. Xu, Z. Shi, L. Zhang, E. M. B. Brown, and A. Wu, "Layered bismuth oxyhalide nanomaterials for highly efficient tumor photodynamic therapy," *Nanoscale*, vol. 8, no. 25, pp. 12715–12722, 2016, doi: 10.1039/C5NR04540A.

[96] Z. Xu, C. Zhang, Y. Zhang, Y. Gu, and Y. An, "BiOCl-based photocatalysts: Synthesis methods, structure, property, application, and perspective," *Inorg Chem Commun*, vol. 138, p. 109277, Apr. 2022, doi: 10.1016/J.INOCHE.2022.109277.

[97] G. Liu *et al.*, "BiOCl microspheres with controllable oxygen vacancies: Synthesis and their enhanced photocatalytic performance," *J Solid State Chem*, vol. 306, Feb. 2022, doi: 10.1016/J.JSSC.2021.122751.

[98] W. Yang, B. Ma, W. Wang, Y. Wen, D. Zeng, and B. Shan, "Enhanced photosensitized activity of a BiOCl–Bi2WO6 heterojunction by effective interfacial charge transfer," *Physical Chemistry Chemical Physics*, vol. 15, no. 44, p. 19387, 2013, doi: 10.1039/c3cp53628a.

[99] T. Hu, Y. Yang, K. Dai, J. Zhang, and C. Liang, "A novel Z-scheme Bi2MoO6/BiOBr photocatalyst for enhanced photocatalytic activity under visible light irradiation," *Appl Surf Sci*, vol. 456, pp. 473–481, Oct. 2018, doi: 10.1016/j.apsusc.2018.06.186.

[100] X. Qu *et al.*, "A novel ternary Bi4NbO8Cl/BiOCl/Nb2O5 architecture via in-situ solvothermal-induced electron-trap with enhanced photocatalytic activities," *Appl Surf Sci*, vol. 506, p. 144688, Mar. 2020, doi: 10.1016/j.apsusc.2019.144688.

[101] R. Jiang *et al.*, "Mineralization and toxicity reduction of the benzophenone-1 using 2D/2D Cu2WS4/BiOCl Z-scheme system: Simultaneously improved visible-light absorption and charge transfer efficiency," *Chemical Engineering Journal*, vol. 400, p. 125913, Nov. 2020, doi: 10.1016/j.cej.2020.125913.

[102] A. Phuruangrat *et al.*, "Synthesis of Ag/Bi2MoO6 Nanocomposites Using NaBH4 as Reducing Agent for Enhanced Visible-Light-Driven Photocatalysis of Rhodamine B," *J Inorg Organomet Polym Mater*, vol. 30, no. 2, pp. 322–329, Feb. 2020, doi: 10.1007/s10904-019-01190-4.

[103] C. Buttersack, "Modeling of type IV and V sigmoidal adsorption isotherms," *Physical Chemistry Chemical Physics*, vol. 21, no. 10, pp. 5614–5626, 2019, doi: 10.1039/C8CP07751G.

[104] M. N. Kajama, "Hydrogen permeation using nanostructured silica membranes," N. C. Nwogu and E. Gobina, Eds., May 2015, pp. 447–456. doi: 10.2495/SDP150381.

[105] X. Xiao *et al.*, “Degradation of rhodamine B in a novel bio-photoelectric reductive system composed of Shewanella oneidensis MR-1 and Ag3PO4,” *Environ Int*, vol. 126, pp. 560–567, May 2019, doi: 10.1016/j.envint.2019.03.010.

[106] M. Guo *et al.*, “Bi2WO6–BiOCl heterostructure with enhanced photocatalytic activity for efficient degradation of oxytetracycline,” *Sci Rep*, vol. 10, no. 1, p. 18401, Oct. 2020, doi: 10.1038/s41598-020-75003-x.

[107] W. M. Haynes, D. R. Lide, and T. J. Bruno, Eds., *CRC Handbook of Chemistry and Physics*, 95th ed. Boca Raton: CRC Press.

Chapter 5: Conclusions and Recommendations

5.1 Conclusions

In this study, Bi_2WO_6/BiOCl was optimized through the degradation of the industrial textile dye, Rhodamine B. The preparation of the composite was optimized by studying the effects of Bi_2WO_6:BiOCl ratio, treatment temperature, and treatment time. It was revealed that maximum RhB photodegradation is achieved with Bi_2WO_6/BiOCl made with a ratio of 1:0.3 for a period of 12 hours at 135°C. The improved degradation was attributed to a synergistic effect between Bi_2WO_6 and BiOCl that boosted visible light responsiveness and e^-/h^+ separation. Using XRD crystallography, it was revealed that the composite exhibited preferential growth along the (100) plane, which suggested the presence of internal electric fields to provide good charge carrier separation. This was underscored by SEM imaging, which showed the BiOCl plate extension along the surface of the Bi_2WO_6 microsphere, providing a good surface area for pollutant and light capture.

Using the optimized precursor, a novel Pd-Bi_2WO_6/BiOCl heterojunction catalyst was successfully fabricated using simple hydrothermal and photoreduction methods. By using XRD, XPS, and SEM analysis, it was observed that Pd deposition did not result in any significant change in the crystal lattice of Bi_2WO_6/BiOCl, allowing the main structure to retain its desirable properties. The photocatalytic activities of the samples were evaluated through the degradation of RhB under visible light. 0.5 wt% Pd-Bi_2WO_6/BiOCl showed the highest photodegradation rate, representing an improvement of 25.45% over the bare sample. It was inferred that the addition of palladium resulted in increased visible light absorption via the surface plasmon resonance effect. This was confirmed by UV-vis spectroscopy, which revealed that the sample had significantly broader spectral coverage in the range of 300 to 700 nm as compared to pure BiOCl, Bi_2WO_6, and

Bi_2WO_6/BiOCl. Additionally, by using the onset of the spectra, the band gaps of the samples were estimated. It was found that 0.5 wt% Pd-Bi_2WO_6/BiOCl had an E_g of 2.54 eV, making it applicable in the visible light range.

Using N_2 sorption isotherms, the surface area and pore volumes of the samples were calculated. It was revealed that Bi_2WO_6/BiOCl had a BET surface area of 56.37 m^2/g, which was considerably greater than that of pure Bi_2WO_6 and BiOCl. The Pd sample showed a similar value of 56.22 m^2/g, allowing it to exhibit similar adsorption characteristics as the bare sample. This was confirmed with RhB adsorption testing, which showed that both Bi_2WO_6/BiOCl and Pd-Bi_2WO_6/BiOCl had the most impressive adsorption profiles under pseudo-second-order modeling. The effects of certain operating parameters, including temperature, pH, catalyst dosage, and RhB concentration, were also investigated. The results also showed that the extent of photodegradation was consistent over the course of a four-stage recycle study, attesting to the stability of the catalyst.

Using a series of quenching experiments, a possible degradation mechanism was proposed. It was revealed that photoinduced h^+ and •OH were the main active species in the degradation of RhB. By calculating the valence and band positions, it was shown that Bi_2WO_6/BiOCl formed a type 1 heterojunction. The formation of the interface between the two parent semiconductors pushes both holes and electrons to move from the BiOCl to the Bi_2WO_6 structure. The addition of Pd creates a Schottky junction with the catalyst to form charge traps for electrons in the Bi_2WO_6 conduction band, allowing for increased visible light response. Furthermore, the holes on the Bi_2WO_6 VB can degrade RhB through direct oxidation or by reacting with OH molecules to form highly oxidative •OH radicals. The results of pH testing showed optimal activity at pH 6, suggesting that the direct oxidation mechanism is the more dominant mode of RhB degradation. Additionally, it was found that the decomposition of RhB proceeds via the N-de-ethylation route, which was revealed by a characteristic blue shift in the peak absorbance. Hence, the formation of the heterojunction coupled with the addition of palladium nanoparticles greatly enhanced the visible light degradation of the RhB molecules.

In conclusion, Bi_2WO_6/BiOCl samples hydrothermally prepared with a ratio of 1:0.3, a calcination temperature of 135°C, and a calcination time of 12 hours showcased enhanced photodegradation of RhB under visible light conditions. The addition of Pd to the surface of Bi_2WO_6/BiOCl resulted in a considerable increase in visible light activity and served as good evidence that plasmonic-enhanced heterojunction photocatalysts have great potential for the effective removal of organic pollutants in water.

5.2 Future Recommendations

Although all of the initial project objectives were achieved, there are many different avenues that could have also been studied but did not fit into the scope of this project. When reflecting on the work presented in this report, several ideas for future exploration come to mind. These aim to promote the application of photocatalytic systems and are listed as follows:

- This study focused on optimizing the conditions of the hydrothermal method to attain Bi_2WO_6/BiOCl composites. It should be noted that the ratio, temperature, and time were all tailored towards maximizing RhB degradation. However, to provide a more complete assay of this catalyst, other pollutants should also be considered. For instance, the conditions that provided optimal RhB decontamination may not be the same for other pollutants like methylene blue or phenol. Therefore, future work could focus on documenting the optimization conditions for other common organic pollutants. This would give a more complete understanding of Bi_2WO_6/BiOCl-driven water decontamination.

- In addition to the discussion on hydrothermal synthesis, other fabrication routes should also be considered. The hydrothermal route was selected for this study as it is the most popular choice in the literature, and as such, there is more data available to compare the results. However, other methods, including solvothermal and ionothermal, should also be explored to give a better comparison of the methods. These methods may lead to different morphologies for Bi_2WO_6 and BiOCl, thereby effecting the adsorption and photocatalytic kinetics. Hence, it is important to gain an understanding of these routes to truly discover which method is most appropriate for a given system.
- To simulate visible light radiation, a USHIO tungsten halide lamp was used in conjunction with a cutoff lens to filter out UV rays. To gain more insight into the visible light responsiveness of the samples, photocatalytic reactions should be performed under the sun or in a solar simulation setting. This would provide a more comprehensive analysis of the kinetics of visible-light photocatalysis.
- To date, limited work has been reported on the integration of Bi_2WO_6/BiOCl catalysts in solar cells or photocatalytic generators. Thus, an analysis of the use of this catalyst in a photoreactor could open different avenues for larger-scale applications. This could be realized by coating the catalyst onto small glass beads to create a lab-scale photoreactor for potential scale-up. Similar work has been done in this area with other plasmonic bismuth catalysts, which have shown promising results in decontaminating pollutants and bacteria.
- Other noble metals should also be introduced to Bi_2WO_6/BiOCl to allow for a comparative analysis of which metal achieves optimal results. The selection of Pd was made based on the work function and stability of the nanoparticles; however, other dopants like Au, Pt, and Ru have also shown promising results for other bismuth-based catalysts. Thus, these

metals should also be deposited on bare Bi_2WO_6/BiOCl to study their impacts on visible light activity.

- In light of the recent pandemic and ensuing health crisis, photocatalytic systems have been designed for surface disinfection of bacteria and viruses. Traditionally, TiO_2 has been coated on high-contact surfaces like doorknobs and tables. However, a visible-light active catalyst like Pd-Bi_2WO_6/BiOCl could prove to be more potent as it can absorb a wide spectral range, curtailing the need for external lighting sources. Indeed, this would require optimizing the conditions for different target germs, but the excellent visible light activity makes it a promising area to consider. Therefore, a study should be undertaken to assess the potential of the catalyst for disinfecting bacterial and viral cells.

The implementation of some of the mentioned studies would enrich the understanding not only of Bi_2WO_6/BiOCl but also of photocatalysts in general. As this field is still mainly on a lab scale, further work is required to help realize the great promise of environmental photocatalytic systems in the near future.

Appendix A: Reaction Kinetic Model

The photodegradation occurring in the system is considered to be a heterogenous catalytic reaction. As a result, the kinetics of the reaction can be calculated using the Langmuir-Hinshelwood (LH) model, shown in the equation below

$$r = -\frac{dc}{dt} = \frac{k_r K c}{1+Kc} \tag{1}$$

Where, c is the concentration of the substrate at a given time (t), k_r is the actual rate constant and K is the adsorption equilibrium constant.

In most cases the initial concentration of the organic pollutant being degraded is on the scale of mg/L (ppm), as such the Kc term is deemed negligible such that pseudo-first order kinetics are applied, and the reduced model follows

$$\ln\left(\frac{c_0}{c}\right) = k_{app} t \tag{2}$$

Where, c_0 and c are defined as the initial substrate concentration and substrate concentration at a given time, respectively.

The equation above was used the model the kinetics of photocatalytic degradation for this study. All the degradation rates reported in the thesis were calculate using the plots of the pseudo-first order model. From Equation 2, $\ln\left(\frac{c_0}{c}\right)$ can be plotted as a function time (t). The slope of the resulting plot is the apparent degradation rate constant (k_{app}). The following figure shows the rate constant equations plotted for Bi_2WO_6/BiOCl samples with varying amount of palladium.

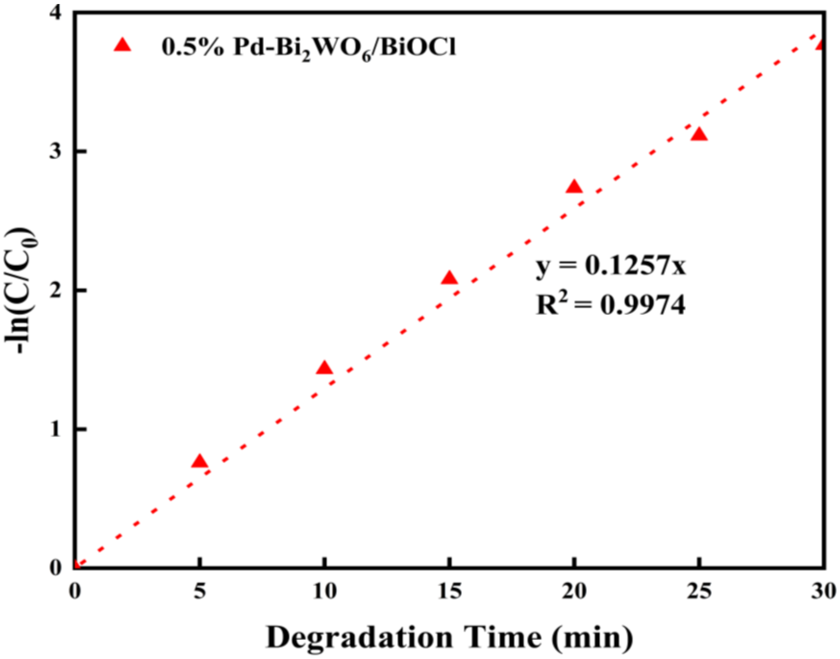

Figure A1: Pseudo-first order model for Pd-Bi$_2$WO$_6$/BiOCl samples.

Appendix B: Calculation of Band Gap

The band gap is an important optical property of a photocatalyst. To ascertain the band gap, diffuse reflectance data was collected for powder catalyst samples to give absorption plots shown below.

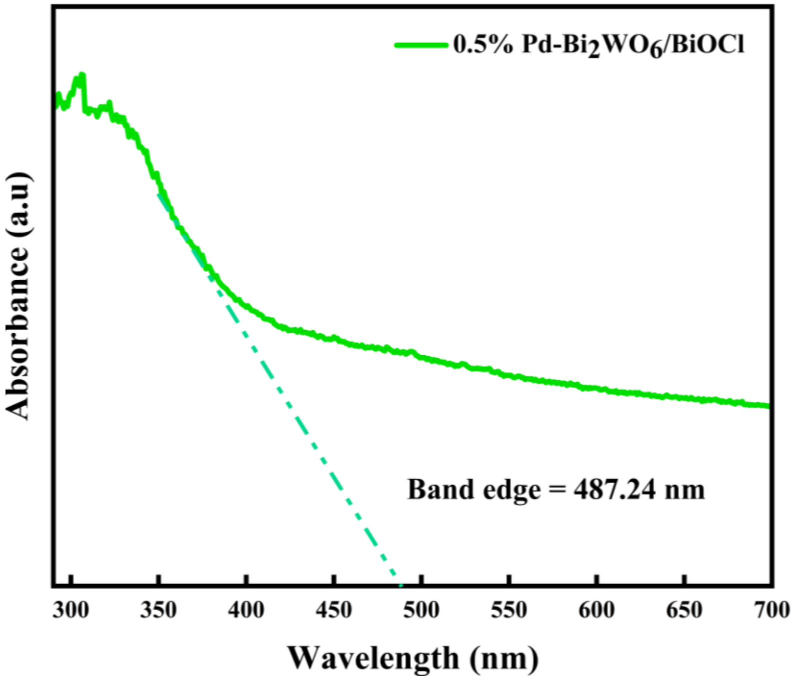

Figure B1: UV-vis absorption spectra for 0.5 wt% Pd-Bi_2WO_6/BiOCl.

This plot above shows the absorption spectra for 0.5% Pd-Bi_2WO_6/BiOCl in the range of 300 to 700 nm. As indicated with the dashed line, the absorption band edge (λ) was estimated to be 487.24 nm. Using the Planck equations, the band gap can be calculated as:

$$E_g(eV) = \frac{1240}{\lambda_{absorbance\text{-}edge}} \tag{1}$$

$$E_g(eV) = \frac{1240}{487.24} \tag{2}$$

$$\mathbf{E_g(eV) = 2.54} \tag{3}$$

Appendix C: Calculation of Band Positions

The valence and conduction band positions for Bi_2WO_6/BiOCl in Section 4.4.8 were estimated using the Mulliken electronegativity equations described in Section 2.3:

$$E_{CB} = \chi_p - E^e - 0.5E_g \qquad (1)$$

$$E_{VB} = E_{CB} + E_g \qquad (2)$$

Where, E_{CB}, E_{VB}, and E_g represent the position of the conduction band edge, valence band edge and the band gap. χ_p represents the semiconductor electronegativity and E^e represents the free electron energy using the hydrogen scale (~4.5 vs. NHE).

The following sample calculation was performed for the band positions of BiOCl where similar procedures were implemented for other samples as well:

1. The ionization energies and electron affinities for the constituent elements (Bi, O, and Cl) were gathered from the CRC handbook

Table C1: Ionization energy and electron affinity for constituent elements of BiOCl.

Atoms	Number of Atoms	Ionization Energy (eV)	Electron Affinity (eV)
Bi	1	7.29	0.942
O	1	16.62	1.461
Cl	1	12.97	3.613

2. Using the values from the table, the electronegativity values (χ) for the constituent elements were calculated as follows:

$$\chi_{Bi} = \frac{\text{Ionization energy + Ionization energy}}{2} = \frac{7.29 + 0.942}{2} = 4.11 \text{ eV}$$

$$\chi_{O} = \frac{\text{Ionization energy + Ionization energy}}{2} = \frac{16.62 + 1.461}{2} = 7.54 \text{ eV}$$

$$\chi_{Cl} = \frac{\text{Ionization energy} + \text{Ionization energy}}{2} = \frac{12.97 + 3.613}{2} = 12.97 \text{ eV}$$

3. From the electronegativity of the elements, a geometric mean was taken to give the overall electronegativity of BiOCl (χ_{BiOCl}) as 6.36 eV.
4. Using the Equation 1, the conduction band position was calculated as:

$$E_{CB} = 6.36 \text{ eV} - 4.5 \text{ eV} - 0.5(3.35 \text{ eV})$$

$$\mathbf{E_{CB} = 0.184 \text{ eV}}$$

5. From Equation 2, the valence band position was calculated as:

$$E_{VB} = 0.184 \text{ eV} + 3.35 \text{ eV}$$

$$\mathbf{E_{VB} = 3.53 \text{ eV}}$$

Figure C1: Estimated band positions for Bi_2WO_6 and BiOCl photocatalysts.

Photocatalyst	**χ_p (eV)**	**E^e (eV)**	**E_g (eV)**	**E_{CB} (eV)**	**E_{VB} (eV)**
Bi_2WO_6	6.21	4.50	2.89	0.26	3.15
BiOCl	6.36	4.50	3.35	0.18	3.53

Appendix D: RhB Standard and Calibration Curves

The standard absorbance and calibration curves for Rhodamine (RhB) are shown as follows.

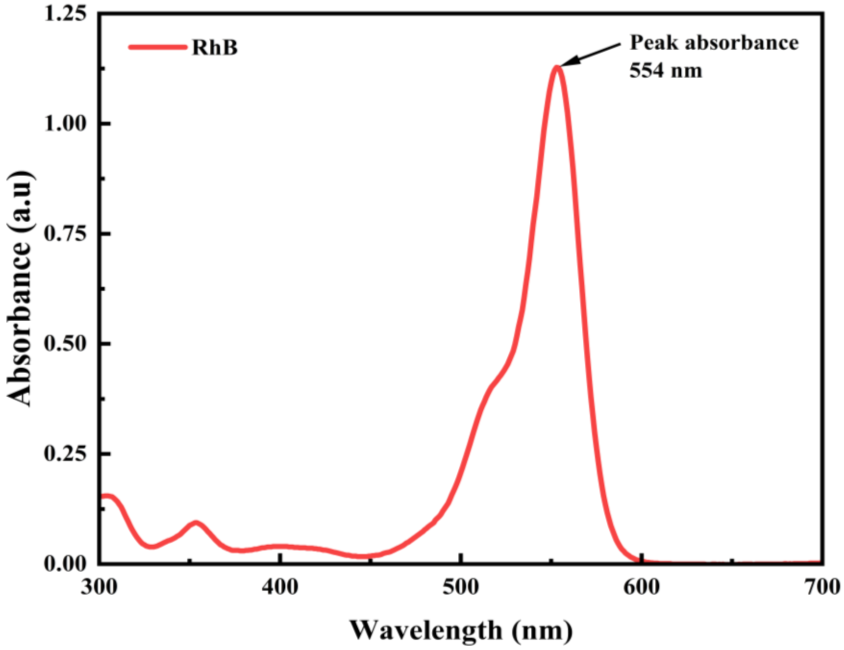

Figure D1: Peak Absorbance for RhB.

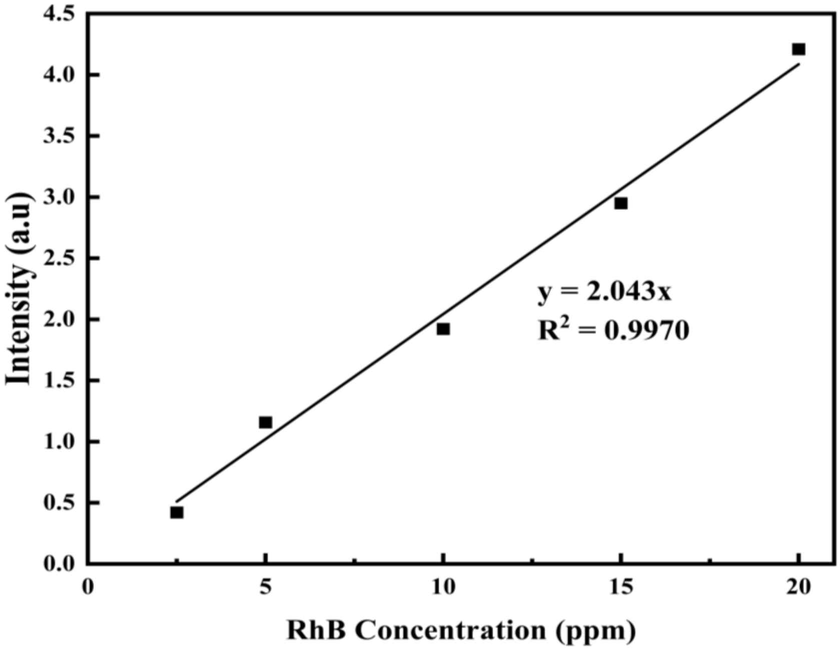

Figure D2: Calibration curve between RhB concentration and light intensity at 554 nm.

Appendix E: Photodegradation Repeatability Study

To assess the accuracy and repeatability of results, samples were synthesized three times under the same conditions and subsequently tested. The results for 0.5 wt% Pd-Bi_2WO_6/BiOCl are shown below:

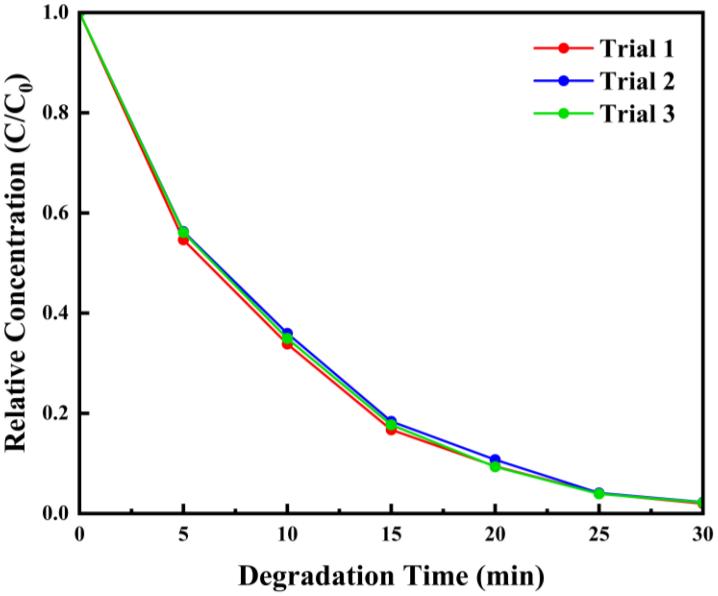

Figure E1: Repeatability test for 0.5% Pd-Bi_2WO_6/BiOCl catalyst (dosage: 0.5 g/L, temperature: 20 °C, pH: 4.8, RhB concentration of 10 ppm).

Figure E1 shows that all three trails display near-identical degradation profiles. This confirms that the optimized hydrothermal synthesis described in the procedure is repeatable and reliable. The pseudo-first order degradation rates are provided in the table below:

Table E1: Pseudo-first order rate constant (k_{app}) and R^2 for Pd-Bi_2WO_6/BiOCl samples in repeatability test.

Trial	k_{app} (min^{-1})	R^2
1	0.1257	0.9974
2	0.1215	0.9959
3	0.1242	0.9972

Appendix F: Experimental Setup

All the photocatalytic testing was conducted using a modified photoreactor system depicted in the figure below. The slurry batch reactor consisted of a 500 mL beaker fitted with a thermostatic cooling bath. Illumination was achieved using a 300 W tungsten halogen lamp (Ushio, USA) with a wavelength range of 310 to 800 nm to mimic solar radiation. The lamp was modified using a Kenko-Zeta filter (transmittance > 90%) to block irradiation with a wavelength below 410 nm, ensuring photocatalysis would take place strictly under visible light. Each run consisted of a select concentration of 200-mL of RhB solution as the catalytic substrate. The system was contained in a reflective house to ensure that the only source of radiation was the lamp.

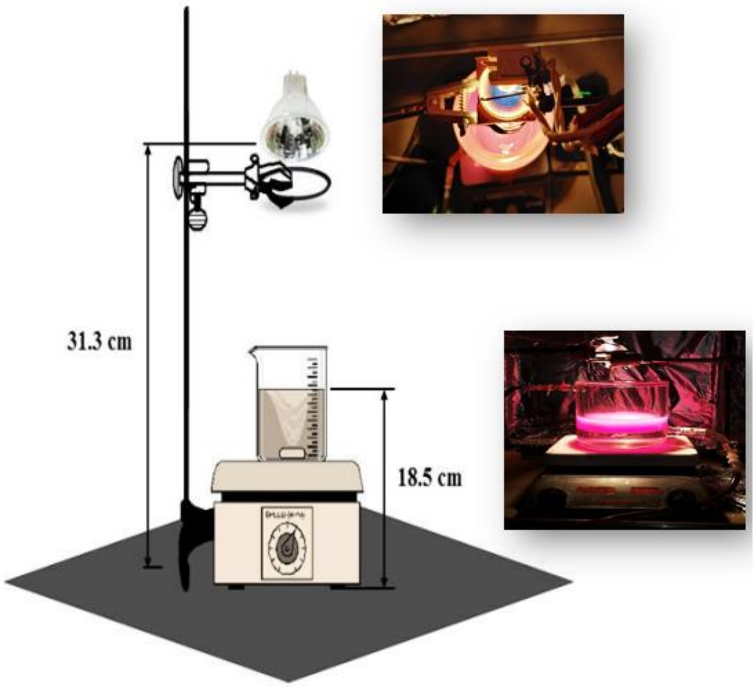

Figure F1: Schematic diagram of photoreactor setup used for degradation testing.